Measured and Modelled Turbulence Effects on Wind Turbine Wakes With Particular Focus on the Modelling of Vertical Momentum Influx Into Wind Farm Wakes

DISSERTATION

der Mathematisch-Naturwissenschaftlichen Fakultät
der Eberhard Karls Universität Tübingen
zur Erlangung des Grades eines
Doktors der Naturwissenschaften
(Dr. rer. nat.)

vorgelegt von
MORITZ MAUZ
aus Esslingen am Neckar

Tübingen
2023

Gedruckt mit Genehmigung der Mathematisch-Naturwissenschaftlichen Fakultät der Eberhard Karls Universität Tübingen.

Tag der mündlichen Qualifikation:	08.05.2024
Dekan:	Prof. Dr. Thilo Stehle
1. Berichterstatter:	Prof. Dr. Jens Bange
2. Berichterstatter:	Prof. Dr.-Ing. Hermann Knaus

Contents

Symbols

α	angle of attack
α	wind deficit decay rate
β	sideslip
C_T	thrust coefficient
C_T^*	cumulative thrust coefficient of a wind park
C_q^2	structure parameter for the specific humidity
δ_{ij}	Kronecker delta
d	WT turbulence layer thickness
D	rotor diameter
D	duration
D_ϕ	structure function of variable ϕ
ε_{ijk}	Levi-Civita symbol
f	frequency
f	geometric factor, ratio
f_c	Coriolis parameter
f_s	sampling frequency
ϕ_m	stability correction function
Γ	circulation or vortex strength
h	hub height
κ	von Kármán constant
K_m	momentum transfer coefficient
Λ	normalised wind deficit decay rate
L	characteristic length, half of peak-to-peak distance in the vortex evaluation
L	Obukhov length
N	number of measurements
Π	dimensionless constant
q	specific humidity

r	radius
r	spatial shift/lag
r_c	core radius
R	rotor radius
σ^2	variance
t	time
τ	time increment
u_0	free stream velocity in front of a wind turbine or wind farm
u_f	free stream velocity
u_r	residual wind speed
u_{r0}	initial (minimum) residual wind speed
u	wind component pointing positive east
v	wind component pointing positive north
v_g	ground speed
v_h	horizontal wind speed
V_t	tangential velocity
w	wind component pointing positive upwards
x	x-coordinate
y	y-coordinate
z	z-coordinate
Ω	angular velocity

Abbreviations

ABL	atmospheric bounday layer
AW	Amrumbank West (wind park)
a.g.l.	above ground level
BH	Burnham-Hallock (vortex model)
BMWi	Bundesministerium für Wirtschaft und Energie (Federal Ministry of Economic Affairs and Energy)
CBL	convective boundary layer
CFD	computational fluid dynamics
CMH	chilled-mirror hygrometer
DWD	Deutscher Wetterdienst (German Weather Service)
EFFWAKE	efficiency and wake (model)
FESSTVaL	Field Experiment on Submesoscale Spatio-Temporal Variability in Lindenberg
FWPRT	fine-wire platinum resistance thermometer
GPS	global positioning system
HeliOW	helicopter operations in off-shore wind parks (Helikoptereinsätze in Offshore Windparks)
IMU	inertial measurement unit
IR	infrared
LED	light emitting diode
LES	large-eddy simulation
lidar	light detecting and ranging
LI-COR	light, gas, and radiation sensors (manufacturer)
MASC	multi-purpose airborne sensor carrier
MOST	Monin Obukhov similarity theory
MSO	Meerwind Süd-Ost (wind park)
NREL	National Renewable Energy Laboratory (of US Department of Energy)
NO	Nordsee Ost (wind park)

NS	Navier-Stokes (equations)
met-tower	meteorological tower
PID	proportional-integral-derivative (controller)
PIV	particle image velocimetry
RMSD	root-mean-square deviation
SCADA	supervisory control and data acquisition
SHT31	Sensirion hygrometer and thermometer variant 31
SL	surface layer
SWIFFR	simple wind farm far-field recovery (model)
TDL	tunable diode laser
TEC	thermoelectric cooler
TC	thermocouple
UAS	uncrewed aircraft system
WEA	Windenergieranlage (wind energy converter)
WEC	wind energy converter
WFP	wind farm parametrisation
WIPAFF	wind park far field (project)
WRF	weather research and forecasting (model)
WT	wind turbine, synonymous to WEC

Acknowledgements

A lot of people have contributed in manifold ways to the work that eventually lead to this thesis. In particular I would like to acknowledge:

- My supervisor Prof. Dr. Jens Bange, for making this work possible, providing the necessary infrastructure, advise in multiple ways and giving room for development and my own ideas.
- Prof. Dr. Jens Bange and Prof. Dr.-Ing. Hermann Knaus for reviewing this thesis and participating in the doctoral graduation procedure.
- Dr. Wolfgang Junkermann for sharing his views and developments on chilled-mirror hygrometers.
- All my colleagues in the Umphy-team that shared their knowledge over the years with me: Bram van Kesteren, Andreas Platis, Kjell zum Berge, Martin Schön, Hasan Mashni, Uwe Putze, Ines Weber, Yann Büchau, Vasileios Savvakis, Matteo Bramati, Mosaab Sajidi, Gabriela Miranda, Alexander Rautenberg and Yongtan Wang.
- All the students that maintained software code, hardware and the MASC UAS: Lukas, Saskia and Frederick.
- Henrik and Lukas for piloting our MASC UAS skilfully on countless occasions.
- Frank Beyrich and the DWD for support and allowing us to take measurements at the Richard-Aßmann-Observatory in Lindenberg.
- My parents for their support in various ways. Especially to my father, who always knew that good things take time.
- While they are no 'people', but characters nevertheless, I thank Leela, Luna, Murmel and Ramses for sweetening-up my daily life with their affection, kindness and lovely dorkyness.
- I thank Sarina, for encouraging perfectionism at times when I was settling on mediocrity, giving comfort and warmth when my thesis stripped me of both.

The Project HeliOW (project number: 0324121B) and WIPAFF (project number: 0325783) are funded by the German Federal Ministry for Economic Affairs and Energy (BMWi) on the basis of a resolution of the German Bundestag.

Abstract

The presented work is based on experimental measurements behind wind (energy) turbines (WT). The wake behind a wind turbine and the inflow at different distances are measured. The data are the basis for a process chain in the HeliOW project, in which the wake of a $4.5\ \mathrm{MW}$ offshore wind turbine is modelled and validated with the UAS data. The focus is on investigating the influence of turbulence behind wind turbines and how it behaves in the wake. The unique measurements represent detached blade tip vortices (BSW), which are used as a reference in CFD (computational fluid dynamic) calculations. UAS measurements in the wake between 0.5 and 5 times the rotor diameter D show the behaviour of the wind deficit in the near and middle wake range. Based on these measurements, an analytical model of the wake of wind turbines was created. This model, called SWIFFR (simple wind farm far field recovery), is based on the Reynolds-averaged Navier-Stokes equations and uses the atmospheric turbulent momentum flux as a driving force that reduces the wind deficit and introduces kinetic energy into the atmospheric layer previously disturbed by the WT. The model was subsequently also applied to wake data from wind farms. Here a comparison was made with the EFFWAKE (efficiency and wake) model, which assumes an exponential course of the wind deficit. It can be shown that the SWIFFR model represents the wind speeds in the wake of wind farms more accurately. The EFFWAKE model is considered a representative of the top-down models, in which the analytical solution is derived from the equations describing the atmosphere. The SWIFFR model is also compared with the established Frandsen model (bottom-up). Here, the kinetic energy loss of the atmosphere in the wake is calculated purely from the perspective of turbine mechanics. The SWIFFR model offers the possibility to combine both approaches.

In the field of measurement sensors, breakthroughs were achieved in the area of turbulent air humidity measurement. A dew point mirror was designed and developed for use on airborne measurement platforms. There are no commercial solutions for such applications, as they are usually too heavy and too large. The new sensor development will be compared against commercial high-precision humidity sensors mounted on meteorological measurement towers. Likewise, the dew point measurement is compared with a LI-COR LI-7500RS, which also allows the comparison of measured turbulent variables. The newly developed dew point sensor allows measurements of the turbulent dew point up to $10\ \mathrm{Hz}$. Such a sensor opens up new possibilities for investigating phenomena in the lower atmosphere in which the turbulent moisture fluxes or density fluctuations of the air play a central role. Thus, for the first time, lift-dependent flows, e.g. in the wake of wind farms, can be studied in detail in the future.

Zusammenfassung

Die vorliegende Arbeit fußt auf experimentellen Messungen hinter Windenergieanlagen (WEA). Es werden der Nachlauf hinter einer WEA und die Zuströmung in verschiedenen Abständen vermessen. Diese Daten sind die Grundlage für eine Prozesskette im Projekt HeliOW (Helikoptereinsätze in Offshore Windparks), in welchem u.a. der Nachlauf einer $4,5\ \mathrm{MW}$ Offshore-WEA modelliert und mit den UAS Daten validiert wird. Dabei liegt der Fokus auf der Untersuchung des Einflusses der Turbulenz hinter WEA und wie diese sich im Nachlauf verhält. Die einzigartigen Messungen bilden abgelöste Blattspitzenwirbel (BSW) ab, welche als Referenz in CFD-Rechnungen (computational fluid dynamic, dt. rechnergestützte Strömungsdynamik) eingehen. UAS Messungen im Nachlauf zwischen $0,5$ und fünffachem Rotordurchmesser D zeigen das Verhalten des Winddefizits im nahen und mittleren Nachlaufbereich auf. Basierend auf diesen Messungen wurde ein analytisches Modell des Nachlaufs von WEA erstellt. Dieses Modell names SWIFFR (simple wind farm far field recovery) basiert auf den Reynolds-gemittelten Navier-Stokes Gleichungen und nutzt den atmosphärischen turbulenten Impulsfluss als treibende Kraft, welche das Winddefizit abbaut und kinetische Energie in die vormals durch die WEA gestörte Atmosphärenschicht einträgt. Das Modell wurde im weiteren Verlauf auch auf Nachlaufdaten von Windparks angewandt. Hier wurde ein Vergleich zum EFFWAKE Modell durchgeführt, welches einen exponentiellen Verlauf des Winddefizits annimmt. Es kann gezeigt werden, dass das SWIFFR Modell die Windgeschwindigkeiten im Nachlauf von Windparks genauer abbildet. Das EFFWAKE Modell gilt als Vertreter der top-down Modelle, in welchen die analytische Lösung aus den die Atmospähre beschreibenden Gleichungen hergeleitet wird. Das SWIFFR Modell wird ebenso mit dem etablierten Frandsen Modell (bottom-up) verglichen. Hierbei wird der kinetische Energieverlust der Atmosphäre im Nachlauf rein aus der Perspektive der Turbinenmechanik errechnet. Das SWIFFR Modell bietet die Möglichkeit beide Ansätze zu verbinden.

Im Bereich der Messsensorik wurden Durchbrüche auf dem Gebiet der turbulenten Luftfeuchtemessung erlangt. Es wurde ein Taupunktspiegel entworfen und entwickelt, welcher auf luftgestützten Messplattformen zum Einsatz kommt. Für solche Einsatzzwecke gibt es keine kommerziellen Lösungen, da diese in der Regel zu schwer und zu groß sind. Die Neuentwicklung des Sensors wird gegen kommerzielle hochgenaue Luftfeuchtesensoren, montiert auf meteorologische Messtürmen, verglichen. Ebenso wird die Taupunktmessung mit einem LI-COR LI-7500RS verglichen, welches auch den Vergleich turbulenter Messgrößen erlaubt. Der neu entwickelte Taupunktspiegelsensor ermöglicht Messungen des turbulenten Taupunkts bis zu $10\ \mathrm{Hz}$. Mit einem solchen Sensor eröffnen sich neue Möglichkeiten, Phänomene in der unteren Atmosphäre zu untersuchen, bei welchen die turbulenten Feuchteflüsse oder Dichteschwankungen der Luft eine zentrale Rolle spielen. Somit lassen sich erstmals auch auftriebsabhängige Strömungen, z.B. im Nachlauf von Windparks in Zukunft detailiert untersuchen.

List of peer-reviewed first author publications

Mauz, M., Rautenberg, A., Platis, A., Cormier, M., and Bange, J. First identification and quantification of detached-tip vortices behind a wind energy converter using fixed-wing unmanned aircraft system. *Wind Energy Science*, 4(3):451–463, 2019. doi: 10.5194/wes-4-451-2019. URL `https://www.wind-energ-sci.net/4/451/2019/`.

Mauz, M., van Kesteren, B., Junkermann, W., zum Berge, K., Schön, M., Platis, A., and Bange, J. Miniature high-frequency chilled-mirror hygrometer for atmospheric measurements aboard fixed wing UAS. *Meteorologische Zeitschrift*, 29:439–449, 07 2020. doi: 10.1127/metz/2020/1026. URL `http://dx.doi.org/10.1127/metz/2020/1026`.

Mauz, Moritz, Emeis, S., Hoeckh, F., van Kesteren, B., Platis, A., and Bange, J. Towards higher accuracy in wind farm deficit decay modelling - a comparison. *Meteorologische Zeitschrift*, 09 2023. doi: 10.1127/metz/2023/1183. URL `http://dx.doi.org/10.1127/metz/2023/1183`.

List of peer-reviewed co-author publications

Cormier, M., Bühler, M., **Mauz, M.**, Lutz, T., Bange, J., and Krämer, E. Cfd prediction of tip vortex aging in the wake of a multi-mw wind turbine. *Journal of Physics: Conference Series*, 1618, 2020. URL https://iopscience.iop.org/article/10.1088/1742-6596/1618/6/062029/pdf.

Platis, A., Hundhausen, M., **Mauz, M.**, Siedersleben, S., Lampert, A., Bärfuss, K., Djath, B., Schulz-Stellenfleth, J., Canadillas, B., Neumann, T., Emeis, S., and Bange, J. Evaluation of a simple analytical model for offshore wind farm wake recovery by in situ data and weather research and forecasting simulations. *Wind Energy*. doi: 10.1002/we.2568. URL https://onlinelibrary.wiley.com/doi/abs/10.1002/we.2568.

Rautenberg, A., Schön, M., zum Berge, K., **Mauz, M.**, Manz, P., Platis, A., van Kesteren, B., Suomi, I., Kral, S. T., and Bange, J. The multi-purpose airborne sensor carrier masc-3 for wind and turbulence measurements in the atmospheric boundary layer. *Sensors*, 19(10), 2019. ISSN 1424-8220. doi: 10.3390/s19102292. URL http://www.mdpi.com/1424-8220/19/10/2292.

Wildmann, N., **Mauz, M.**, and Bange, J. Two fast temperature sensors for probing of the atmospheric boundary layer using small remotely piloted aircraft (rpa). *Atmospheric Measurement Techniques*, 6(8):2101–2113, 2013. doi: 10.5194/amt-6-2101-2013. URL https://www.atmos-meas-tech.net/6/2101/2013/.

zum Berge, K., Schoen, M., **Mauz, M.**, Platis, A., van Kesteren, B., Leukauf, D., El Bahlouli, A., Letzgus, P., Knaus, H., and Bange, J. A two-day case study: Comparison of turbulence data from an unmanned aircraft system with a model chain for complex terrain. *Boundary-Layer Meteorology*, 180:53–78, 2021. ISSN 0306-2619. doi: 10.1007/s10546-021-00608-2.

Conference contributions

Mauz, M. A high-frequency chilled-mirror hygrometer for turbulent stationary and airborne dew-point measurements. In *EMS Annual Meeting - online, Hannover*, 2021. `https://meetingorganizer.copernicus.org/EMS2021/EMS2021-508.html`.

Mauz, M. and Bange, J. Current uav-assisted wind energy-research projects at the university of tuebingen with the in-house built masc aircraft. In *ISARRA, Oban*, 2017. `http://www.isarra.org/wp-content/uploads/2017/05/ProgrammeFullAbstractsISARRA2017_20170516.pdf`.

Mauz, M., Rautenberg, A., Platis, A., Cormier, M., and Bange, J. First identification and quantification of detached-tip vortices behind a wind energy converter using fixed-wing unmanned aircraft system. In *EGU General Assembly, Vienna*, 2018. `https://meetingorganizer.copernicus.org/EGU2019/EGU2019-14117.pdf`.

Mauz, M., Junkermann, W., Platis, A., and Bange, J. High frequency chilled mirror hygrometer for atmospheric measurementswith fixed wing UAS. In *EMS Annual Meeting, Kopenhagen*, 2019a. `https://meetingorganizer.copernicus.org/EMS2019/EMS2019-899.pdf`.

Mauz, M., Rautenberg, A., Platis, A., Cormier, M., and Bange, J. Erste Identifizierung und Quantifizierung von abgelösten Blattspitzenwirbeln hinter einer WEA mit einem Starrflügler UAS. In *Meteorologentagung DACH2019-43, Garmisch-Partenkirchen*, 2019b. `https://www.dach2019.de/DACH2019-abstracts.pdf`.

Mauz, M., Rautenberg, A., Platis, A., Cormier, M., and Bange, J. First identification and quantification of detached-tip vortices behind a wind energy converter using fixed-wing unmanned aircraft system. In *EMS Annual Meeting, Kopenhagen*, 2019c. `https://meetingorganizer.copernicus.org/EMS2019/EMS2019-898.pdf`.

Mauz, M., Rautenberg, A., Platis, A., Cormier, M., and Bange, J. First identification and quantification of detached-tip vortices behind a wind energy converter using fixed-wing unmanned aircraft system. In *ISARRA, Lugo*, 2019d. `http://www.isarra.org/?page_id=625`.

Mauz, M., Rautenberg, A., Platis, A., Cormier, M., and Bange, J. First identification and quantification of detached-tip vortices behind a wind energy converter using fixed-wing unmanned aircraft system. In *Wind Energy Science Conference, Cork*. European Academy of Wind Energy, 2019e.

Mauz, M., Rautenberg, A., Platis, A., Cormier, M., and Bange, J. First identification and quantification of detached-tip vortices behind a wind energy converter using fixed-wing unmanned aircraft system. In *WindForS Science Meeting, Garmisch-Partenkirchen*, 2019f. `https://www.windfors.de/wp-content/uploads/2019/02/WindForS-2019-GPK-Meeting-2019-02-21.pdf`.

Mauz, M., Emeis, S., Höckh, Platis, A., and Bange, J. An analytical solution for wind deficit decay behind a single wind turbine / wind farms using momentum conservation validated by airborne data. In *WESC - wind energy science conference - online, Hannover*, 2021.

1 Introduction

In natural science, measurements can either be proof for a theory or be the foundation, and necessary spark for new principles or simple ideas that are derived from them. Either way, measurements did take a fundamental role in understanding natures laws – and they still do. One might think that in the 21st century all scientific frontiers have been conquered, but mankind and its ever evolving technology simply pushes the frontier farther by answering one question that arises a new one. Some people find this frightening, yet for others it is beautiful. This work is mainly aimed to the latter part of society that might find joy and use from some answers that are provided in this thesis. May they be able to solve the questions that arise in the wake of it.

The measurements and the work presented in this thesis aim to help to better understand the behaviour of the atmosphere, which is directly influenced by wind turbines (WTs). Thus, this thesis may contribute to wind energy research in general and to boundary-layer meteorology.

Nowadays, it is impossible to imagine a modern energy supply without renewable energies. Wind power accounts for a large share of this, and there is no end in sight to the expansion of (offshore) wind energy in Germany and the world. In addition, wind turbines are constantly growing in size and output. Therefore, their impact onto the environment, e.g. the surrounding atmospheric flow and the wind turbine wakes, is increasing, which raises new issues. Some of which will be addressed in this thesis based on atmospheric airborne measurements and analytical modelling.

The task of a WT is simple: Converting momentum taken from the mean wind to electrical energy. A state-of-the-art WT can reach up to $260\ \mathrm{m}$ into the atmosphere. In offshore wind farms, these altitudes are the typical inversion base heights in the marine boundary layer (Zhong et al., 2017). Thus, rotor diameters of $220\ \mathrm{m}$ (Haliade-X 12 MW) and a hub height of $150\ \mathrm{m}$ of the WT take up almost one third of the atmospheric boundary layer (ABL) that stretches up to around $1\ \mathrm{km}$ (Stull, 2000). Modern WTs need to deal with different effects than their smaller predecessors, that mainly operated in the surface layer (SL), the lowest part of the ABL. While WTs still operate the same way, turbulence created below an inversion height interacts differently than turbulence introduced above an inversion height, due to different thermal stabilities in these regions.

Understanding turbulence created by a WT is the key to understand the structures in the wake of a WT, and has always been of interest for scientists and engineers. Vermeer et al. (2003); Vermeer (1992) studied detached blade-tip vortices in the early days of wind energy harvesting, using smoke trail wind tunnel experiments. Those studies were an approach to understand the coherent helical turbulence structure that can be found behind every operating WT. Wind tunnel experiments gained a lot of popularity, since they provided a possibility to study WTs in a controlled environment at a reasonable cost and effort. Also the size of a single WT alone is often the limiting factor, preventing a study in a real-world scenario. With progress in technology, wind tunnel experiments were accompanied with high resolution PIV (particle image velocimetry) measurements that made it possible to resolve turbulence in the near wake of a model WT (Zhang et al., 2012). However, a common problem with wind tunnel measurements is that they tend to suffer from scaling problems when transferred to full size WTs (Wang et al., 1996, 2020). Also to set up and to maintain different thermal stratifications in wind tunnels is a difficult task.

Remote sensing techniques like lidars (light detecting and ranging) usually provide measurements with a spatial resolution in the range of $30\ \mathrm{m}$. This spatial resolution is not suitable to study small-scale turbulence, but lidar measurements are well suited for long term wake monitoring by detecting wake centres and their behaviour with changing wind direction (Bodini et al., 2017; Wildmann et al., 2018). Advances in filter functions for lidar data improved turbulence estimation. Though, it is possible to calculate dissipation rates in the lower atmosphere (Wildmann et al., 2020). Short range continuous wave lidars also provide higher spatial resolution at short focal lengths and have been used in WT wake measurements (Menke et al., 2018). Yet, these measurements still do not resolve and isolate single small-scale phenomena, e.g. blade-tip vortices which play a dominant role in the near wake of a WT, as will be explained later in this thesis.

In-situ atmospheric measurements can resolve small-scale turbulence, e.g. sonic anemometers mounted on a weather observation mast. A drawback of in-situ measurements that are fixed in one location, is the fact that turbulent structures usually have a short life span, and to fully understand turbulent phenomena, spatial information is needed. The helipod (pod of meteorological equipment dragged by a helicopter) campaign (Bange and Roth, 1999; Muschinski et al., 2001; Platis et al., 2017) was a successful approach to gather in-situ turbulence in-line data in the atmosphere over heterogeneous terrain. While these kinds of atmospheric measurements provide a certain amount of mobility, they also come with high costs and restrictions, e.g. minimum flight height or down-wash of the helicopter for follow-up measurements. Uncrewed aircraft systems (UAS) are in many respects the ideal measurement platform. They are guided by GPS (global positioning system) and fly autonomously to predefined waypoints (on a high resolution spatial grid), e.g. in a WT wake.

The research UAS of type MASC-3 (multi-purpose airborne sensor carrier), shown in Fig. 1.1, is a fixed-wing airborne measurement system designed and operated by the University of Tübingen (Wildmann et al., 2013, 2014a,b,c; Mauz et al., 2019; Rautenberg et al., 2019; Mauz et al., 2020; zum Berge et al., 2021) and is used to capture in-situ atmospheric data.

The MASC-3 system is equipped for high-frequency measurements with a sensor response time $< 0.05\ \mathrm{s}$, except for humidity. The atmospheric flow, meaning the 3-D wind vector, is measured by a five-hole pressure probe. The ambient air temperature is measured by a fine-wire platinum resistance thermometer (FWPRT). Thus, it is able to resolve pressure and temperature related turbulent structures at very small scale up to $20\ \mathrm{Hz}$ (Wildmann et al., 2013; Mauz et al., 2019). All recorded data are stored with a sampling frequency of $500\ \mathrm{Hz}$. Post-processing, the data are scaled, synchronized and available at $100\ \mathrm{Hz}$. In addition to the atmo-

wingspan	$4\ \mathrm{m}$
total weight	$\approx 7\ \mathrm{kg}$
sci. payload	$\approx 1\ \mathrm{kg}$
cruising speed	$18.5\ \mathrm{m\ s^{-1}}$
endurance	up to $2.5\ \mathrm{h}$
propulsion	electrical pusher engine
autopilot	Pixhawk 2.1 'Cube'
take-off	bungee/winch/catapult

Figure 1.1: *MASC-3 UAS (uncrewed aircraft system) shortly after lift-off, equipped with optional wing-pods for particle and electro-static measurements. Photographed by Bernd Lammel for the DWD (German Weather Service). The measurement instruments and probes are located at the very front. To the right, the main technical specifications are summarised.*

spheric parameters, the IMU (inertial measurement unit) records the necessary GPS position, orientation angles and angular accelerations. See Rautenberg et al. (2019) for a detailed description of the UAS and its instrumentation.

The data presented in this work are i.a. captured by a MASC-3 UAS operated behind a WT in the near wake, partially at a distance of 0.25 rotor diameter D. High resolution turbulence measurements can resolve blade-tip vortices in the near wake of a WT. A method to measure, to identify, and to quantify blade-tip vortices has been developed (Mauz et al., 2019). Measuring the dimensions of blade-tip vortices is of great importance to define grid sizes in large-eddy simulations (LES) (Kim et al., 2016). LES of blade-tip turbulence need a point of reference for the grid size which is proportional to the core radius r_c to resolve blade-tip vortices and converge correctly (Cormier et al., 2020). A method to identify blade-tip vortices is helpful to define the near wake region of a WT wake. The near wake region of the wake is not defined by a fixed distance, it can range from about $0.5 - 3.0\ \mathrm{D}$ and is characterised by the presence of a continuous helical vortex hose. This coherent helical structure acts like a shield to the developing initial wind deficit behind the nacelle, against the surrounding turbulent momentum influx by the atmosphere (Lignarolo et al., 2014). Once the momentum and energy of the vortex hose structure is depleted, those vortex hoses collapse. From thereon leewards, the vanished 'shield' enables momentum transfer from the undisturbed atmosphere. The wind deficit that peaks at around $0.5 - 1.0\ \mathrm{D}$ (nacelle effects), is now exposed. This behaviour of the near wake turbulence and wind deficit was shown by wind tunnel measurements by Medici and Alfredsson (2006). The key to understand the collapse of the vortex structure behind the nacelle is vortex ageing. Vortices experience viscous shear effects that drain the rotational energy and lead to a widening of the vortex hose core radius. These viscous effects, together with shear forces, eventually weaken and decelerate the vortex helix to the point where the vortex hoses get unstable and disintegrate.

Frandsen (2007) gives a general description of the wind deficit and turbulence development in a WT wake. He distinguishes between artificial turbulence that is created by the WT and natural turbulence, e.g. entraining vertically and laterally from the surrounding free stream. To understand turbulence behaviour in a wake, it is important to understand that the entraining turbulence from the free flow is coupled to the wind deficit decay. The turbulent influx is the reason the wind speed will regain energy, until the level of the free-stream velocity is reached again (Emeis, 2010). The whole process of restoring the initial wind speed in a wake starts by the 'natural' atmospheric turbulence mixing with the artificial turbulence, added by the WT. Frandsen (2007) divides the radial symmetric wake of a WT in turbulence that 'knows its origin' (artificial turbulence) in the core of the wake, and turbulence situated in the outer regions that has mixed with atmospheric turbulence. With increasing distance from the nacelle, the fraction of turbulence 'knowing its origin' decreases until it is undistinguishable from the free flow turbulence. While atmospheric turbulence is measurable, it is very difficult to distinguish artificial turbulence by the WT from the free flow turbulence in an in-situ measurement. Since the entraining turbulence can be linked to the decay of the wind deficit, the mean horizontal wind velocity in the wake can be used as an easy to measure parameter instead.

Aside from the engineering aspect of wind turbines, the spacing between individual converters within a wind farm has become a significant factor in wind energy research and wind farm design. Extensive efforts have been made to determine a realistic cost ratio and to establish minimum distances between wind turbines (Meyers and Meneveau, 2012; Yang et al., 2012). Although the individual wake of a wind turbine in an offshore wind farm has been specifically researched (Fuertes et al., 2018; Sedaghatizadeh et al., 2018), studies investigating the wake of the entire offshore wind farm have only been carried out recently. The WIPAFF (wind park far field) project (Emeis et al., 2016; Platis et al., 2020a,b) provides a unique data set of in-situ wind farm wake measurements. The data were captured at different thermal atmospheric conditions. Wake lengths of up to $60\ \mathrm{km}$ were observed in stable atmospheric conditions. Wind farms and their wake effects are part of weather research and forecasting (WRF) models (Siedersleben et al., 2018). These model simulations are computational intensive. The WT wakes can be described and calculated individually (bottom-up approach) forming a collective wind farm wake or the wind farm wake can be described (top-down), e.g. analytically. Usually, provided the wind farm is large enough, leeward of a wind farm, only one giant wake in the rotor plane is identifiable. Thus, there is a benefit in saving computational power and in computing a single wind farm wake. The benefit of utilising a top-down analytical model for a wind farm is that it can offer solutions for various thermal stratifications while treating the farm as a 'black box'. This eliminates the need for computing the wake for every single turbine, as required by the bottom-up approach demonstrated in, e.g. Niayifar and Porté-Agel (2016). Simple top-down analytical solutions are also useful for meso-scale WRF simulations or quick wake length assessments. Emeis (2010) presented a straightforward analytical model called EFFWAKE (efficiency and wake) to depict the flow field behind an offshore wind farm. The model postulates that the wind deficit decays exponentially with a constant rate (α). EFFWAKE's strongest points are its versatility and simplicity. However, the model's wake recovery lacks precision and neglects the wind farm's geometry (Platis et al., 2018). An outstanding problem with the EFFWAKE model is determining a critical parameter: the separation height Δz, which divides the wind farm wake from the geostrophic flow that lies above it (Platis et al., 2020b). Additionally, the decay of the wind farm wake necessitates consideration of wind farm design (WT spacing and density) and lateral momentum (in)flux across the wake (Platis et al., 2018). As a result, uncertainties persist regarding the pace at which wind deficit reduces. Therefore, a wind farm wake analytical model capable of estimating wake with only a few parameters would assist in accurately quantifying wind farm wakes while requiring minimal computational resources.

In an effort to improve quick wind farm wake assessment, a model derived from the Reynolds-averaged momentum conservation equation of the free flow has been introduced and compared to the existing EFFWAKE and Frandsen model. This new simple wind farm far-field recovery analytical wake model (SWIFFR) is simple to use, and predicts wind farm wakes using a minimal amount of input parameters. The model approach also differs from known semi-empirical bottom-up models, e.g. the Jensen (1983), Frandsen et al. (2006) or Katić et al. (1987) model, which are usually benchmarked using CFD calculations (Kaldellis et al., 2021).

The dimensions of single WTs and the mixing of air they cause, especially in wind parks, suggest that buoyancy may become a mechanism in a wake that needs to be investigated more thoroughly. Buoyancy-driven flows occur with variation of density. For example a stable marine boundary layer can be massively disturbed by a wind park. Denser air near the sea surface is artificially moved to higher, warmer altitudes, and warmer, more humid air is forced downwards.

Buoyancy is also important when studying the convective boundary layer (CBL). Muppa et al. (2016) studied turbulent humidity fluctuations in the CBL using lidar (light detection and ranging) measurements. Their lidar measurements capture a daily cycle of humidity in a column directly above the lidar instrument. UAS measurements would provide a spatial mapping of turbulent humidity flux, e.g. in a CBL. FESSTVaL (Field Experiment on Submesoscale Spatio-Temporal Variability in Lindenberg) was a measurement campaign (2019–2021) from several universities and the German Weather Service (DWD) that aims to validate lidar measurements, to improve existing weather forecast models and investigates cold pool events in a CBL as well as the formation of thunder cells in a CBL, e.g. on a hot and humid summer day. The (turbulent) humidity transport inside the CBL is also an important factor for the formation of cloud layers (Moeng and Arakawa, 2012). A light-weight, high-frequency sensor that can be equipped on an airborne platform could add a lot of valuable data and input to current research topics in boundary-layer meteorology.

Hajra (2014) reviewed recent studies on buoyancy-driven flows and concludes that analytical and empirical relations based on laboratory measurements have not been successfully applied for geophysical scales, and, hence, a proper understanding of the physical processes associated with buoyancy-driven flows in nature is necessary. Thus, there is a high demand for field studies dealing with that phenomenon.

A key parameter to investigate buoyancy is the air density that is dependent of temperature and its moisture content. While high-frequency thermometers exist for UAS platforms (Wildmann et al., 2013), there are no light-weight, high-frequency options for humidity sensors available. This circumstance led to the in-house development of a humidity sensor on the basis of the chilled-mirror principle.

Commercially available humidity sensors that can accurately measure turbulent moisture fluctuations often have significant drawbacks that make their use on a UAS platform impractical. However, fast-response humidity sensors that use optical absorption techniques, including Lyman-alpha, TDL (tunable diode laser), or IR (infrared) absorption, have the ability to determine the variance, as well as other relevant turbulent humidity parameters, with greater accuracy (De Bruin et al., 1993). However, all these listed sensors are not suited to be mounted on small UAS, since they are too heavy and too big. Lyman-alpha and IR high-frequency humidity sensors have been installed in research aircraft (Platis et al., 2017; Lampert et al., 2018) or in a helipod probe (Bange and Roth, 1999; Muschinski et al., 2001) where they proofed their capability to operate on mobile platforms. For a UAS, the weight of a sensor is one of the key factors to consider. Available humidity sensors that are very light-weight (≈ 10 g) and cheap, are capacitive sensors. Those sensors measure the relative humidity in the air by measuring the capacitance of a capacitor. The underlying principle for these sensors is that water vapour diffuses into a dielectric porous material, and therefore changes the capacitance (the measurement signal) of the sensor. These sensor types have typically a temporal resolution smaller than 1 Hz. As a result, these sensors are not fast enough to detect turbulent moisture fluxes on board of an aircraft. In a first approach to make those sensors usable for UAS based measurements in the lower atmosphere, Wildmann et al. (2014b) applied an inverse model onto the measured humidity signal. This post-processing step increased the temporal resolution of a capacitive sensor up to 3 Hz. A main draw-back of this method is the artificial increase of the noise which in practice makes this method unsuitable for turbulent humidity measurements and evaluation. Also the inverse model uses a fixed diffusion coefficient which is temperature dependent. Therefore, in practice the model needs to be retuned for every measurement to the ambient temperature. So it seems that capacitive sensors are at their technical limit, since they are already very small, with a diameter of around 2 mm and a thickness of less than 1 mm the dielectric component can not be designed any smaller without sacrificing measurement accuracy. Therefore, to complete the MASC measurement platform with a humidity sensor that can measure turbulent humidity fluctuations, a sensor had to be developed, tailored to the boundary conditions specified by the MASC platform.

For the in-house design of a high-frequency humidity sensor, the chilled-mirror hygrometer (CMH) principle was chosen. These sensors measure the dew point temperature of the air directly, hence also the name dew point mirror. The dew point is the temperature, at which humidity condenses spontaneously, and the rate of condensation is equal to the rate of evaporation. The measurement principle of a CMH is simple. A metallic surface (usually a small gold mirror) is cooled down by a TEC (thermoelectric cooler), and when the dew point is reached, the temperature of the mirror is measured. The challenge in designing a CMH, is to always keep the same amount of condensate on the mirror. In the in-house built CMH this complex control loop is achieved by the implementation of a PID (proportional-integral-derivative) software controller. One of the most important advantages of a CMH sensor, in contrast to a capacitive sensor, is that the atmospheric parameter (dew point) is a very robust humidity measure and can be directly measured. Figure 1.2 shows a schematic of the sensor principle and the working prototype mounted on the MASC-3 UAS (Mauz et al., 2020). The measurement principle has been compared to capacitive sensors, with the result that CMH sensors, especially in radiosondes, do not suffer from a change of response time, in contrast to capacitive sensors, due to the temperature dependent diffusion of water vapour (Fujiwara et al., 2003). Commercially available CMH sensors unfortunately lack the temporal resolution that is required to measure turbulent humidity changes. The in-house CMH uses a PID software controller that regulates the sensor 50 times per second. The measurements are compared against average values using the meteorological tower (met-tower) data, and also

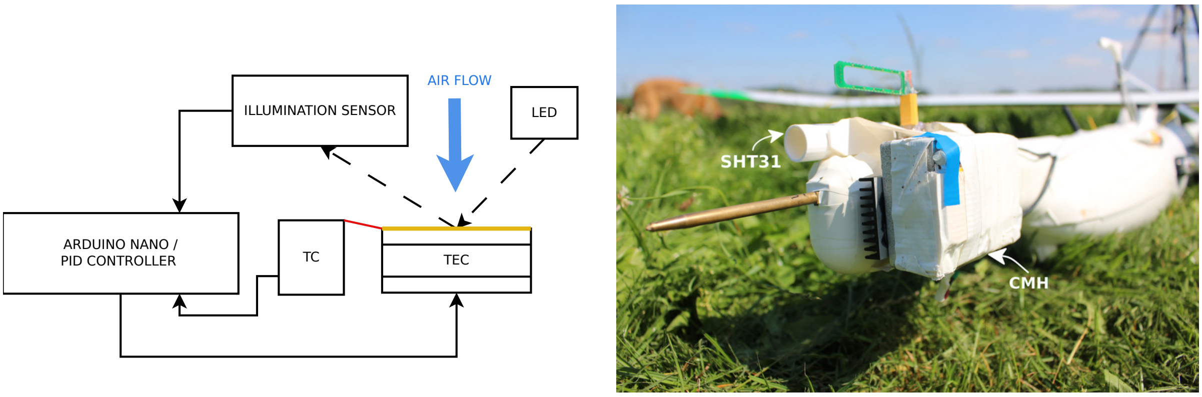

(a) **(b)**

Figure 1.2: ***(a)*** *Schematic of how the CMH works. The CMH is made up of off-the-shelf components, such as the microprocessor (Arduino Nano), which contains, among other routines, the PID controller that regulates the voltage output to the thermoelectric cooler (TEC). The gold layer on the TEC acts as a mirror in direct contact with the incoming air. The thermocouple (TC) thermometer measures the temperature of the mirror.*
(b) *Mounted CMH prototype (2019) onto the sensor dome of the MASC-3 UAS. The inlet is located under the blue tape. On the other side of the sensor dome, the SHT31 thermo-hygrometer is mounted inside a flow tube. Figures taken from Mauz et al. (2020).*

the high-frequency response of the CMH is evaluated using the same UAS data.

In an effort to make the CMH sensor smaller and an integral part of the UAS and its sensor system, the design has been further improved: The sensor has been integrated into the sensor dome with an air inlet reaching through the fuselage into the undisturbed flow (s.a. Fig. 1.3). The heat sink is cooled by the air flow around the UAS, providing reliable cooling power. By moving the sensor inside the sensor dome, the manoeuvrability of the UAS is no longer altered, in contrast to the first prototype mounting (s.a. Fig. 1.2b).

Research Questions

In the preceding introductory pages, various topics have been presented, but they are linked by a common theme: Turbulence. More precisely: Turbulence measurement with aircraft systems. Always with the aim of measuring/resolving, describing and, if necessary, modelling turbulent structures and phenomena behind wind turbines. From this, the following concrete research questions can be derived, which shaped the course of my doctorate:

1. How large are detached blade-tip vortices from wind turbines?
   And what is their influence on the wake?
2. How is the residual wind velocity recovering behind a WT in the wake?
   What is the role of atmospheric turbulence?
3. Is there an influence of turbulent moisture flux on density-driven flows behind WTs?
4. How to measure turbulent moisture flux with UAS?

The points mentioned above are partly interdependent. The following pages will address the research questions above.

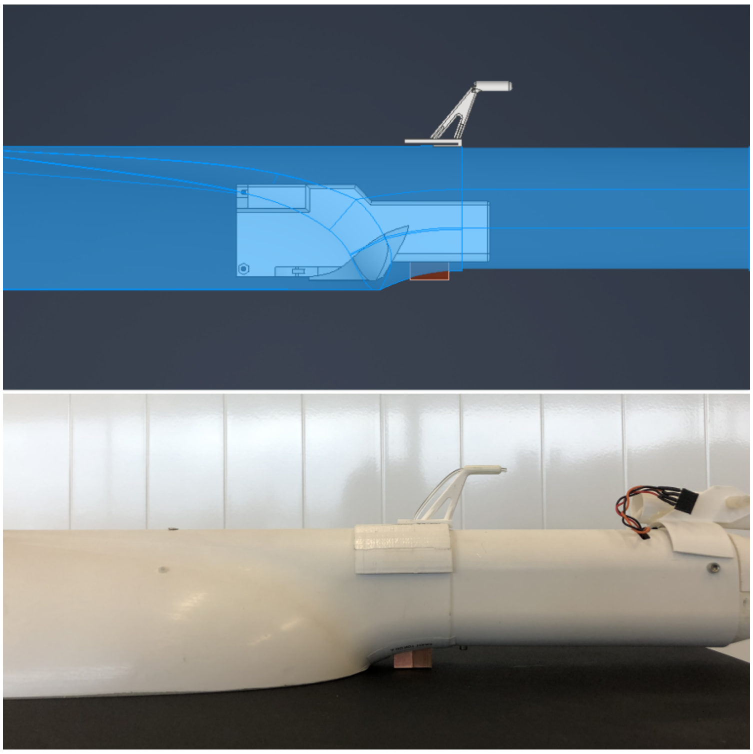

Figure 1.3: (Top) *Sketch of the latest iteration of the CMH (2021) located inside the sensor dome of the MASC-3 UAS. With courtesy of Matteo Bramati.* ***(Below)*** *Own photograph of the present sensor dome. By relocating the sensor inside of the UAS the flight properties of the UAS remain unaltered. The heat sink is still cooled by the boundary layer flow of the UAS.*

2 Results

This section will provide a summary of the most important results that are explained in detail in the articles attached to this thesis (Apps. A.1 to A.3).

2.1 Detached Blade-tip Vortices

Blade-tip vortices are one of the most prominent turbulent structures that are associated with WT turbulence. Usually, in form of helical vortex hoses that spiral around the wind deficit in the wake. In the following, a two-dimensional simplification, i.e. a cut through such a vortex hose at hub height, is considered. The vortex properties of such a vortex are measured and compared to LES results.

All WT wake related data were obtained in the framework of the BMWi (Bundesministerium für Wirtschaft und Energie, engl. Federal Ministry of Economic Affairs and Energy) funded project HeliOW (helicopter operations in off-shore wind farms), at the Jade Windpark north of Wilhemshaven in Germany. One of the main goals in the HeliOW project is to set up a model chain, including an LES wake model that is combined with a helicopter rotor dynamics simulation, whereas the LES wake model is validated by in-situ MASC-3 data. One of the key features to provide a realistic wake model is to compute the blade-tip vortices and its dynamics correctly (Kim et al., 2016). Thus, aside from inflow and wind deficit measurements the detection and evaluation of blade-tip vortices are of great importance to enable the development of an LES model of a wake that is as close as possible to the real-world counterpart. From an in-situ measurement point of view, the challenge is not only to measure the blade-tip vortex, but also to identify the wind measurement as a blade-tip vortex and to evaluate the measurement. Since there does not exist such a method to identify and evaluate a blade-tip vortex from a fly-by measurement behind a WT, a method suited to the UAS-based measurement procedure has been developed. The method will be briefly explained, followed by the results when applied to WT wake measurements.

The underlying vortex model for the applied method in Mauz et al. (2019) is the Burnham and Hallock (1982) model (BH). It has been also successfully applied to describe counter-rotating vortices studying detached aircraft wing vortices (Fischenberg, 2011). In wind energy science, this vortex model has previously been applied to wind tunnel smoke trail measurements by Vermeer (1992). Due to its simplicity, it has been chosen to be used for the MASC-3 evaluations. Analysis of the in-situ measurements and comparison with the BH model represent a new approach for the assessment of turbulence behind wind turbines. Equation 2.1 describes the tangential velocity $V_\mathrm{t}(r)$ of a vortex with circulation Γ and core radius r_c at distance r from the vortex centre in the BH model.

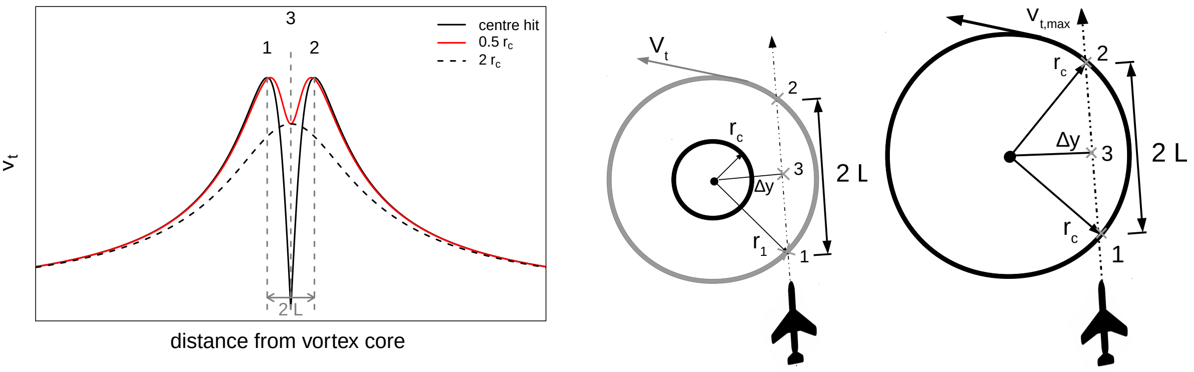

(a) **(b)** **(c)**

Figure 2.1: ***(a)*** *Analytical solution for the tangential velocity distribution V_t at different distances Δy from the vortex centre. The black solid line is the solution of Eq. 2.1 for r reaching from $-\infty$ to ∞ and $\Delta y = 0$, the black broken line corresponds to a solution for $\Delta y = 2r_\mathrm{c}$* ***(b)*** *and the red solid line is an exemplary solution for $\Delta y = 0.5r_\mathrm{c} < r_\mathrm{c}$* ***(c)****. Figures taken from Mauz et al. (2019).*

$$V_\mathrm{t}(r) = \frac{\Gamma}{2\pi} \cdot \frac{r}{r_\mathrm{c}^2 + r^2} \tag{2.1}$$

An analytical solution of Eq. 2.1 is shown in Fig. 2.1a (black solid line). This solution also corresponds to a UAS measurement for $\Delta y = 0$ which is a (rare but not impossible) boundary case for the UAS passing the vortex centre at $\Delta y < r_\mathrm{c}$ shown schematically in Fig. 2.1c. With Δy the lateral offset of the UAS relative to the vortex core. For a successful blade-tip vortex evaluation the UAS has to pass the vortex between the vortex centre and $\Delta y = r_\mathrm{c}$, otherwise a set of equations that leads to the calculation of r_c and Γ has indefinite amount of solutions. Once the UAS measures a blade-tip vortex under the necessary conditions, the measurement of the horizontal wind shows a double peak feature similar to the red line at position 1 and 2 in Fig. 2.1a.

At the time of the measurement campaign at the Jade wind park, no experience in measuring detached blade-tip vortex has been gained previously. Therefore, no guarantee to gain usable blade-tip vortex measurements could be given. However, to gather data the UAS passed the wake at $0.25\ \mathrm{D}$ and $0.5\ \mathrm{D}$ at hub height roughly 40 times. Distinguished blade-tip measurements were only available at the close vicinity to the nacelle where the measurement signals were more defined. From these measurements, only one fly-by could be used to determine all vortex parameters (s.a. Fig. 2.2a). The horizontal wind speed measurement along the flight path in Fig. 2.2a shows the undisturbed wind speed being $\approx 9\ \mathrm{m\ s^{-1}}$. Two clearly visible peaks mark the entering and exit of the wake. In-between the two peaks the average wind speed in the wake is reduced to approximately $5\ \mathrm{m\ s^{-1}}$. Illustration 2.2b shows the same measurement but split in all wind components. Here, it can be seen that the blade-tip vortex is mainly rotating in the horizontal plane, thus u and v bare the main rotational energy, as can be expected at hub height. For a more precise evaluation, the measurement has been rotated into the rotational plane of the vortex that slightly differs from the horizontal plane. Hence, after rotation the w component is almost completely eliminated. Now, the main rotational energy splits between the u and v component. Figure 2.2c and Fig. 2.2d show the blade-tip vortex measurements 1 and 2 in a more detailed resolution with the vortex centre as the centre of a radial symmetric coordinate system (cf. Fig. 2.1a). The positions 1,2 and 3 as shown in Fig. 2.1a,b mark the double peak, and define the beginning and the end of the secant with length $2L$ from which the vortex parameters r_c and Γ can be derived by means of a dimensionless relationship (Eq. 2.2) described in all detail in Mauz et al. (2019) or in App. A.1 of this thesis. Equation 2.2 describes the relation of the tangential velocities (left hand side) measured at point 3 (numerator) and point 1 or 2 (denominator) in Eq. 2.2, with the respective positions shown in Fig. 2.1.

$$\frac{V_{\mathrm{t},\Delta\mathrm{y}}}{V_{\mathrm{t,max}}} = \frac{r_\mathrm{c}\sqrt{r_\mathrm{c}^2 - L^2}}{r_\mathrm{c}^2 - \frac{L^2}{2}} \tag{2.2}$$

The above equation is applied to the measured data after the parameters like L and the tangential velocities are extracted.
With

$$V = \frac{V_{\mathrm{t},\Delta\mathrm{y}}}{V_{\mathrm{t,max}}} \tag{2.3}$$

and L the half of the peak-to-peak distance, the equation for the vortex core radius is:

$$r_\mathrm{c} = \frac{\sqrt{-L^2V^2 + L^2 + \sqrt{-L^4(V^2-1)}}}{\sqrt{-2V^2+2}}. \tag{2.4}$$

Equation 2.4 gives the vortex core radius with a known ratio of wind speeds V and peak-to-peak distance. The latter can be easily worked out from the UAS data if the speed over ground is accurate.

Furthermore, the broken purple line in Fig. 2.2c,d shows the norm of the wind vector and serves as a quality criterion for the coordinate rotation: in the vicinity of the vortex centre and core radius the now rotated horizontal wind must be identical with the norm of the wind vector, due to one of the wind components (here w) is approximately zero.

The resulting vortex parameters using the evaluation method and Eq. 2.2 described in Mauz et al. (2019) are shown in Tab. 2.1. Here, the blade-tip vortex measurements are compared against CFD calculations with and without a refined mesh grid around the blade, and in the near wake region up to $0.35\ \mathrm{D}$. The CFD calculations were made for comparable inflow conditions as they existed on the day of the UAS measurements (Cormier et al., 2020). Additionally, the circulation Γ is calculated from SCADA (supervisory control and data acquisition) data using Eq. 2.5 from literature, e.g. (Sørensen et al., 2014),

$$\Gamma = \frac{\pi v_\infty^2 C_\mathrm{T}}{\Omega N_b} \tag{2.5}$$

with N_b the number of blades of the WT, its rotational velocity Ω, the undisturbed wind velocity v_∞ and C_T the thrust coefficient of the WT. The CFD calculations with variable grid size show how important the in-situ measurements are to verify CFD results. Both CFD calculations result in a plausible vorticity. Only one of the CFD calculations, using a tip mesh, shows a realistic vortex radius of 0.6 m versus 2.06 m.

Table 2.1: *Vortex parameters derived from in-situ measurements, calculated from SCADA data of the WT and based on a CFD calculation by Cormier et al. (2020) using comparable inflow conditions as prevailed at the measurement site.*

	r_c [m]	Γ [m^2 s^{-1}]	Γ/Γ_{CFD} [−]
measured vortex 1	0.66	81.3	1.15
measured vortex 2	0.55	67.04	0.95
CFD - without tip mesh	2.06	74.5	1.05
CFD - with tip mesh	0.6	70.85	1.0
SCADA	-	66.2	0.93

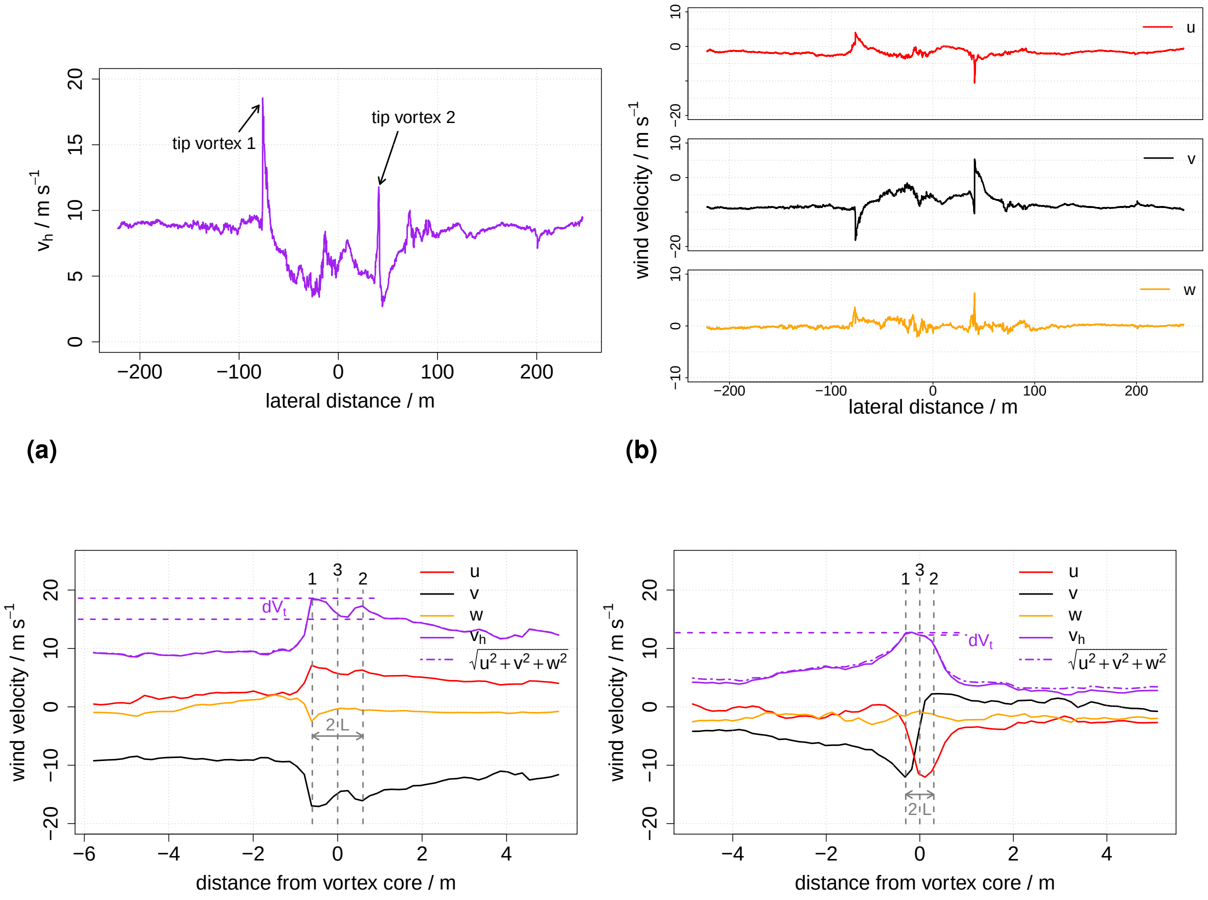

(a) **(b)** **(c)** **(d)**

Figure 2.2: *Set of a measurement of two blade-tip vortices at* 0.25 D *behind a WT (Mauz et al., 2019).* ***(a)*** *Measurement of the horizontal wind along the whole flight path.* ***(b)*** *The same measurement, but split into all three wind components.* ***(c)*** *Zoom into tip vortex 1 with a radial symmetric reference coordinate system at the vortex centre. Positions 1,2 and 3 are as in Fig. 2.1c. The broken purple line shows the norm of the wind vector and serves as a quality criterion for the coordinate rotation (here they almost superimpose). In the vicinity of the vortex centre and core radius the now rotated horizontal wind must be identical to the norm of the wind vector due to one of the wind components (here* w*) is approximately zero.* ***(d)*** *Same as (c) but for tip vortex 2.*

2.2 Wind Farm Wake Recovery – The SWIFFR Model Proposal

In order to extract value from measured data, they are usually cross-checked with existing data sets or compared with theoretical analytical or empirical models. In-situ wind farm wake data are a novelty and no other data are available, thus, the next step is to compare the data to any kind of model that would describe the data. Platis et al. (2018) took the first step by comparing in-situ wind farm wake data to the EFFWAKE model (Emeis, 2010) and have worked out the strengths and weaknesses of the model. The EFFWAKE model provides an exponential, time-dependent solution, describing the residual wind velocities in the wind farm wake (s.a. Sec. 2.2.1).

In the wake of the data processing and evaluation, it became apparent that a simple analytical model describing the wind farm wake deficit, preferably derived from flow-governing equations is not yet available. The wind deficit is the difference of the wind velocity in the wind turbine wake (or wind farm wake) and the wind velocity in the surrounding flow. Generally, atmospheric flow models can be classified in top-down and bottom-up approaches. The latter ones describe the flow from the obstacle that disturbs the flow, e.g. a wind turbine acting as a momentum sink. A popular example is the Frandsen (Frandsen et al., 2006) model. Top-down models describe a flow related phenomenon by the flow governing equations, e.g. the EFFWAKE model or the SWIFFR model proposed in this thesis.

The EFFWAKE model has been refined in the recent years Emeis (2017, 2022) and its analytical description is of great value in meteorology and wind farm management. In order to find a steady-state location-dependent pendent to the EFFWAKE model, the idea was born to develop a similar model starting from the Navier-Stokes (NS) flow governing equations. The resulting SWIFFR model will be compared against the EFFWAKE (Emeis, 2010) and Frandsen (Frandsen et al., 2006) model. All three models involved in the comparison are presented below.

2.2.1 The EFFWAKE Model

The EFFWAKE model is an analytical model that describes the residual wind speed recovery in the wake of a wind farm by an exponential function. Equation 2.6 describes the residual wind speed u_r in the wake of a wind farm following Emeis (2010, 2017).

$$\frac{u_r(t)}{u_0} = 1 + \left(\frac{u_{r0}}{u_0} - 1\right) \exp(-\alpha t) \tag{2.6}$$

With u_{r0} the initial wind deficit in the wake directly behind the wind park at $x = 0$ and u_0 the undisturbed wind speed at hub height in the inflow. The EFFWAKE model uses a bulk parametrisation to simplify the Reynolds shear stress, the driving force that degrades the wind deficit and reintroduces kinetic energy into the wake. This simplification results in a wake deficit decay rate $\alpha = K_\mathrm{m}/d^2$ that is assumed constant along the wake with momentum transfer from aloft the wake at distance d from height $z = h + d$. The atmospheric stability influences the momentum transfer coefficient K_m. Therefore, an additional stability correction function ϕ_m, applicable in the lower atmosphere, is implemented (Garratt, 1994).

$$K_{\mathrm{m}} = \frac{\kappa u_* z}{\phi_m(z/L)} \tag{2.7}$$

For a neutral stratification, $\phi_m(z/L) = 1/\gamma = 1$ can be applied, for unstable and stable stratifications different corrections must be made.

$$\phi_m\left(\frac{z}{L}\right) = \begin{cases} 1/\gamma & \text{for} \frac{z}{L} < 0 \\ 1 & \text{for } \frac{z}{L} = 0 \\ 1 + a\frac{z}{L} & \text{for } \frac{z}{L} > 0 \end{cases} \tag{2.8}$$

With $\gamma = (1 - b\ z/L)^{0.25}$ and L the Obukhov length, $a = 5$ and $b = 16$. Thermal stability related deviations of the model are evaluated by Canadillas et al. (2020). They calculate the initial wind velocity deficit u_{r0}/u_0, as a function of ambient turbulent intensity I_u, the collective farm thrust coefficient C_{T}^*, effective drag coefficient C_D and turbine spacing (WTs per certain distance) of different wind farms. Then, they use the EFFWAKE model to project the residual wind speeds in specific wind farm clusters and compare it to in-situ data and a commercially available software model. For more details on the implementation, the reader is referred to Appendix B in Canadillas et al. (2020).

Another study using the EFFWAKE model was done by Platis et al. (2018). They substituted the initial wind deficit behind the wind farm u_{r0}/u_0 with a measured value from the WIPAFF (wind park far field) campaign and compare the EFFWAKE model results to measured in-situ data. In the EFFWAKE model, the atmospheric stability is represented by u_* and a correction function ϕ_m. But as ϕ_m is determined as a constant, it merely acts as a weighting factor for the momentum transfer coefficient K_m (see Eq. 2.7). Both studies, with different approaches, show a certain level of flexibility of the EFFWAKE model. However, a tight fit to the data is mainly limited to the near wake or the far wake (Platis et al., 2018).

2.2.2 The Frandsen Model

The second model, the SWIFFR model is compared to, is the Frandsen et al. (2006) model, or also simply referred to as Frandsen model. This model is a popular representative of a bottom-up model, while the SWIFFR model uses a top-down approach. The square-root function of the SWIFFR model (Equation 2.11) exhibits similarities with the Frandsen model in terms of the suggested wake shape of the wind farm. The model addresses an orderly array layout consisting of straight rows of wind turbines, with each unit being equidistantly spaced within and between the rows (Frandsen et al., 2006). The Frandsen model calculates a wind farm wake length by using an effective wind farm thrust coefficient C_{T}^*, a wind turbine (array) related parameter that is linked to the momentum transfer from kinetic to electrical energy. Instead of the rotor diameter D, an effective wake expansion coefficient k is used.

The latter two can be written as a single parameter k^*:

$$\frac{u_r}{u_0} = \frac{1}{2}\left(1 + \sqrt{1 - \frac{2C_\mathrm{T}^*}{1 + 2k^*x}}\right) \tag{2.9}$$

The predicted residual wind speed in the wake is normalised by the free stream velocity in front of the wind farm u_0 at hub height. The parameter k^* is mainly reduced to a fitting parameter, that is affected by various variables additionally to the rotor diameter, like thermal stratification, shear stress and momentum transfer, e.g. over different terrain. Thus, it is almost impossible to define common wake widening factors (Andersen et al., 2014).

2.2.3 The SWIFFR Model

Inspired by the time-dependent EFFWAKE model, and in search of a steady-state location-dependent solution, the SWIFFR model was developed. Same as the EFFWAKE model, the SWIFFR model describes the residual wind speeds along the wake centre line behind a wind farm, but the model can also be applied to single wind turbine wakes. The formalism is derived from a simplification of the Navier-Stokes (NS) flow governing equation. Various terms can be disregarded in the Navier-Stokes equations when dealing with boundary-layer flows featuring very low friction (Prandtl, 1904). Therefore, the model uses two remaining terms; the advection of mean momentum and the Reynolds stress term. The full and detailed derivation is described in App. A.2. The Reynolds stress term is approximated via an empirical relation, assuming a first-order distribution of the vertical Reynolds shear stress. Thus, the Reynolds shear stress is represented using a momentum transfer coefficient K_m (refer to Eq. 2.7), and it is transformed into a finite difference format at the wake centreline at hub height h. The resulting non-linear, non-homogeneous differential equation is:

$$\frac{du_r^2}{dx} = \underbrace{\frac{CK_\mathrm{m}}{R^2}\left(\frac{1}{f}+1\right)}_{\alpha}(u_0 - u_r) = \alpha u_0 - \alpha u_r, \text{ with: } f \gg 1 \tag{2.10}$$

With $C = 1$ a constant that remains from the formalism derivation and f the ratio of the wind farm's lateral to its vertical extent. Thus, a wind deficit decay rate α, similar to the EFFWAKE model is defined. To solve Eq. 2.10 analytically, further simplifications allow to transform Eq. 2.10 to an easy to solve quadratic equation with its solutions:

$$u_{r_{1,2}}(x) = \frac{1}{2}\left(\left(c - \frac{\alpha x}{2}\right) \pm \sqrt{\left(\frac{\alpha x}{2} - c\right)^2 + 2u_0\alpha x}\right) \tag{2.11}$$

Only the positive solution of eq. 2.11 is physically relevant and will result in positive wind speeds. Parameter c outlines the initial boundary conditions, specifically for$x = 0$. These initial conditions can either be measured or calculated. A theoretical value can also be determined, for instance, for a single wind turbine, $u_r(0) \approx 0.3u_0$, which can be calculated using Betz law (Betz, 1920).

The equation 2.11 gives the remaining wind speed u_r at each location x along the wake centreline. It is assumed that the wind-deficit decay rate α, with K_m denoting the momentum transfer coefficient, remains constant over x. This equation can approximate the recovery of any reduction in wind speed, as long as the same simplifications apply that are assumed in its derivation, e.g. wind recovery behind a large tree.

2.2.4 The SWIFFR model and In-Situ Wake Data

To highlight the main commonalities and differences in the models used for the comparison, a subset of the results published in Mauz et al. (2023) is shown. The EFFWAKE and the SWIFFR models are both compared to measured in-situ data. The WIPAFF project's airborne wake data are available to the wider scientific community through the PANGAEA database (Bärfuss et al., 2019; Lampert et al., 2020). The data presented here were measured on August 8, 2017 (flight #30). The flight contains three wind farm wakes behind three adjacent wind farms, Amrumbank West (AW), Nordsee Ost (NO), Meerwind Süd/Ost (MSO) that are exemplarily shown below in Fig. 2.3. An overview of all flights performed during the WIPAFF campaign is given in Platis et al. (2018). All wind farms are located in the German Bight.

The measurements were captured with the research aircraft Dornier Do-128 of the Technical University of Braunschweig. The aircraft is equipped with sensors for temperature, humidity, pressure, and wind components. The sampling frequency is 100 Hz. Details about the installed sensors can be found in Lampert et al. (2020). The airspeed of the aircraft during the measurement flights was $66\ \mathrm{m\,s^{-1}}$.

The three subplots in Fig. 2.3 show the normalised wind velocity in the wake behind three wind farms: Amrumbank West (AW), Nordsee Ost (NO) and Meerwind Süd/Ost (MSO). The measurements (black stars) the SWIFFR model solution (black solid line), the EFFWAKE model computations (grey solid lines), and the EFFWAKE best fit (red broken line) are shown. The different EFFWAKE computations are necessary, because the model does not specify the layer thickness d (or dz as shown in Fig. 2.3) for the turbulent momentum transfer in the wind deficit decay rate $\alpha = \frac{K_\mathrm{m}}{d^2}$. Consequently, the red broken line is the EFFWAKE solution with a best fit wind deficit decay rate α_bf. These best fit decay rates are i.a. shown in Tab. 2.2 for all flights shown in Mauz et al. (2023). The derived turbulent layer thicknesses are also shown as Δz_bf. The SWIFFR model negates this uncertainty by defining the layer thickness of the turbulent momentum transfer as the rotor radius R (s.a. Eq. 2.10). The measurements are averaged wind velocities along a roughly 200 m long path in the wake minimum at the respective distant x in the wake.

Judging by the RMSD (root-mean-square deviation) alone, shown in the last column in Tab. 2.2, both the EFFWAKE and the SWIFFR models perform similarly well. However, the EFFWAKE model has the disadvantage that the turbulent layer thickness is not quantifiable, yet, important for the model to determine or predict wind farm wake lengths.

2.2.5 The super-SWIFFR Simplification

As mentioned above the Frandsen model and the SWIFFR model share the same square-root shape, while the EFFWAKE model is an exponential function. The Frandsen model is a bottom-up model by design, largely depending on the wind farm parameter C_T^* and an abstract

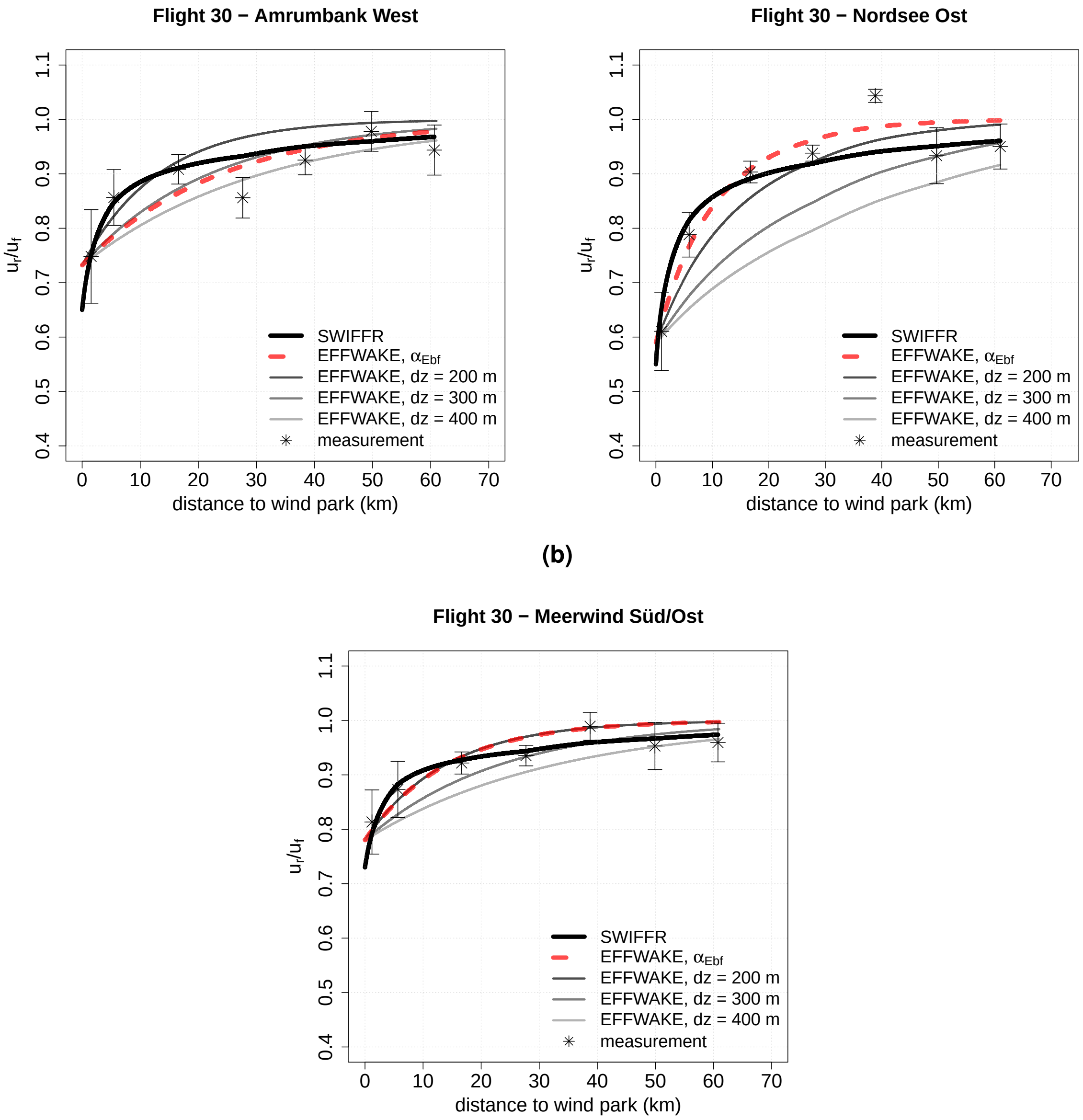

(a)

(b)

(c)

Figure 2.3: *Evaluation of the three wind farm wakes AW* ***(a)****, NO* ***(b)*** *and MSO* ***(c)*** *for flight #30. Same atmospheric boundary conditions are assumed for all three wakes, due to the vicinity of the three wind farms (Mauz et al., 2023).*

Table 2.2: *Model parameters and root-mean-square deviations (RMSD) of the EFFWAKE, the SWIFFR model for all presented cases as well as the Frandsen model (Mauz et al., 2023). With* $u_r(0)/u_f(0) = c$*, and* C_T *the thrust coefficient of the wind farm derived from the Frandsen model.*

Flight	Wind	$\mathbf{u}_*$	$\alpha_\mathbf{Ebf}$	$\alpha/\overline{u}_f$	$\Delta\mathbf{z}_\mathrm{bf}$	$c\vert_{\mathrm{x}=0}$	C_T	Π	RMSD $\cdot 10^3$
No.	farm	$[\mathrm{m\ s^{-1}}]$	$[\mathrm{h^{-1}}]$	$[\mathrm{km^{-1}}]$	$[\mathrm{m}]$	$[-]$	$[-]$	$[-]$	$[\mathrm{m\ s^{-1}}]$
EFFWAKE (best fit)									
30	AW	0.22	1.26	0.034	320	0.73	0.45	0.33	41
30	NO	0.22	2.76	0.075	170	0.59	0.49	0.29	40
30	MSO	0.22	2.26	0.061	200	0.78	0.39	0.30	27
31	AW	0.29	1.40	0.026	370	0.61	0.50	0.31	41
31	NO	0.29	3.40	0.062	180	0.63	0.49	0.31	38
31	MSO	0.29	3.60	0.066	180	0.70	0.45	0.32	22
41	GW I/II	0.21	1.00	0.022	430	0.68	0.48	0.33	39
SWIFFR			α $[\mathrm{h^{-1}}]$		R $[\mathrm{m}]$				
30	AW	0.22	13.5	0.365	60	0.65	0.45	0.29	33
30	NO	0.22	13.4	0.362	60	0.55	0.49	0.27	45
30	MSO	0.22	13.4	0.365	60	0.73	0.39	0.28	17
31	AW	0.29	17.8	0.325	60	0.35	0.50	0.18	47
31	NO	0.29	17.7	0.322	60	0.55	0.49	0.27	21
31	MSO	0.29	17.6	0.321	60	0.65	0.45	0.29	25
41	GW I/II	0.21	9.0	0.200	60	0.60	0.48	0.29	37
Frandsen					$k^* \cdot 10^5$ $[\mathrm{m^{-1}}]$		C_T^*		
30	AW				6.25	0.66	0.45	0.30	39
30	NO				5.31	0.57	0.49	0.28	45
30	MSO				7.10	0.73	0.39	0.28	20
31	AW				3.11	0.50	0.50	0.25	44
31	NO				4.70	0.57	0.49	0.28	22
31	MSO				5.50	0.65	0.45	0.29	21
41	GW I/II				3.40	0.60	0.48	0.29	47
super-SWIFFR				Λ $[\mathrm{km^{-1}}]$			C_T^*		
30	AW			0.343			0.45	0.28	37
30	NO			0.343			0.49	0.28	44
30	MSO			0.343			0.39	0.28	19
31	AW			0.343			0.50	0.28	70
31	NO			0.343			0.49	0.28	23
31	MSO			0.343			0.45	0.28	23
41	GW I/II			0.343			0.48	0.28	62

geometrical wake widening factor k^*, the SWIFFR model uses atmospheric input parameters like the mean wind velocity u_0, the friction velocity u_*, but also wind farm related parameters like the turbine radius R.

Figure 2.4 illustrates the similarity of the the Frandsen and SWIFFR model in its computed outcome. This similarity and the proportionality (s.a. Eq. 2.12) of the thrust coefficient C_T^* to the normalised initial wind deficit $c|_{\mathrm{x=0}}$, allows a parametrisation of the SWIFFR model.

$$\Pi = c|_{\mathrm{x=0}} \cdot C_\mathrm{T}^* = \text{constant} \approx 0.28 \tag{2.12}$$

The resulting first parametrisation of the SWIFFR solution utilising the thrust coefficient derived from the Frandsen solution is then calculated using:

$$u_r(x) = \frac{1}{2}\left(\left(\frac{\Pi u_0}{C_\mathrm{T}^*} - \frac{\alpha x}{2}\right) + \sqrt{\left(\frac{\alpha x}{2} - \frac{\Pi u_0}{C_\mathrm{T}^*}\right)^2 + 2u_0 \alpha x}\right) \tag{2.13}$$

An additional simplification is done. The a priori unknown parameter α is substituted by an empirical value. Therefore, an average of the normalised wind deficit decay rates Λ is introduced:

$$\Lambda = \frac{1}{6}\sum_{i=1}^{6} \frac{\alpha_i}{\overline{u}_{fi}} \approx 0.343. \tag{2.14}$$

Since Λ is the average of a normalised parameter of six wind farm wakes (excluding GW I/II), its insertion into the final equation needs to be accompanied by a velocity: the free stream velocity at hub height u_f, preferably in front of the wind farm, hence u_0. The super simplified version then becomes:

$$u_r(x) = \frac{1}{2}\left(\left(\frac{\Pi u_0}{C_\mathrm{T}^*} - \frac{\Lambda u_0 x}{2}\right) + \sqrt{\left(\frac{\Lambda u_0 x}{2} - \frac{\Pi u_0}{C_\mathrm{T}^*}\right)^2 + 2u_0^2 \Lambda x}\right) \tag{2.15}$$

Dividing by u_0 yields the relative residual wind velocities behind the wake, depending only on the thrust coefficient C_T^*:

$$\frac{u_r(x)}{u_0} = \frac{1}{2}\left(\left(\frac{\Pi}{C_\mathrm{T}^*} - \frac{\Lambda x}{2}\right) + \sqrt{\left(\frac{\Lambda x}{2} - \frac{\Pi}{C_\mathrm{T}^*}\right)^2 + 2\Lambda x}\right) \tag{2.16}$$

A graphical comparison of the super-SWIFFR model, the SWIFFR and the Frandsen model is given in Fig. 2.4. For the wind farm wakes examined in Mauz et al. (2023) the differences to the SWIFFR solution is mainly negligible. Two solutions with a notable change in RMSD (s.a. Tab. 2.2) stand out: 31 - AW and 41 - GW I/II in Fig. 2.4. The reason for the non-conformity is the very low initial wind deficit for the case of the Amrumbank West wake and difficulties in the determination of the free flow wind velocity around the Gode Windpark, also described in more detail in Mauz et al. (2023) that lead to an increased uncertainty in the normalised wind deficit decay rate and a significant deviation from the mean value of $\Lambda \approx 0.343$.

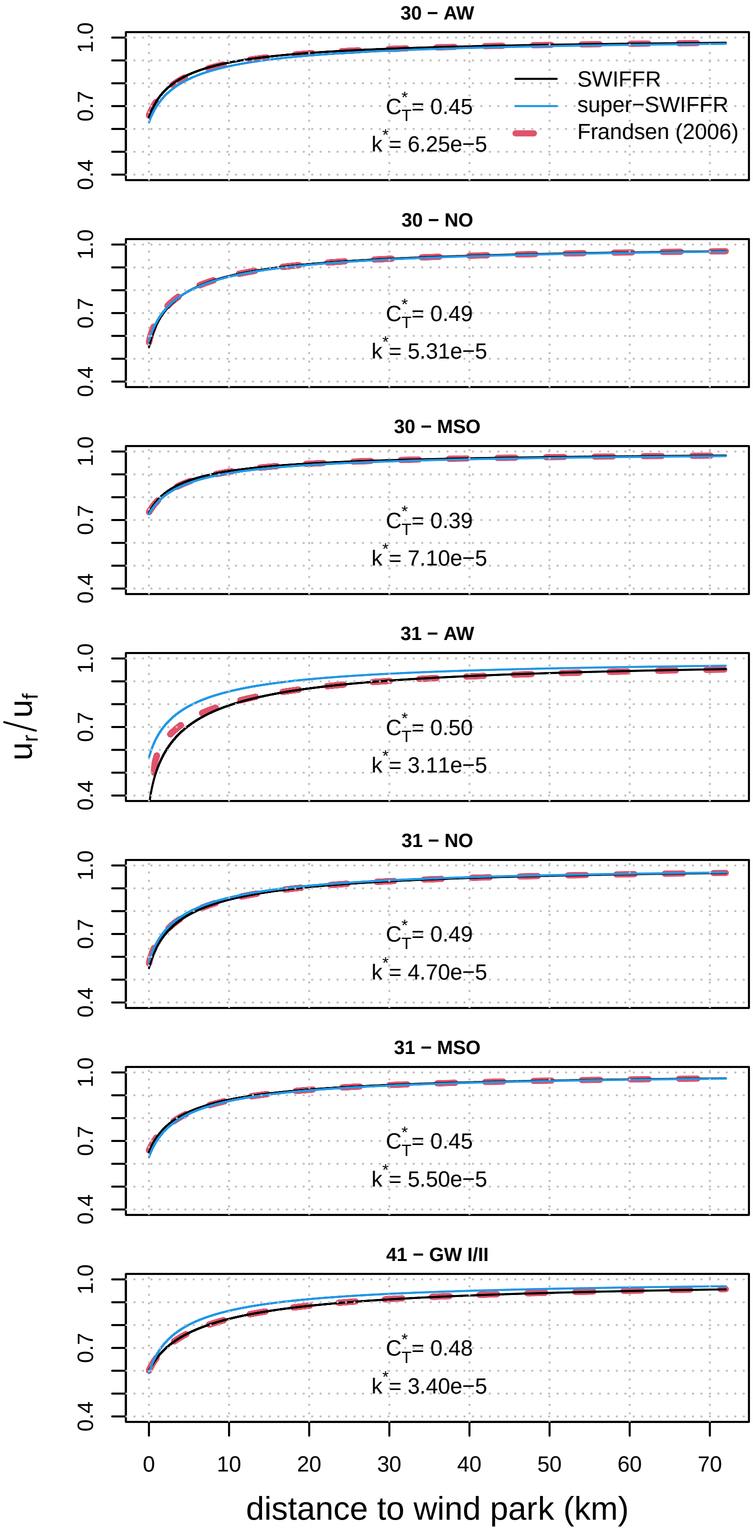

Figure 2.4: *A comparison is made between the Frandsen model Frandsen et al. (2006) and two SWIFFR models, one being a standard model and the other parametrised with dependencies derived from Table 2.2. While SWIFFR implements a top-down approach, the Frandsen model is a typical example of a bottom-up model. Despite the differences in respective derivation, the predictions of the SWIFFR and Frandsen models coincide, with the exception of Flight #31 - AW, where the initial wind deficit exceeds 50%. The figure is sourced from Mauz et al. (2023).*

2.3 High-Frequency Chilled-Mirror Hygrometer for Fixed-Wing UAS

Wind turbine wake structures interact with buoyant movement of air parcels, depending on the atmospheric, thermal conditions along the wake. This is especially relevant behind offshore wind farms. With increasing wind turbine dimensions, in particular the rotor diameters, the mixing of different layers of the lower atmosphere needs to be considered. Wind turbines essentially force density-driven buoyant movement. Aside the ambient temperature of these air parcels the water vapour content is the density defining parameter. Information about the change of water content, e.g. in forced convection, is critical to accurately describe and model the influence of density-driven structures on wind farm wakes.

However, measuring turbulent fluctuations of humidity in the air has always been a complicated and expensive endeavour. Especially for mobile UAS (fixed-wing) platforms there are no light-weight sensors available. Therefore, the in-house development of a relatively cheap and light-weight sensor has been initiated. The first onboard measurements of the chilled-mirror hygrometer (CMH) were made in the fetch of a meteorological tower (met-tower) located at the WINSENT wind energy test site at the Swabian Alb near the town of Donzdorf in south-west Germany. The UAS captured data from 20 to $210\ \mathrm{m\ a.g.l.}$ The met-tower is equipped with Thies thermo- and hygrometers at around $20, 40, 80$ and $100\ \mathrm{m\ a.g.l.}$ The CMH data was compared to the data of these sensors and an additional (capacitive) thermo- and hygrometer sensor (SHT31) that is equipped on the UAS. This sensor set-up allows for the following evaluations:

- Comparison between the CMH and the (slower) capacitive sensor, both mounted on the UAS measuring the same spatial series.
- Comparison of the measured average along a straight flight path (measurement leg) in the fetch of the met-tower against the sensors mounted on the met-tower in different altitudes.
- Evaluation of the high-frequency response of the CMH along a flight leg.

The measurements were made on 23 August 2019, on a sunny day from 10:00 to 12:00 UTC. During the flights, the stratification of the atmosphere was slightly unstable. The surface temperature was $18.5^\circ\mathrm{C}$. The main wind direction is 100° with an average horizontal wind speed of $v_h \approx 5\ \mathrm{m\ s^{-1}}$.

The results of the direct comparison of the CMH against a state-of-the-art capacitive hygrometer sensor (SHT31) are shown in Fig. 2.5a and Fig. 2.5b. The dew point temperature is calculated from the SHT31 measurement signal of the ambient temperature and the relative humidity. Both figures show a constant offset of the CMH sensor, which is on purpose. A small under-cut of the dew point temperature criterion assures a stable layer of dew and prevents the PID controller from oscillating. The offset can be subtracted from the measurement in the post-processing, if absolute values are needed. Aside the offset, both sensors equipped on the UAS measure the same signal. The spatial series of the CMH and SHT31 sensor shown in Fig. 2.5a map the same peaks and trends, thus the signal varies together along a $700\ \mathrm{m}$ flight leg. The CMH shows more fluctuations in the dew point temperature. To evaluate the

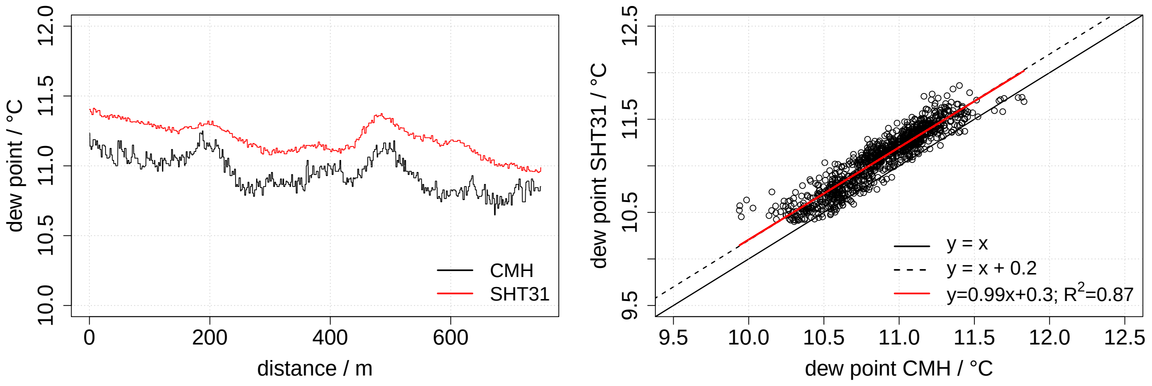

(a) **(b)**

Figure 2.5: ***(a)*** *Spatial series along a single flight leg of the CMH (black line) and the SHT31 capacitive sensor (red line) mounted on the sensor dome of the UAS. Noticeable is a constant offset between the sensors. Both sensors vary together and show the same peaks in the dew point measurements and show the same trends in the measurement.*
(b) *Scatter plot of all measurements in a total of 30 legs at different heights (20, 40, 80 and 100 m a.g.l). The measurements are block averaged over 100 data points (1 s). The black solid line shows a 1:1 relationship. The black dashed line takes into account the constant offset between the two sensors. The red solid line is the true linear relationship between the two sensors. Both figures taken from Mauz et al. (2020).*

fluctuations and to exclude noise as a source, the high-frequency response of the sensor will be evaluated further below. The scatter plot compares the on-board dew point measurement of both sensors over all flight legs. From this plot it is concluded that the CMH measures a low-frequency dew point response at least as good as its capacitive counter-part. As an additional low-frequency response validation the CMH data are compared against met-tower data. Figure 2.6 shows the leg averages of the CMH measurement (black dots) at each altitude, the SHT31 equivalent (red circles) and the measurements obtained from the instruments mounted on the met-tower (orange dots) approximately $50\ \mathrm{m}$ downstream of the UAS flight path. As expected, the SHT31 has a slight offset compared to the CMH. The measured dew point at the tower is always in the range of $\pm 0.5^\circ\mathrm{C}$ relative to the altitude average of the UAS measurements. Considering that the UAS is flying in the fetch of the met-tower the results are in good agreement. The met-tower averages are calculated from a four minute long time series, in which the UAS was flying at the same altitude.

For the high-frequency response evaluation of the in-house made CMH sensor, the power spectra of the data obtained at $20, 30, 40$ and $60\ \mathrm{m\ a.g.l}$ are calculated and averaged. Figure 2.7a shows the spectral response of the CMH. The resulting spectrum shows resolved turbulence in the inertial sub-range up to about $10\ \mathrm{Hz}$. The decisive criterion is the black curve following the Kolmogorov (1941) five-thirds law (parallel to red line). This implies that at a UAS equipped with the CMH sensor and a cruising speed of $\approx 20\ \mathrm{m\ s^{-1}}$, eddies of $2\ \mathrm{m}$ size can be resolved.

Complementing the frequency response, the structure function D of a single leg is exemplarily calculated (Fig. 2.7b). The eddy-size distribution of a turbulent flow in the inertial sub-range, or the local structure of a turbulent flow, was first and foremost quantified using the (auto-)

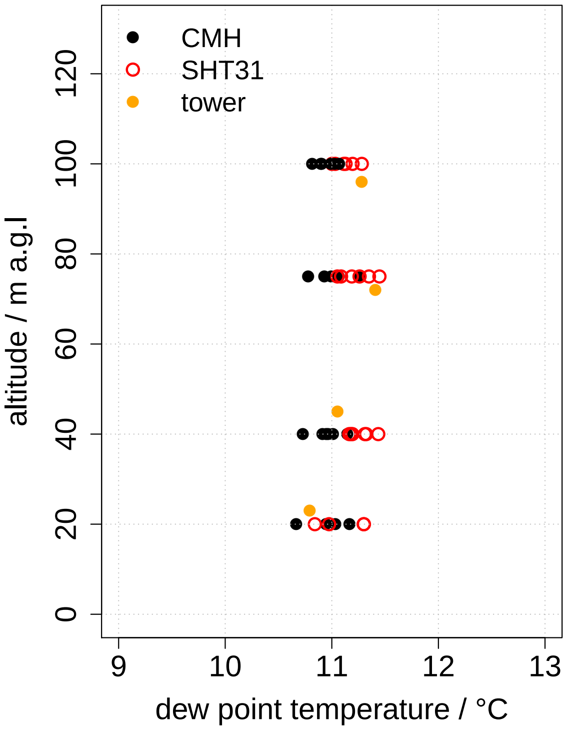

Figure 2.6: *Measured dew point temperatures with an SHT31 capacitive hygrometer and the CMH on board the MASC-3 UAS. The measurements marked in orange are from capacitive hygrometers that are mounted on a meteorological tower about 50 m farther downstream (Mauz et al., 2020).*

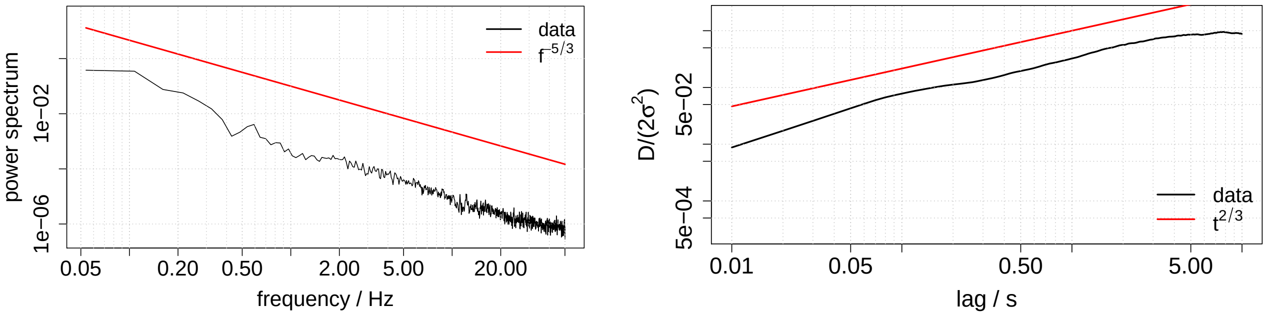

(a) **(b)**

Figure 2.7: (a) *Frequency (f) response from an averaged power spectrum calculated from 14 measurement legs distributed over the first four altitudes.*

(b) *Example structure function D of a measurement along a flight path in 120 m a.g.l in front of the meteorological tower. The red line is the reference delay time $^{2/3}$. Figures taken from Mauz et al. (2020).*

structure function (Kolmogorov, 1941), for in-practise use in high-frequency atmospheric measurements see also Bange (2009) and Wildmann et al. (2013).

$$D_\phi(\tau) = \frac{1}{D-\tau} \int_0^{D-\tau} dt \left[\phi(t+\tau) - \phi(t)\right]^2 \tag{2.17}$$

where τ is the lag or shift, ϕ is the physical quantity, D is the total length of the time series and t is the time.

To facilitate interpretation of the structure functions, they can be normalised by dividing by twice the variance of the corresponding time series:

$$\frac{D_\phi}{2\sigma^2} = \begin{cases} 0 & \text{: fully correlated} \\ 1 & \text{: non-correlated} \\ 2 & \text{: fully anti-correlated} \end{cases} \tag{2.18}$$

Ideally, for a high frequency instrument, the data examined will follow the $t^{2/3}$ line with the least possible delay, since the lowest point of parallelism is equal to the time constant of the sensor.

The structure function in Fig. 2.7b shows an almost parallel distribution to the Kolmogorov distribution (red line). Significant deviations from this line are observed for $\tau < 0.1\ \mathrm{s}$ or corresponding to a frequency of $1/\tau = 10\ \mathrm{Hz}$. This corresponds to the characteristics observed in the averaged spectra shown in Fig. 2.7a. At the low frequency end, the Kolmogorov inertial subrange of locally isotropic turbulence remains at about $5\ \mathrm{s}$. At an average flight speed of $18\ \mathrm{m\,s^{-1}}$ this corresponds to vortices with diameters of $90\ \mathrm{m}$. Due to the relatively low flight altitude this may mark the beginning of the turbulent production region. The heterogeneous inflow due to the complex terrain of the Swabian Alb may explain the small deviations from the 'ideal' Kolmogorov distribution between $0.1\ \mathrm{s}$ and $5\ \mathrm{s}$.

Measuring the Structure Parameter C_q^2 with the In-House CMH

At a measurement campaign at the meteorological Richard-Aßmann-Observatory in Lindenberg, Germany, on the last day of July 2020, the CMH prototype was flown in front of a met-tower at an altitude of $50\ \mathrm{m\ a.g.l}$ at which a LI-COR LI-7500RS open-path gas analyser was installed. This measurement campaign provided the opportunity to compare the CMH to another high-frequency hygrometer. The LI-COR sensor measures water vapour fluctuations at a sampling rate of $20\ \mathrm{Hz}$. Therefore, it is possible to calculate the structure parameter C_q^2 from its measurements. This result is then compared to the calculated structure parameter from the UAS CMH measurements at the same altitude. The measurement campaign allowed a unique comparison of the two measurement systems with regard to the structure parameters.

To calculate the structure parameter, the structure function D_q for the specific humidity q is calculated as shown in Eq. 2.17, while the temporal time shift yields to a spatial shift r:

$$r = \frac{n}{f_s} v_\mathrm{g} \tag{2.19}$$

Table 2.3: *Quantitative overview of the derived parameters from the structure functions shown in Fig. 2.8 and the variance (σ^2) of the underlying data.*

Sensor	C_q^2 $[\mathrm{kg}^2\ \mathrm{kg}^{-2}\mathrm{m}^{-2/3}]$	r_{min} [m]	r_{max} [m]	σ^2 [kg/kg]
LI-COR	$2.25e^{-10}$	2	7	$5.39e^{-09}$
CMH	$6.5e^{-11}$	1.5	3	$1.19e^{-09}$

with n the number of data points associated with the shift r and v_{g} the ground speed of the UAS (the horizontal wind speed v_{h} is used for the tower measurements, respectively), f_s is the sampling rate of the sensor. The obtained lag is then normalised by the 2/3 law expression following Kolmogorov (1941) (Platis et al., 2017).

$$C_{\mathrm{q}}^2 = \left\langle D_{\mathrm{q}}(r) r^{-2/3} \right\rangle_{r_{\mathrm{min}}, r_{\mathrm{max}}} \tag{2.20}$$

Similar studies were done by van den Kroonenberg et al. (2012); Braam et al. (2014, 2016), whereas they used mean structure parameters, in the presented evaluation in this dissertation only one of many measurements is shown to map a quick comparison of the structure parameter obtained by the CMH and the LI-COR sensor.

Figure 2.8 shows the normalised structure function according to Eq. 2.20. The graph to the left (a) is calculated from LI-COR data, the one to the right (b) from CMH in-situ data. The MASC-3 UAS data was captured around $1\ \mathrm{km}$ north the met-mast, with an average wind direction of $300°$. This covered roughly the inflow (fetch) of the met-mast. While not identical the flow conditions should be comparable, especially due to the homogenous terrain around the Lindenberg observatory. The LI-COR data that was used corresponds to a fetch of about $1.1\ \mathrm{km}$ with a relatively stable horizontal mean wind speed of $v_{\mathrm{h}} = 4.5\ \mathrm{m\,s}^{-1}$. The plateau in the line graph, i.e. its value, gives the structure parameter for the specific humidity for each measurement. The lengths of the minimum and maximum lag mark the beginning and the end of the plateau, defining the minimum and maximum characteristic length of the present turbulent eddies. A quantitative comparison is given in Tab. 2.3.

To make the scales in Fig. 2.8 (e.g. the lags on the x axis) comparable it is necessary that the average wind speed for the met-mast measurement is roughly steady and does not vary too much, otherwise the spatial shift (lag) does no longer correspond to the 'eddies' measured in the time series which relationship is resolved using Eq. 2.19 ($v_{\mathrm{g}} \to v_{\mathrm{h}}$). Therefore, the structure function in Fig. 2.8a was calculated from a time frame with low wind speed variance.

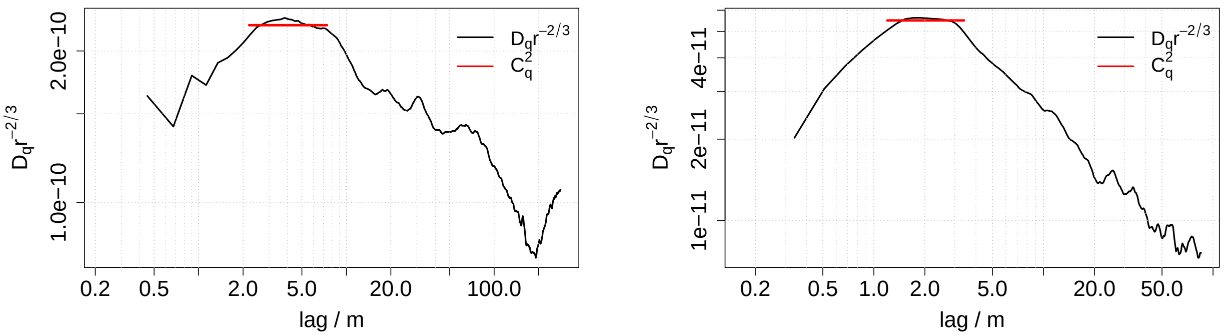

(a) **(b)**

Figure 2.8: *Normalised structure function calculated from the LI-COR sensor measurements* ***(a)*** *and from the CMH measurements from an approximately 450 m long part of a flight leg* ***(b)****. The structure parameter C_q^2 is the value of the plateau indicated by the read line. The lengths of the minimum and maximum lag mark the beginning and the end of the plateau, defining the minimum and maximum characteristic length of the present turbulent eddies.*

3 Discussion

The importance and necessity of high-frequency sensors to measure small (turbulent) structures in the atmosphere becomes apparent throughout this thesis, and is outlined in Sec. 2.1 and Sec. 2.3. Only through an interplay of all high-resolution components blade-tip vortices could be resolved. The reduced pressures in the close-up area behind WTs, and in particular the pressure distribution in detached blade-tip vortices, make the use of a high-resolution humidity sensor additionally interesting. The pressure fluctuations during the passage of a blade-tip vortex can influence the measurement of the wind speed (true air speed). However, since a quotient of the tangential velocities is used in the evaluation (Eq. 2.2), and the measurements are also spatially very close to each other, an influence on the calculation of the core radius is negligible. The method developed and presented for measuring blade-tip vortices exploits simple geometric relationships during the measurement flight. This makes the method easy to follow. The measurement method opens up possibilities for investigating vortex ageing and the role of vortex shielding when considering the momentum flow into the wake of a WT. A series of blade-tip measurements at different distances from the WT hub could be evaluated under the assumption that all blade-tip vortices are of the same energy and origin. Which is given at constant wind speed and constant rotation of the wind turbine blades. The only prerequisite must be that one of the vortices at each distance is flown through under the condition $r < r_\mathrm{c}$, i.e. a distance to the vortex centre smaller than the vortex core diameter.

While the study attached in App. A.1 is concerned with quantifying artificial vortices, i.e. turbulence added by the WT itself, the second wind energy related publication, integrated in App. A.2, is devoted to the wind farm wake interaction with atmospheric turbulence, in particular the role and modelling of vertical momentum influx and the wind velocity recovery in wind farm wakes. It has been shown that the wind speed recovery is rather described in a square-root manner (SWIFFR) than an exponential function (EFFWAKE), and therefore the gains in practical use states an improvement in wind wake modelling. The SWIFFR model is derived from Reynolds-averaged Navier-Stokes equations and describes the wind speed recovery in a one-dimensional flow, at hub height. For the derivation some simplifications had to be made, yet, the results look promising. The resulting analytical solution for the SWIFFR model can be used with different a priori known input parameters as the friction velocity, the mean incoming flow velocity, the initial wind velocity deficit, the rotor diameter of the WTs installed in the evaluated wind farm, and the dimensions of the wind farm. The availability of these parameters allows the calculation of a very specific wind deficit decay rate α, also shown in Eq. 2.10. If the required data are available, the momentum transfer coefficient (and therefore α) can be stability adjusted (Eq. 2.7). A main advantage of the presented analytical model (and a model in general) is the simplification of an otherwise complex phenomenon. Therefore, the necessity to obtain these parameters may negate the purpose of the analytical model in the first place, e.g. for wind farm wake length assessment.

Through exploitation of known correlations and parametrisation, the initial wind velocity deficit and its decay constant α, the substitutions Π and Λ were introduced. At the same time the wind farm thrust coefficient is replacing the measured initial wind deficit. Thrust coefficients are widely used in the wind energy community and are more informative as the initial drop in wind velocity behind a wind farm. These steps altogether increase the ease of use of the SWIFFR model. Figure 2.4 also illustrates the difference between the SWIFFR model and the simplified super-SWIFFR approach. The difference between the two is mostly negligible. An interesting exception is the solution for the GW I/II wind farms. Table 2.2 shows a normalised wind deficit decay constant $\alpha/\overline{u}_f$ of 0.200 for the GW I/II measurements. The super-SWIFFR solution is using the averaged value $\Lambda = 0.343$ for its calculation. This is an increase to approximately $170\ \%$. Despite this difference between the measured to the modelled parameter, the super-SWIFFR solution deviates only about $5\ \%$. Therefore, it seems on the one hand the thrust coefficient C_T^*, or alternatively the initial wind farm wake deficit, are the wake defining parameter, and α may only play a secondary role. The difference in predicted wake length in this case is $50\ \mathrm{km}$ for the super-SWIFFR and $60\ \mathrm{km}$ for the SWIFFR and Frandsen model, with the wake length criterion being reaching $0.95\ \%$ of the inflow velocity u_0 again. Whether the observed difference in wake length prediction is significant depends on the research question, e.g. the wake interaction of neighbouring wind farms. On the other hand, another wake length prediction improvement, compared to the EFFWAKE model, is the square-root shape of the SWIFFR models. It is expected that the development of a turbulent boundary layer behind an obstacle like a wind farm or a wind turbine develops in a square-root manner Garratt (1987, 1994); Hanna (1987). By essentially only one necessary input, the thrust coefficient of the wind farm, the super-SWIFFR solution is easy to use, but can also be tuned by additional informations, e.g. atmospheric stability weighting Λ and increasing or decreasing the wind deficit decay along the wake. π is considered to be independent of atmospheric influence, since it is the ratio of the thrust coefficient and the initial wind deficit directly behind the WT. It may vary only very little depending on the operating conditions of the turbine. Therefore, a further parametrisation could be done by substituting Π:

$$\Pi = \frac{1}{2\sqrt{\pi}}. \tag{3.1}$$

Now, one constant is substituted by a more common one and Eq. 2.16 looks more appealing.

To additionally enable an evaluation of the role of moisture fluxes in WT wake behaviour in the future, a capable sensor had to be developed. The resulting prototype CMH is able to resolve turbulent humidity related structures (as shown in Fig. 2.7) and measures absolute mean dew point temperatures with an accuracy of about $\pm 0.1\ \mathrm{K}$ (Mauz et al., 2020). If homogeneous terrain and homogeneous inflow conditions are assumed for the day of the comparison measurement, it seems that the sensor might not capture turbulence along the complete inertial sub-range, according to Kolmogorov (1941) $-5/3$ law of turbulence decay. Nevertheless, the main goal of the CMH prototype has been to provide a working proof of concept, which still shows some imperfections.

The LI-COR and the CMH sensor can both provide a structure parameter for the specific humidity q. However, the lag length over which the parameter is calculated (length of the plateau) differs. The LI-COR measurement implicates a turbulent length scale of $5\ \mathrm{m}$ ($r_{\mathrm{max}} - r_{\mathrm{min}}$), $8\ \mathrm{m}$ if the plateau is stretched up to the $10\ \mathrm{m}$ lag mark. The CMH shows a smaller length scale ($1.5\ \mathrm{m}$) which most likely is caused by the sensors possible inability to capture a specific frequency range (corresponding to a specific eddy size). This could be related to the small dent at $0.5\ \mathrm{Hz}$ in Fig. 2.7a. A possible argument for a lack of measured variance is the discrepancy between the absolute values of the measured C_{q}^2 parameter (s.a. Tab. 2.3) with a difference of $\approx 1.5e^{-10}$ in value, one order of magnitude separates these values. Due to the homogeneous terrain at the measurement site, it cannot be explained solely by slightly different flow structures, which always occur, especially when comparing line data from a moving measurement platform with stationary data. Further development of the CMH could therefore improve the measurement. However, the measured order of magnitudes $\mathcal{O}(-11)$ to $\mathcal{O}(-9)$ have been well documented by millimetre-wave scintillometry by Ward et al. (2015).

4 Summary and Outlook

In this thesis wind energy research, based on in-situ UAS measurements covers turbulence from measuring individual vortices in a WT wake, up to an analytical description of the centre-line of a wind farm wake. By creating a measurement technique to study detached blade-tip vortices and calculating their core radius, the first research question (*How large are detached blade-tip vortices from wind turbines? And what is their influence on the wake?*) stated in Ch. 1 could be answered. Those results from Mauz et al. (2019) were obtained by Cormier et al. (2020) to sharpen CFD calculations and to further understand the role of blade-tip vortices in the WT wake development. Ultimately, measurements go hand-in-hand with other scientific methods or disciplines.

To answer the second research question (*How does the wind deficit recover behind WTs?*), various established models as well as newer, empirical solution approaches were compared with the measured data. Most models, which originate from the engineering sciences, are bottom-up models and thus describe the recovery of wind speeds behind WTs from the perspective of a WT. Atmospheric parameters, e.g. thermal stratification, momentum transfer or shear stress, are not taken into account, and are mostly assumed. This means that the transferability to wakes under real conditions is limited. And in fact, those models did not describe the UAS based wake measurements properly. This dissatisfaction led to a search for a model that could better accommodate the data. The EFFWAKE model by Emeis (2010) is a prominent model that uses atmospheric parameters to describe the change in atmospheric flow caused by a WT. Like the SWIFFR model, the EFFWAKE model can therefore be categorised as a top-down model. But the similarities only begin here: many of the parametrisations used by Emeis (2010) in EFFWAKE can also be found in the SWIFFR model. However, the approach is different. While the EFFWAKE model is based on a Lagrangian, time-dependent approach to an air parcel moving within a WT wake, the SWIFFR model is based on an Eulerian, steady-state simplification of the Reynolds averaged NS equations, describing the same wake. The differences in both model approaches and how the results compare are shown in Sec. 2.2.

The super-SWIFFR solution can be considered as a step to combine both, bottom-up and top-down approaches. Usually bottom-up models provide a thrust coefficient of the modelled WT, thus, this is a parameter that is most commonly available. What the super-SWIFFR adds as a top-down model is the atmospheric parameters disguised in the Λ and to an extent, the Π parameter. On a side note: In future studies the validity of Eq. 3.1 should be tested.

A benefit of the super-SWIFFR solution in a real world scenario would be the calculation of wind farm wakes in a quick assessment. Usually, Wind farm workloads are calculated and simulated in WRF models using WFP (wind farm parametrisation) (Siedersleben et al., 2018; Tomaszewski and Lundquist, 2020). While WRF simulations are nowhere near as computational expensive as LES calculations, it would still be beneficial to have an analytical solution for any weather condition that would forecast wind farm wakes. Also, for the SWIFFR model to become a reliable wake length forecasting tool, e.g. for off-shore wind farms, more measurements and evaluations are needed to concretise the parametrisation of factors (e.g. Λ and Π). For a proof of concept this method is fine, however, to provide a broader field of applicability to wake data, further field campaigns are desirable.

Now that research question two has been answered by describing the wind velocity deficit in a wind turbine wake or that of a wind farm using the atmospheric momentum flux in a parametrised form, a new question arose: *How would wind deficit decay look like in a density-driven buoyant wake?* Especially in off-shore wind farm wakes, where large volumes of air, distributed over two hundred meters in height are mixed. To answer this question using UAS technology, turbulent density fluxes need to be measurable. The density of air is depending on the ambient temperature, the atmospheric pressure and the moisture content of the air parcel. Since only two out of the three parameters are available in a necessary temporal resolution of at least 5 to $10\ \mathrm{Hz}$ using small-UAS based in-situ sensing, the need for a high frequency moisture sensor was given. This leads to the final research question four: *How to measure turbulent moisture flux with UAS?*

Surely, sensor technology is constantly developing further. Humidity sensors will get smaller and lighter, and UAS technology will improve, too. Thus, in the future there will be most certainly a high-frequency solution for humidity measurements available that is applicable on small airborne platforms. Yet, at the time of this study no commercially available sensor for UAS high-frequency measurements was available. The in-house built CMH sensor is the only possible solution to investigate turbulent humidity phenomena in the lower atmospheric boundary layer using UAS. In general, a humidity sensor, providing high-frequency data, is urgently needed to investigate the role of turbulent humidity and density fluxes in the lower atmosphere. An interesting field of application is the investigation of forced density variations, as introduced above. To allow studies that include turbulent density variations of the air in the wake of a WT or wind farm, buoyancy has to be considered. A smaller part in this thesis covers the sensor design and construction of a high-frequency humidity sensor for UAS implementation. The CMH sensor was tested against state-of-the art capacity humidity sensors. The measured low-frequency signal of the dew point temperature confirms that the first prototype of the sensor can measure the atmospheric ambient dew point. It has been shown that the measurement principle, i.e. using a TEC cooling a gold mirror, can resolve measurements up to $10\ \mathrm{Hz}$. This is sufficient to be able to calculate turbulent parameters as C_q^2 of the inflowing air. Yet, the development of this sensor is not finished, and there is still room for improvements, as has been shown in Sec. 2.3. With the next iteration of the CMH, this sensor type will be standard on every MASC measurement platform.

In all cases, measurements were the basis for either an evaluation method, an analytical model or a sensor development that could not have been realised without the respective in-situ UAS data. The thesis draws on findings from various research fields, such as wind tunnel experiments, LES studies, etc. which collectively set the stage for a scientific environment culminating in the results presented here. These outcomes address three of the four the research questions as outlined in the introduction.

References

Andersen, S., Sørensen, J., Ivanell, S., and Mikkelsen, R. Comparison of engineering wake models with CFD simulations. volume 524. IOP Publishing, 2014. doi: 10.1088/1742-6596/524/1/012161. URL `http://indico.conferences.dtu.dk/conferenceDisplay.py?confId=138`.

Bange, J. *Airborne Measurement of Turbulent Energy Exchange Between the Earth Surface and the Atmosphere*. Sierke Verlag, Göttingen, 2009. 174 pp.

Bange, J. and Roth, R. Helicopter-borne flux measurements in the nocturnal boundary layer over land – a case study. *Boundary-layer Meteorology*, 92:295–325, 08 1999. doi: 10.1023/A:1002078712313.

Bärfuss, K., Hankers, R., Bitter, M., Feuerle, T., Schulz, H., Rausch, T., Platis, A., Bange, J., and Lampert, A. In-situ airborne measurements of atmospheric and sea surface parameters related to offshore wind parks in the German Bight. 2019. doi: 10.1594/PANGAEA.902845. URL `https://doi.org/10.1594/PANGAEA.902845`.

Betz, A. Das Maximum der theoretisch möglichen Ausnützung des Windes durch Windmotoren. *Zeitschrift für das gesamte Turbinenwesen*, 26:307–309, 1920.

Bodini, N., Zardi, D., and Lundquist, J. K. Three-dimensional structure of wind turbine wakes as measured by scanning lidar. *Atmospheric Measurement Techniques*, 10(8):2881–2896, 2017. doi: 10.5194/amt-10-2881-2017. URL `https://www.atmos-meas-tech.net/10/2881/2017/`.

Braam, M., Beyrich, F., Bange, J., Platis, A., Martin, S., Maronga, B., and Moene, A. F. On the discrepancy in simultaneous observations of the structure parameter of temperature using scintillometers and unmanned aircraft. *Boundary-Layer Meteorology*, 158(2):257–283, 2016. doi: https://doi.org/10.1007/s10546-015-0086-9.

Braam, M., Moene, A. F., and Beyrich, F. Variability of the structure parameters of temperature and humidity observed in the atmospheric surface layer under unstable conditions. *Boundary-Layer Meteorology*, 150:399–420, 2014. URL `https://doi.org/10.1007/s10546-013-9882-2`.

Burnham, D. C. and Hallock, J. N. Chicago monoacoustic vortex sensing system. *Wake Vortex Decay*, 4:590–599, 1982.

Canadillas, B., Foreman, R., Barth, V., Siedersleben, S., Lampert, A., Platis, A., Djath, B., Schulz-Stellenfleth, J., Bange, J., Emeis, S., and Neumann, T. Offshore wind farm wake recovery: Airborne measurements and its representation in engineering models. *Wind Energy*, 23, 02 2020. doi: 10.1002/we.2484.

Cormier, M., Bühler, M., Mauz, M., Lutz, T., Bange, J., and Krämer, E. CFD prediction of tip vortex aging in the wake of a multi-MW wind turbine. *Journal of Physics: Conference Series*, 1618, 2020. URL `https://iopscience.iop.org/article/10.1088/1742-6596/1618/6/062029/pdf`.

De Bruin, H. A. R., Kohsiek, W., and Van Den Hurk, B. J. J. M. A verification of some methods to determine the fluxes of momentum, sensible heat, and water vapour using standard deviation and structure parameter of scalar meteorological quantities. *Boundary-Layer Meteorology*, 63(3):231–257, Mar 1993. ISSN 1573-1472. doi: 10.1007/BF00710461. URL `https://doi.org/10.1007/BF00710461`.

Emeis, S. A simple analytical wind park model considering atmospheric stability. *Wind Energy*, 13(5):459–469, 2010. doi: 10.1002/we.367. URL `https://onlinelibrary.wiley.com/doi/abs/10.1002/we.367`.

Emeis, S. *Wind Energy Meteorology*. Springer, Heidelberg, Germany, 2017. doi: https://doi.org/10.1007/978-3-319-72859-9.

Emeis, S. Analysis of some major limitations of analytical top-down wind-farm models. *Boundary-Layer Meteorology*, 01 2022. ISSN 1573-1472. doi: 10.1007/s10546-021-00684-4. published online 24. Jan. 2022.

Emeis, S., Siedersleben, S., Lampert, A., Platis, A., Bange, J., Djath, B., Schulz-Stellenfleth, J., and Neumann, T. Exploring the wakes of large offshore wind farms. *Journal of Physics Conference Series*, 753:092014, 10 2016. doi: 10.1088/1742-6596/753/9/092014.

Fischenberg, D. Charakterisierung von wirbelschleppen aus in-situ-flugmessdaten der falcon d-cmet. Technical report, DLR Institut für Flugsystemtechnik, 2011. URL `https://elib.dlr.de/70300/`.

Frandsen, S. T. *Turbulence and turbulence-generated structural loading in wind turbine clusters*. Risoe National Lab., Roskilde, Denmark. Wind Energy Dept.; Danmarks Tekniske Univ., Kgs. Lyngby, Jan 2007.

Frandsen, S., Barthelmie, R., Pryor, S., Rathmann, O., Larsen, S., Højstrup, J., and Thøgersen, M. Analytical modelling of wind speed deficit in large offshore wind farms. *Wind Energy*, 9 (1-2):39–53, 2006. doi: 10.1002/we.189.

Fuertes, F., Markfort, C., and Porté-Agel, F. Wind turbine wake characterization with nacelle-mounted wind lidars for analytical wake model validation. *Remote Sensing*, 10:668, 04 2018. doi: 10.3390/rs10050668.

Fujiwara, M., Shiotani, M., Hasebe, F., Vömel, H., Oltmans, S. J., Ruppert, P. W., Horinouchi, T., and Tsuda, T. Performance of the Meteolabor “Snow White” chilled-mirror hygrometer in the tropical troposphere: Comparisons with the Vaisala RS80 A/H-Humicap sensors. *Journal of Atmospheric and Oceanic Technology*, 20(11):1534–1542, 2003. doi: 10.1175/1520-0426(2003)020⟨1534:POTMSW⟩2.0.CO;2.

Garratt, J. R. The stably stratified internal boundary layer for steady and diurnally varying offshore flow. *Boundary-Layer Meteorology*, 38:369–394, 1987. doi: https://doi.org/10.1007/BF00120853.

Garratt, J. *The Atmospheric Boundary Layer*. Cambridge Atmospheric and Space Science Series. Cambridge University Press, 1994. ISBN 9780521467452. URL `https://books.google.de/books?id=xeEVtBRApAkC`.

Hajra, B. A review of some recent studies on buoyancy driven flows in an urban environment. *International Journal of Atmospheric Sciences*, 2014, 09 2014. doi: 10.1155/2014/362182.

Hanna, S. R. An empirical formula for the height of the coastal internal boundary layer. *Boundary-Layer Meteorology*, 40:205–207, 1987. doi: https://doi.org/10.1007/BF00140077.

Jensen, N. *A note on wind generator interaction*. Number 2411 in Risø-M. Risø National Laboratory, 1983. ISBN 87-550-0971-9.

Kaldellis, J., Triantafyllou, P., and Stinis, P. Critical evaluation of wind turbines' analytical wake models. *Renewable and Sustainable Energy Reviews*, 144:110991, 07 2021. doi: 10.1016/j.rser.2021.110991.

Katić, I., Højstrup, J., and Jensen, N. O. A simple model for cluster efficiency. In *W. Palz, & E. Sesto (Eds.), EWEC'86. Proceedings. Vol. 1 (pp. 407-410)*, 1987.

Kim, Y., Jost, E., Bangga, G., Weihing, P., and Lutz, T. Effects of ambient turbulence on the near wake of a wind turbine. *Journal of Physics: Conference Series*, 753(3):032047, 2016. URL `http://stacks.iop.org/1742-6596/753/i=3/a=032047`.

Kolmogorov, A. N. The Local Structure of Turbulence in Incompressible Viscous Fluid for Very Large Reynolds' Numbers. In *Dokl. Akad. Nauk SSSR*, volume 30, pages 301–305, 1941.

Lampert, A., Hartmann, J., Pätzold, F., Lobitz, L., Hecker, P., Kohnert, K., Larmanou, E., Serafimovich, A., and Sachs, T. Comparison of Lyman-alpha and LI-COR infrared hygrometers for airborne measurement of turbulent fluctuations of water vapour. *Atmospheric Measurement Techniques*, 11(4):2523–2536, 2018. doi: 10.5194/amt-11-2523-2018. URL `https://www.atmos-meas-tech.net/11/2523/2018/`.

Lampert, A., Bärfuss, K. B., Platis, A., Siedersleben, S. K., Djath, B., Cañadillas, B., Hankers, R., Bitter, M., Feuerle, T., Schulz, H., Rausch, T., Angermann, M., Schwithal, A., Bange, J., Schulz-Stellenfleth, J., Neumann, T., and Emeis, S. In-situ airborne measurements of atmospheric and sea surface parameters related to offshore wind parks in the German Bight. *Earth System Science Data*, 2020.

Lignarolo, L., Ragni, D., Krishnaswami, C., Chen, Q., Simão Ferreira, C., and van Bussel, G. Experimental analysis of the wake of a horizontal-axis wind-turbine model. *Renewable Energy*, 70:31 – 46, 2014. ISSN 0960-1481. doi: https://doi.org/10.1016/j.renene.2014.01.020. URL `http://www.sciencedirect.com/science/article/pii/S0960148114000494`.

Mauz, M., Rautenberg, A., Platis, A., Cormier, M., and Bange, J. First identification and quantification of detached-tip vortices behind a wind energy converter using fixed-wing unmanned aircraft system. *Wind Energy Science*, 4(3):451–463, 2019. doi: 10.5194/wes-4-451-2019. URL `https://www.wind-energ-sci.net/4/451/2019/`.

Mauz, M., van Kesteren, B., Junkermann, W., zum Berge, K., Schön, M., Platis, A., and Bange, J. Miniature high-frequency chilled-mirror hygrometer for atmospheric measurements aboard fixed wing UAS. *Meteorologische Zeitschrift*, 29:439–449, 07 2020. doi: 10.1127/metz/2020/1026. URL `http://dx.doi.org/10.1127/metz/2020/1026`.

Mauz, M., Emeis, S., Hoeckh, F., van Kesteren, B., Platis, A., and Bange, J. Towards higher accuracy in wind farm deficit decay modelling - a comparison. *Meteorologische Zeitschrift*, pages –, 09 2023. doi: 10.1127/metz/2023/1183. URL `http://dx.doi.org/10.1127/metz/2023/1183`.

Medici, D. and Alfredsson, P. H. Measurements on a wind turbine wake: 3D effects and bluff body vortex shedding. *Wind Energy*, 9(3):219–236, 2006. doi: 10.1002/we.156. URL `https://onlinelibrary.wiley.com/doi/abs/10.1002/we.156`.

Menke, R., Vasiljević, N., Hansen, K. S., Hahmann, A. N., and Mann, J. Does the wind turbine wake follow the topography? A multi-lidar study in complex terrain. *Wind Energy Science*, 3(2):681–691, 2018. doi: 10.5194/wes-3-681-2018. URL `https://www.wind-energ-sci.net/3/681/2018/`.

Meyers, J. and Meneveau, C. Optimal turbine spacing in fully developed wind farm boundary layers. *Wind Energy*, 15:305 – 317, 03 2012. doi: 10.1002/we.469.

Moeng, C.-H. and Arakawa, A. Representation of boundary layer moisture transport in cloud-resolving models. *Monthly Weather Review*, 140(11):3682 – 3698, 2012. doi: 10.1175/MWR-D-12-00046.1. URL `https://journals.ametsoc.org/view/journals/mwre/140/11/mwr-d-12-00046.1.xml`.

Muppa, S. K., Behrendt, A., Päth, F., Wulfmeyer, V., Metzendorf, S., and Riede, A. Turbulent humidity fluctuations in the convective boundary layer: Case studies using water vapour differential absorption lidar measurements. *Boundary-Layer Meteorology*, 158:43–66, 01 2016. doi: 10.1007/s10546-015-0078-9.

Muschinski, A., Frehich, R., Jensen, M., Hugo, R., Hoff, A., Eaton, F., and Balsley, B. Fine-scale measurements of turbulence in the lower troposphere: An intercomparison between a kite- and balloon-borne, and a helicopter-borne measurement system. *Boundary-Layer Meteorology*, 98(2):219–250, Feb 2001. ISSN 1573-1472. doi: 10.1023/A:1026520618624. URL `https://doi.org/10.1023/A:1026520618624`.

Niayifar, A. and Porté-Agel, F. Analytical modeling of wind farms: A new approach for power prediction. *Energies*, 9(9), 2016. ISSN 1996-1073. doi: 10.3390/en9090741. URL `https://www.mdpi.com/1996-1073/9/9/741`.

Platis, A., Moene, A. F., Villagrasa, D. M., Beyrich, F., Tupman, D., and Bange, J. Observations of the temperature and humidity structure parameter over heterogeneous terrain by airborne measurements during the LITFASS-2003 campaign. *Boundary-Layer Meteorology*, 165(3): 447–473, 2017. doi: https://doi.org/10.1007/s10546-017-0290-x.

Platis, A., Siedersleben, S. K., Bange, J., Lampert, A., Bärfuss, K., Hankers, R., Canadillas, B., Foreman, R., Schulz-Stellenfleth, J., Djath, B., Neumann, T., and Emeis, S. First in situ evidence of wakes in the far field behind offshore wind farms. *Scientific Reports*, 8:2163, 2018. doi: 10.1038/s41598-018-20389-y.

Platis, A., Bange, J., Bärfuss, K., Canadillas, B., Hundhausen, M., Djath, B., Lampert, A., Schulz-Stellenfleth, J., Siedersleben, S., Neumann, T., and Emeis, S. Long-range modifications of the wind field by offshore wind parks – results of the project WIPAFF. *Meteorologische Zeitschrift*, 01 2020a. doi: 10.1127/metz/2020/1023.

Platis, A., Hundhausen, M., Mauz, M., Siedersleben, S., Lampert, A., Bärfuss, K., Djath, B., Schulz-Stellenfleth, J., Canadillas, B., Neumann, T., Emeis, S., and Bange, J. Evaluation of a simple analytical model for offshore wind farm wake recovery by in situ data and weather research and forecasting simulations. *Wind Energy*, 2020b. doi: 10.1002/we.2568. URL `https://onlinelibrary.wiley.com/doi/abs/10.1002/we.2568`.

Prandtl, L. Über Flüssigkeitsbewegung bei sehr kleiner Reibung. *Verhandlungen des III. Intern. Math. Kongr. Heidelberg*, 1904. Auch: Gesammelte Abhandlungen 2, 484-491.

Rautenberg, A., Schön, M., zum Berge, K., Mauz, M., Manz, P., Platis, A., van Kesteren, B., Suomi, I., Kral, S. T., and Bange, J. The multi-purpose airborne sensor carrier MASC-3 for wind and turbulence measurements in the atmospheric boundary layer. *Sensors*, 19(10), 2019. ISSN 1424-8220. doi: 10.3390/s19102292. URL `http://www.mdpi.com/1424-8220/19/10/2292`.

Sedaghatizadeh, N., Arjomandi, M., Kelso, R., Cazzolato, B., and Ghayesh, M. H. Modelling of wind turbine wake using large eddy simulation. *Renewable Energy*, 115:1166–1176, 2018. ISSN 0960-1481. doi: https://doi.org/10.1016/j.renene.2017.09.017. URL `https://www.sciencedirect.com/science/article/pii/S0960148117308790`.

Siedersleben, S. K., Platis, A., Lundquist, J. K., Lampert, A., Bärfuss, K., Cañadillas, B., Djath, B., Schulz-Stellenfleth, J., Bange, J., Neumann, T., and Emeis, S. Evaluation of a wind farm parametrization for mesoscale atmospheric flow models with aircraft measurements. *Meteorologische Zeitschrift*, 27(5):401–415, 12 2018. doi: 10.1127/metz/2018/0900.

Sørensen, J. N., Mikkelsen, R., Sarmast, S., Ivanell, S., and Henningson, D. Determination of wind turbine near-wake length based on stability analysis. *Journal of Physics: Conference Series*, 524(1):012155, 2014. URL `http://stacks.iop.org/1742-6596/524/i=1/a=012155`.

Stull, R. *Meteorology for Scientists and Engineers*. Brooks/Cole, 10 Davis Drive, Belmond CA, USA, 2nd edition, 2000. ISBN 0534372147.

Tomaszewski, J. and Lundquist, J. Simulated wind farm wake sensitivity to configuration choices in the weather research and forecasting model version 3.8.1. *Geoscientific Model Development*, 13:2645–2662, 06 2020. doi: 10.5194/gmd-13-2645-2020.

van den Kroonenberg, A. C., Martin, S., Beyrich, F., and Bange, J. Spatially-averaged temperature structure parameter over a heterogeneous surface measured by an unmanned aerial vehicle. *Boundary-Layer Meteorology*, 142:55–77, 2012. URL `https://doi.org/10.1007/s10546-011-9662-9`.

Vermeer, N.-J. Local circulation on rotating wind turbine blades from velocity measurements in the wake of a model rotor. pages 117–121, Nottingham, 03 1992. British Wind Energy Association Annual Wind Energy Conference 1992.

Vermeer, N.-J., Sørensen, J., and Crespo, A. Wind turbine wake aerodynamics. *Progress in Aerospace Sciences - PROG AEROSP SCI*, 39:467–510, 10 2003. doi: 10.1016/S0376-0421(03)00078-2.

Wang, C., Campagnolo, F., Canet, H., Barreiro, D. J., and Bottasso, C. L. How realistic are the wakes of scaled wind turbine models? *Wind Energy Science Discussions*, 2020:1–27, 2020. doi: 10.5194/wes-2020-115. URL `https://wes.copernicus.org/preprints/wes-2020-115/`.

Wang, Z. Y., Plate, E. J., Rau, M., and Keiser, R. Scale effects in wind tunnel modelling. *Journal of Wind Engineering and Industrial Aerodynamics*, 61(2):113 – 130, 1996. ISSN 0167-6105. doi: https://doi.org/10.1016/0167-6105(96)00049-9. URL `http://www.sciencedirect.com/science/article/pii/0167610596000499`.

Ward, H. C., Evans, J. G., Grimmond, C. S. B., and Bradford, J. Infrared and millimetre-wave scintillometry in the suburban environment - part 1: Structure parameters. *Atmospheric Measurement Techniques*, 8(3):1385–1405, 2015. doi: https://doi.org/10.5194/amt-8-1385-2015.

Wildmann, N., Mauz, M., and Bange, J. Two fast temperature sensors for probing of the atmospheric boundary layer using small remotely piloted aircraft (RPA). *Atmospheric Measurement Techniques*, 6(8):2101–2113, 2013. doi: 10.5194/amt-6-2101-2013. URL `https://www.atmos-meas-tech.net/6/2101/2013/`.

Wildmann, N., Hofsäß, M., Weimer, F., Joos, A., and Bange, J. MASC; a small Remotely Piloted Aircraft (RPA) for wind energy research. *Advances in Science and Research*, 11:55–61, 2014a. doi: 10.5194/asr-11-55-2014. URL `http://www.adv-sci-res.net/11/55/2014/`.

Wildmann, N., Kaufmann, F., and Bange, J. An inverse-modelling approach for frequency response correction of capacitive humidity sensors in ABL research with small remotely piloted aircraft (RPA). *Atmospheric Measurement Techniques*, 7(9):3059–3069, 2014b. doi: 10.5194/amt-7-3059-2014. URL `https://www.atmos-meas-tech.net/7/3059/2014/`.

Wildmann, N., Ravi, S., and Bange, J. Towards higher accuracy and better frequency response with standard multi-hole probes in turbulence measurement with remotely piloted aircraft (RPA). *Atmospheric Measurement Techniques*, 7(4):1027–1041, 2014c. doi: 10.5194/amt-7-1027-2014. URL `http://www.atmos-meas-tech.net/7/1027/2014/`.

Wildmann, N., Vasiljevic, N., and Gerz, T. Wind turbine wake measurements with automatically adjusting scanning trajectories in a multi-doppler lidar setup. *Atmospheric Measurement Techniques*, 11(6):3801–3814, 2018. doi: 10.5194/amt-11-3801-2018. URL `https://www.atmos-meas-tech.net/11/3801/2018/`.

Wildmann, N., Päschke, E., Roiger, A., and Mallaun, C. Towards improved turbulence estimation with doppler wind lidar VAD scans. *Atmospheric Measurement Techniques Discussions*, 2020:1–30, 2020. doi: 10.5194/amt-2020-8. URL `https://www.atmos-meas-tech-discuss.net/amt-2020-8/`.

Yang, X., Kang, S., and Sotiropoulos, F. Computational study and modeling of turbine spacing effects in infinite aligned wind farms. *Physics of Fluids*, 24(11):115107, 2012. doi: 10.1063/1.4767727. URL `https://doi.org/10.1063/1.4767727`.

Zhang, W., Markfort, C. D., and Porté-Agel, F. Near-wake flow structure downwind of a wind turbine in a turbulent boundary layer. *Experiments in Fluids*, 52(5):1219–1235, May 2012. ISSN 1432-1114. doi: 10.1007/s00348-011-1250-8.

Zhong, X., Sahu, D. K., and Kleissl, J. WRF inversion base height ensembles for simulating marine boundary layer stratocumulus. *Solar Energy*, 146:50 – 64, 2017. ISSN 0038-092X. doi: https://doi.org/10.1016/j.solener.2017.02.021. URL `http://www.sciencedirect.com/science/article/pii/S0038092X17301147`.

zum Berge, K., Schoen, M., Mauz, M., Platis, A., van Kesteren, B., Leukauf, D., El Bahlouli, A., Letzgus, P., Knaus, H., and Bange, J. A two-day case study: Comparison of turbulence data from an unmanned aircraft system with a model chain for complex terrain. *Boundary-Layer Meteorology*, 180:53–78, 2021. ISSN 0306-2619. doi: 10.1007/s10546-021-00608-2.

Appendix A

Publications

A.1 First identification and quantification of detached-tip vortices behind a wind energy converter using fixed-wing unmanned aircraft system

Wind Energ. Sci., 4, 451–463, 2019
https://doi.org/10.5194/wes-4-451-2019

First identification and quantification of detached-tip vortices behind a wind energy converter using fixed-wing unmanned aircraft system

Moritz Mauz[1], **Alexander Rautenberg**[1], **Andreas Platis**[1], **Marion Cormier**[2], **and Jens Bange**[1]

[1]Centre for Applied Geoscience, Eberhard Karls University of Tübingen, 72074 Tübingen, Germany
[2]Institute of Aerodynamics and Gas Dynamics, University of Stuttgart, 70569 Stuttgart, Germany

Correspondence: Moritz Mauz (moritz.mauz@uni-tuebingen.de)

Received: 14 February 2019 – Discussion started: 1 March 2019
Revised: 24 July 2019 – Accepted: 31 July 2019 – Published: 29 August 2019

Abstract. In the present study, blade-tip vortices have been experimentally identified in the wake of a commercial wind turbine using the Multi-purpose Airborne Sensor Carrier Mark 3 (MASC Mk 3) unmanned aircraft system (UAS) of the University of Tübingen. By evaluation of the wind components, detached blade-tip vortices were identified in the time series. From these measurements, the circulation and core radius of a pair of detached blade-tip vortices is calculated using the Burnham–Hallock (BH) wake vortex model. The presented data were captured under a dominating marine stratification about 2km from the North Sea coastline with northern wind direction. The measured vortices are also compared to the analytical solution of the BH model for two vortices spinning in opposite directions. The model has its origin in aviation, where it describes two aircraft wake vortices spinning in opposite directions.

An evaluation method is presented to measure detached-tip vortices with a fixed-wing UAS. The BH model will be used to describe wake vortex properties behind a wind energy converter (WEC). The circulation and core radius of detached blade-tip vortices will be calculated. Also a proposition of the model for WEC wake evaluations will be made to describe two independent co-rotating vortices. Quantifying blade-tip vortices helps to understand the process of vortices detaching from a rotor blade of a wind turbine, their development in the wake until finally dissipating in the far wake and contributing to overall atmospheric turbulence. This is especially interesting for set-ups of numerical simulations when setting the spatial resolution of the simulation grid.

1 Introduction

The wind energy sector has been growing worldwide for decades and the produced power from wind energy is still growing. Not only the amount of installed wind energy converters (WECs) is increasing but also the capacity of a single turbine. Also the field of application has widely increased with WEC. There are systems available for homogeneous terrain, off or near the shore, or even complex terrain with a high amount of additional turbulence stress that is induced onto the wind turbine's blades.

A modern off-shore WEC delivers up to 12 MW of power in ideal conditions. In wind energy research, numerical simulations of the wind velocity field of a WEC and its produced turbulence are important tools that give valuable information. Pressure and velocity distributions around a turbine blade and nacelle as well as in the wake can be studied. A numerical model increases its validity when it is backed by real-world in situ data. Once measured data have revealed some possible tweaks and enhancements to a model, improvements can be made and flow back into the (e.g. numerical) model. Numerical simulation might underestimate peak vorticity and radii of wake vortices, especially when the grid size of the simulation is not sufficient (Kim et al., 2016). Another way of studying WEC wakes are wind tunnel experiments that try to recreate wake patterns in a smaller scale (e.g. Bartl et al., 2012, or Vermeer, 1992). While in the early days of wind tunnel experiments the wake was visualised by smoke trails, PIV (particle image velocimetry) measurements have increased the resolution and accuracy of wind tunnel experiments drastically (e.g. resolving Reynolds shear stress and turbulent kinetic energy; Zhang et al., 2012). But a common issue with wind tunnel measurements is that they usually suffer from scaling problems (Wang et al., 1996). Remote sensing techniques like lidar have also found their way into WEC wake evaluations. Various measurement strategies were developed to visualise WEC wakes, e.g. in complex terrain (Barthelmie et al., 2018). Typical lidar scans provide a long-term measurement of a probed volume or plane. The spatial resolution (25–50 m), however, is comparably coarse. Lidars can provide a continuous monitoring of WEC wake structures (e.g. wake centre, direction and wind velocity deficit) (Bodini et al., 2017) in homogeneous or even in complex terrain (Wildmann et al., 2018). Short-range continuous-wave lidars provide even higher spatial resolution for short focal distances and have been applied in WEC wake measurements (Menke et al., 2018), yet these measurements can still not resolve blade-tip vortices. UAS (unmanned aircraft system) measurements can provide in situ line measurements, covering a small volume but with a high temporal and spatial resolution in (deca-) centimetre range. The coverage of these scales is important to measure detached-tip vortices in the near wake of a WEC.

A WEC, especially in a stable marine ABL (atmospheric boundary layer), acts as a turbulence generator. The added turbulence has two main sources. On the one hand, there is the increased wind shear in the wake that results from the wind deficit in the near wake and the low-pressure bulb that develops behind the WEC nacelle. On the other hand, turbulence is created by expansion and dissipation of detached blade-tip vortices that transfer their kinetic energy to the surrounding flow. A proper understanding of these vortices and their induced load onto the converter blade is of great importance for future enhancement of life span and working loads of wind energy converters in wind farms. Blade-tip vortices follow a helical pattern into the wake, detaching from each converter blade. These detached eddies can be measured with the mounted five-hole-probe on the MASC UAS. Subramanian et al. (2015) detected tip vortices via pressure fluctuations qualitatively in a flight pattern along the wake, also using a small UAS. In this study, an evaluation method is presented to measure the core radius r_c, circulation Γ and maximum tangential velocity $V_{t,\max}$ of a tip vortex using in situ wind measurements from UAS flights perpendicular to the mean wind velocity.

2 Measurement system and measurement site

2.1 Research aircraft

The research UAS MASC Mk 3 (see Fig. 1 and Table 1) is a fixed-wing airborne measurement system of the University of Tübingen that has been used in several measurement campaigns and has been described by Wildmann et al. (2014a, b). The third iteration of this platform features some changes to the fuselage. The electrical pusher motor has been moved from a centre position behind the wings to the tail, accelerating the aircraft along the centre axis and increasing flight stability. The MASC Mk 3 system allows in situ high-frequency measurements of the atmospheric flow and its transported properties. A detailed description of the improved UAS and its instruments can be found in Rautenberg et al. (2019b). The latest iteration MASC Mk 3 is using an improved IMU (inertial measurement unit) and positioning system.

Figure 1. Research UAS MASC Mk 3 shortly before lift-off. (Photo taken by the author.)

Table 1. Characteristics of the MASC Mk 3 UAS at the HeliOW campaign.

Wingspan	4 m
Total weight	≈ 7 kg
Sci. payload	≈ 1 kg
Cruising speed	$19\,\mathrm{m\,s^{-1}}$
Endurance	Up to 2.5 h
Propulsion	Electrical pusher engine
Take-off	Bungee or winch

Aside the changes in fuselage design, the former Research Onboard Computer System (ROCS) autopilot operating on the MASC Mk 2 system has been changed to the Pixhawk 2.1 autopilot. This is an independent open-hardware and open-source autopilot project (Pixhawk-Organisation, 2019).

2.2 Measurement site

Figure 3 shows the location of the measurement site in the north-west of Germany and the flight tracks of the MASC Mk 3 unmanned aerial vehicle (UAV) around the Enercon E-112 converter. Both tracks are part of a rectangular flight pattern around the WEC in an anti-clockwise direction. For the wake data evaluation, only the data captured along the southern flight tracks (orange path in Fig. 3) are used. The E-112 WEC is the most powerful converter in the Jade Wind Park north of Wilhelmshaven, Germany. The particular converter is a former near-shore prototype with a rotor diameter D of 114 m delivering up to 4.5 MW of electrical power and

Figure 2. Research UAS MASC Mk 3 in front of an Enercon wind energy converter at the Jade Wind Park in July 2018. (Photo taken by the author.)

thus comparable to an actual off-shore WEC. The Jade Wind Park is located about 2 km from the North Sea coastline and a maritime influence in the wind profile can be expected.

Apart from surrounding WECs (to the south of the E-112 WEC) power lines to the east and north and industrial buildings to the north and north-east (not in the picture) restricted the flight path to the ones depicted in Fig. 3.

For this study of the near wake of a WEC, the wind turbine described above has been chosen. This specific converter and its location near the coast is comparable with off-shore converters in marine flow which was a requirement when choosing the WEC. The measurements are part of the HeliOW project, in which the atmospheric turbulence in front of and in the wake of a WEC is the foundation of a chain of numerical simulations. The goal of the project is also to determine safe helicopter flight paths in off-shore wind energy parks. The numerical simulation chain also includes CFD simulations of the wind turbine (University of Stuttgart) which are injected in flight-mechanical simulations of a helicopter (provided by Technical University of Munich and DLR Braunschweig). Thus, the tip vortex measurements are an important contribution to the validation of later numerical simulations of the flow.

2.3 Available data

For the tip vortex evaluation, five flight legs (straight and level fly-by instances) are available 0.25 D downstream of the WEC rotor plane. Only one of these legs shows the necessary criterion for the circulation and core radius calculation (see the following sections). The one leg (two vortex measurements) that fits the criterion will be shown exemplary to present the evaluation method and the analytical solution using the BH model approach, including also the approach by Sørensen et al. (2014). At the remaining measurements, it often occurred that the measurement range of the pressure transducer, connected to the five-hole probe, was overstepped by the pressure differences created by the blade-tip vortex. These measurements could not be used for evaluation due to the absence of data at the vortex measurement.

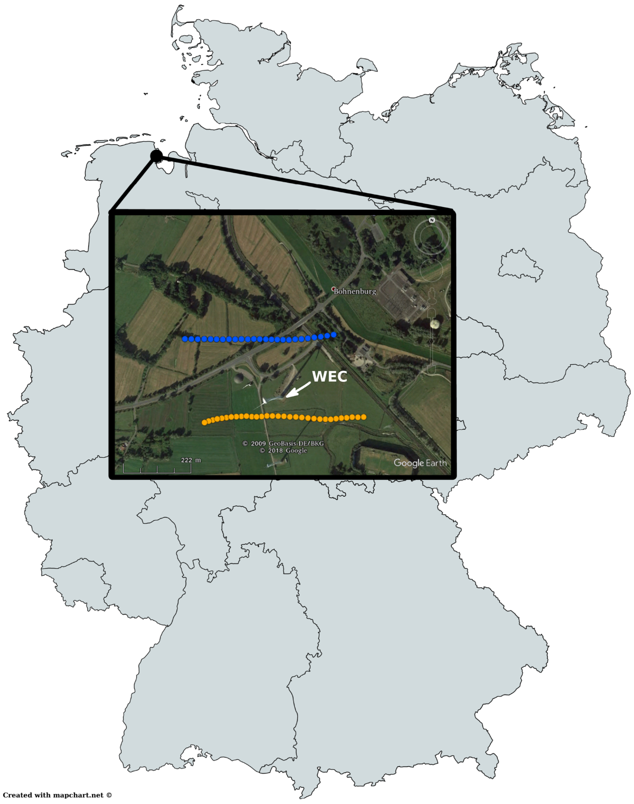

Figure 3. Location of the E-112 WEC in the north-west of Germany north of Wilhelmshaven near the North Sea coast. MASC flight tracks in front (blue) and in the wake (orange) of the E-112 with northern main wind direction (5° north that day). On the © Google Earth image, the WEC is oriented toward the south-easterly wind direction. The map was created with https://mapchart.net (last access: 1 July 2019).

The presented data were captured within a 15 min lasting flight pattern at about 18:30 LT (UTC+2) on a summer day. It can be expected that atmospheric conditions (wind direction and speed, thermal stratification, turbulence intensity) did not change significantly during this period. The average wind speed in the inflow was 8.8 $\mathrm{m\,s^{-1}}$ from the northerly direction (5°) with a turbulence kinetic energy (TKE) of $\approx 0.1\,\mathrm{m^2\,s^{-2}}$ at hub height. These values have been calculated from a 10 s measurement ($\approx$ 200 m flight distance) in the undisturbed atmosphere.

3 Methods

With the goal to measure detached-tip vortices behind a WEC, it is helpful to have at first an understanding of the behaviour of those vortices. Figure 4 shows the helical vortex pattern forming behind a WEC by representing the isosurfaces of the λ_2 criterion of detached-tip vortices from compu-

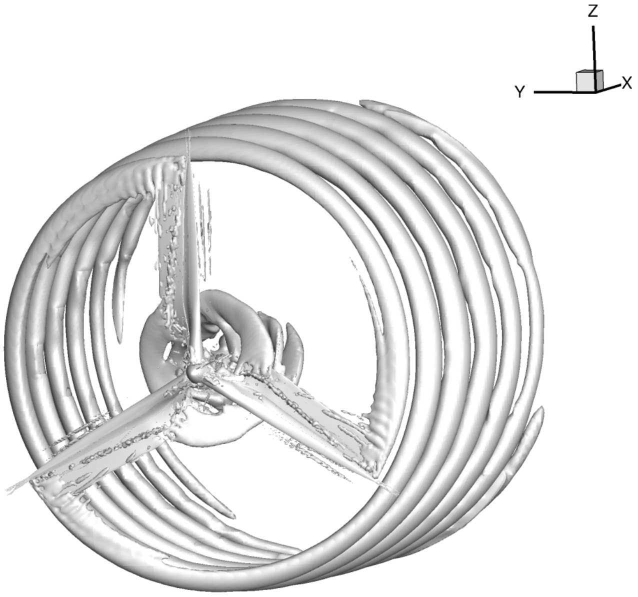

Figure 4. Isosurfaces of detached blade-tip and root vortices following the λ_2 criterion for vortex identification. Here, the x axis follows the main wind direction. Numerical simulation of a generic model of an E-112 4.5 MW converter.

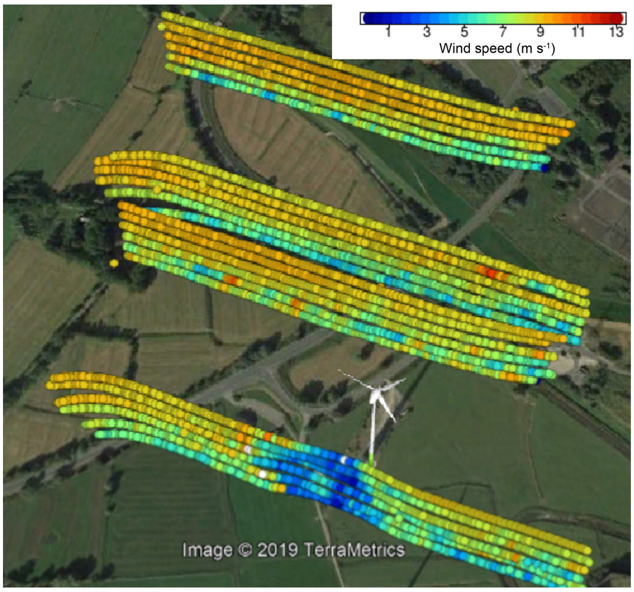

Figure 5. Visualisation of the horizontal wind measurements at different flight leg altitudes (from 85 to 185 m above ground in 20 m steps) and different distances to the WEC (1, −1, −2 and −4 D). Significant wind deficit 1 D behind the WEC E-112. On this day, the wind direction was about 30° north. Image generated in © Google Earth.

tational fluid dynamics (CFD) simulation. The fully resolved unsteady Reynolds-averaged Navier–Stokes (URANS) simulation has been performed by the University of Stuttgart with the compressible flow solver FLOWer (Kroll and Fassbender, 2005), using the Menter SST (Menter, 1994) turbulence model. The modelled rotor is a stand-alone generic model of the Enercon E-112 WEC rotor, based on free-access airfoil data. For more details regarding the numerical methods, please refer to Cormier et al. (2018) in which the same methods have been applied and described. Figures 5 and 6 give a qualitative impression of the presence of the WEC wake. In both horizontal wind velocity and TKE, the wake and its effects are visible. Further downstream the helical pattern will start to meander and the symmetrical pattern will dissipate into turbulence. In the near vicinity of the WEC nacelle, these vortices follow a helical pattern. The helical structure is shown simplified by a ring vortex in Fig. 7 which is an approximation of the wake vorticity at high tip-speed ratio. The tangential velocity in this sketch can be split in its horizontal components at hub height (nacelle height). Here, the y axis points north (ideally anti-parallel to the main wind direction), similar to the conditions at the HeliOW campaign (see Fig. 3), and the x axis points east along the UAS flight path. Note that, at hub height, the tip vortex ideally has no w component (Fig. 7) under the vortex ring assumption. Thus, at this height, the tangential velocity can be split into its horizontal components u and v. The red rectangle indicates a change of perspective, showing a top view of a vortex spinning in the $x-y$ plane. In reality, from planing flight paths until take-off of the UAS and the actual measurement, the wind direction changes slightly. Therefore, for later evaluations, the coordinate system has been rotated into the main wind direction.

3.1 Vortex model

To measure and evaluate tip vortices from UAS data, an analytical vortex model has to be found. Previous efforts to define a vortex were reviewed, e.g. by Jeong and Hussain (1995), comparing several definitions with data from direct numerical simulations and exact solutions of the Navier–Stokes equations. A universal definition of a vortex or a generally applicable model does not exist. Assuming incompressible flow and an irrotational velocity field, where the curl of the gradient of the velocity is zero, the circulation Γ, representing the strength of a vortex around a contour C, can be connected to the vorticity flux by Stokes' theorem. For any surface S that spans the curve C and $\mathrm{d}\boldsymbol{I}$ being an infinitesimal tangential element along C,

$$\Gamma = \oint_C \boldsymbol{V}_\mathbf{t} \cdot \mathrm{d}\boldsymbol{I} = \int_S \boldsymbol{\omega} \cdot \boldsymbol{n} \, \mathrm{d}S. \qquad (1)$$

The circulation Γ is the line integral of the tangential velocity along the curve C which is equal to the vorticity flux $\omega = \nabla \times V_\mathrm{t}$ through the surface S, with $\boldsymbol{n}$ being the normal vector of the surface.

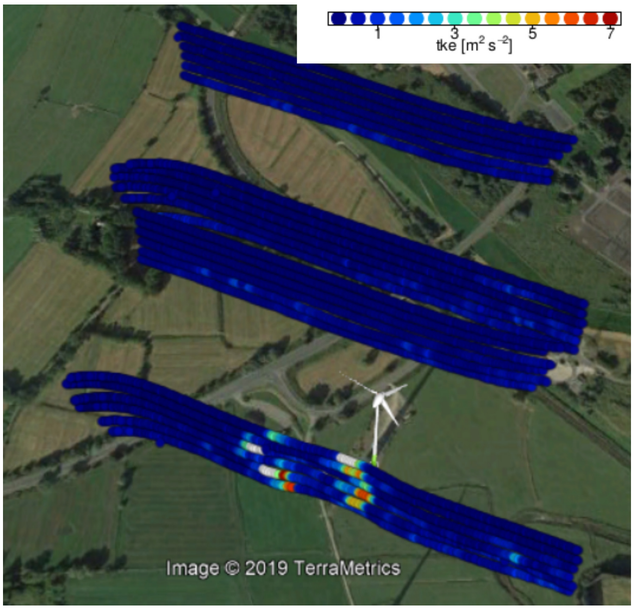

Figure 6. Visualisation of the TKE from the same measurements as in Fig. 5. Blue areas represent low turbulence and red the highest measured turbulence. At 1 D, the presence of the wake and the produced turbulence by the tip vortices is visible. The averaging window for the for TKE calculation is 1 s, corresponding to 100 data points, and suits qualitative reading only. Image generated in © Google Earth.

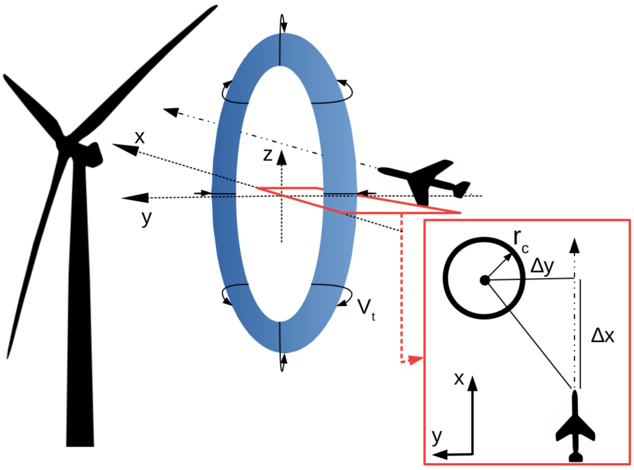

Figure 7. Simplified sketch of a vortex pair passed by the UAS to the right. In reality, it would have rather a helical pattern than a ring shape. Velocities and axis are according to meteorological standards; therefore, axis and orientation are according to the in situ conditions. The y axis points north; x axis points east. At hub height, the w component (along z axis) vanishes. The red rectangle illustrates a top view of a tip vortex with distance Δy to the UAS.

A circular integration in a cylindrical polar coordinate system with the azimuthal angle ϕ and the radius r yields

$$\Gamma(r) = \int_0^{2\pi}\int_0^{r} \omega(r,\phi) r \mathrm{d}r \, \mathrm{d}\phi. \tag{2}$$

For a two-dimensional axisymmetric vortex, the circulation

$$\Gamma(r) = 2\pi r V_\mathrm{t}(r) \tag{3}$$

is a simple function of the radius and the tangential velocity V_t. Since real vortices in fluids experience viscous effects, the structure of detached-tip vortices of the blade of WEC cannot be sufficiently described by Eq. (3). Close to the centre of the vortex, lower tangential velocities persist, increasing to their maximum at the core radius r_c of the vortex and decreasing again for further distances r. To account for that, in the context of WEC and also for detached-tip vortices from the wings of aircraft, an analytical model is necessary.

Since in this study detached vortices of a WEC converter are treated similarly to aircraft wake vortices, a few similar model approaches were possible. A comparison of analytical vortex models for tip vortices created by aircraft has been done by Ahmad et al. (2014). Also Fischenberg (2011) measured wake vortices created by the VFW 614 ATTAS manned aircraft (DLR Braunschweig) and compared the results to two similar vortex models proposed by Lamb (1939) and Burnham and Hallock (1982). Fischenberg concludes that both models show the ageing processes of a vortex wake known from theory. In general, the model by Burnham–Hallock shows a slightly better agreement in circulation and tangential velocity to the conducted measurements by Fischenberg. Also Vermeer (1992) uses the BH vortex model successfully to describe WEC wake vortices. According to these findings and its simplicity, it has been decided to use the analytical solution for wake vortices by Burnham–Hallock in this study. While the two counter-rotating vortices in the BH model used in aviation interact with each other, the two opposite vortices in a WEC wake do not do that. This is an important detail to point out. So for the identification of the vortex parameters (Γ, r_c), a model of two counter-spinning vortices is not necessary. Here, a stand-alone vortex is considered. For the later analytical solution of the whole flight path perpendicular to the WEC wake, the BH model for two vortices is consulted.

The BH model does not provide a solution for the whole wake structure but for an idealised 2-D cut. Describing two (independent) counter-rotating wake vortices with a simple analytical model and comparing it to in situ measurements is a new approach in studying wind turbine wake structures.

Having a look at the BH model, a vortex is described by its circulation Γ, tangential velocity V_t and its core radius r_c. The tangential velocity is the velocity of the air circling the vortex centre and is a function of the distance r to the vortex core.

$$V_\mathrm{t}(r) = \frac{\Gamma}{2\pi}\frac{r}{r_\mathrm{c}^2 + r^2} \tag{4}$$

The core radius r_c is defined as the distance from the vortex centre (or core) at which the tangential velocity is at its maximum (circular symmetry). So the radius r_c is also the radius

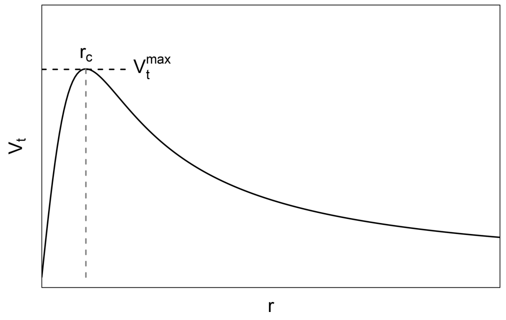

Figure 8. Qualitative plot of the tangential velocity from the vortex core outwards. The tangential velocity increases from zero (left) to a maximum at a distance r_c and decreases to zero for large distances (to the right).

at which the surface integral (see Eq. 1) is maximal, considering a circular surface. For $r = r_c$, the maximum tangential velocity becomes (Eq. 5)

$$V_{t,max} = \frac{\Gamma}{4\pi r_c}. \tag{5}$$

Figure 8 shows the tangential velocity V_t distribution of a BH-modelled vortex with the highest tangential velocity at the distance $r = r_c$. The distribution is circle symmetric with the vortex core ($r = 0$) in its centre.

In order to estimate the circulation and size of r_c from transects through the vortices with MASC in the wake of a WEC, the following procedure is proposed.

3.2 Evaluation method

As shown above, it is likely to measure tip vortices at hub height. At this height, a simplification of the two vortices can be made. The blade-tip vortices can be considered as two-dimensional vortices of circular shape in the horizontal plane, and ideally the w component can be neglected. After subtracting the mean wind v_∞, the vortex tangential velocity is

$$\boldsymbol{v} - \boldsymbol{v}_\infty = \boldsymbol{v}' = (u', v', 0). \tag{6}$$

The norm of the tangential velocity then is

$$V_t = \sqrt{u'^2 + v'^2}. \tag{7}$$

When measuring with a UAS, the measurement can be considered a snapshot of the in situ conditions. Figure 9 differentiates between two different scenarios of the UAS passing a vortex. Both are shown from a top view. Both scenarios will be explained in detail in the following paragraphs, with first focussing on Fig. 9a. Here, the UAS passes the vortex at its closest distance (Δy), marked as point 3 in the sketch, with $\Delta y > r_c$; thus, the vortex core radius is not reached.

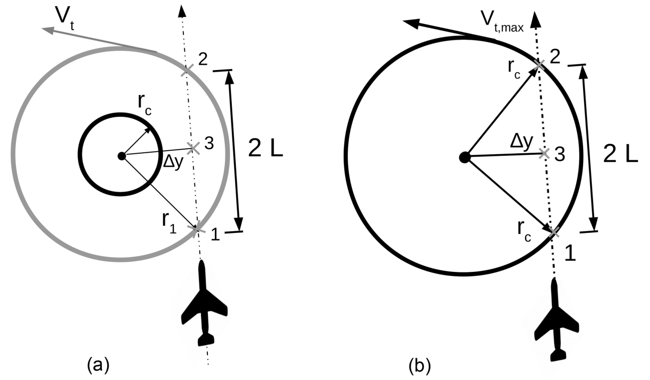

Figure 9. Schematic of the UAS passing a vortex in the horizontal plane (top-down view). Two different cases have to be distinguished: the closest distance to the vortex $\Delta y > r_c$ **(a)** and the passing distance $\Delta y < r_c$ **(b)**.

Points 1 and 2 mark the positions of two corresponding tangential velocities of identical absolute value, when approaching the vortex and moving away from it again. The measured signal is similar to the dashed black line in Fig. 10 that is an example for $\Delta y = 2r_c$. From such data, only point 3 can be identified, since it is the point at which the measured tangential velocity is at its maximum. Points 1 and 2 are somewhere left and right of the maximum, with L being unknown. There are indefinite combinations of Γ and r_c that could describe the vortex using Eq. (4).

$$V_{t,2} = V_{t,1} = \frac{\Gamma}{2\pi} \frac{r_1}{r_c^2 + r_1^2} \tag{8}$$

$$V_{t,\Delta y} = \frac{\Gamma}{2\pi} \frac{\Delta y}{r_c^2 + \Delta y^2} \tag{9}$$

$$r_1^2 = r_2^2 = L^2 + \Delta y^2 \text{ (Pythagorean theorem)} \tag{10}$$

Equations (8), (9) and (10) are known to describe the velocities and geometry of the measurement. $V_{t,1}$ ($V_{t,2}$) is the tangential velocity at the point 1 (and 2). Since there are four unknown parameters (Γ, r_c, L and $r_{1,2}$), the problem is not solvable.

Now, we consider the case when the UAS passes a vortex at $\Delta y < r_c$, as shown in Fig. 9b. The measured tangential velocity now provides a distinct feature: a double peak in the horizontal wind measurement. This double peak is caused by passing the maximum tangential velocity at $r = r_c$ at positions 1 and 2. Since the tangential velocity decreases from that point inwards (towards the vortex core), the velocity at point 3 is a local minimum, leading to a visible "dent" in the data (see red line in Fig. 10). Additionally, the ground speed of the UAS is known; hence, the distance L can be calculated. The three equations previously described above then become

$$V_{t,2} = V_{t,1} = V_{t,max} = \frac{\Gamma}{2\pi} \frac{r_c}{r_c^2 + r_c^2} = \frac{\Gamma}{4\pi r_c} \tag{11}$$

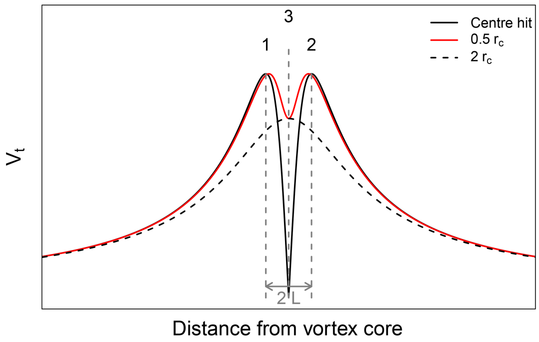

Figure 10. Analytical solution of a UAS passing the vortex at a path crossing the centre (solid black line), passing at $r = 0.5r_c$ (red line) and at a distance double the core radius (dashed black line). The peak-to-peak distance is 2 L (see Fig. 9), illustrated above for the solid black line.

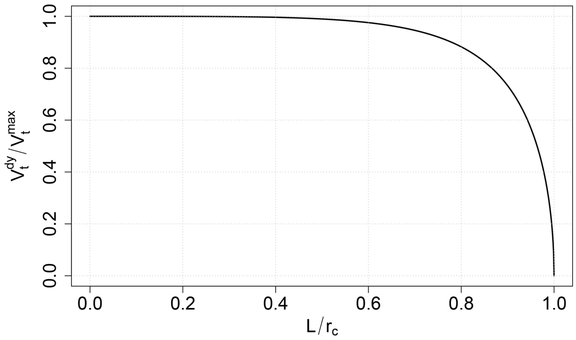

Figure 11. Dimensionless relationship between the ratio of the minimum (dent) tangential velocity and the maximum tangential velocity vs. half the peak-to-peak distance (L) in percentage of r_c.

$$V_{t,\Delta y} = \frac{\Gamma}{2\pi} \frac{\Delta y}{r_c^2 + \Delta y^2} \tag{12}$$

$$r_1^2 = r_2^2 = L^2 + \Delta y^2 = r_c^2 \quad \longleftrightarrow \quad \Delta y^2 = r_c^2 - L^2. \tag{13}$$

With now only three (Γ, r_c and Δy) unknown parameters, it is possible to solve the equations.

Dividing Eq. (12) by Eq. (11) eliminates Γ. Inserting Eq. (13) gives

$$\frac{V_{t,\Delta y}}{V_{t,\max}} = \frac{r_c\sqrt{r_c^2 - L^2}}{r_c^2 - \frac{L^2}{2}}. \tag{14}$$

Equation (14) describes a tangential velocity ratio that is a function of L. Also L is known to range from 0 to r_c. A dimensionless relationship ($L\ r_c^{-1}$) can be plotted and is shown in Fig. 11. By passing the vortex with $\Delta y < r_c$ and plotting the measured V_t against the distance to the vortex (Fig. 10), we can determine L, $V_{t,\max}$, V_t, Δy. Using the diagram in Fig. 11, we finally determine $L\ r_c^{-1}$ and thus r_c.

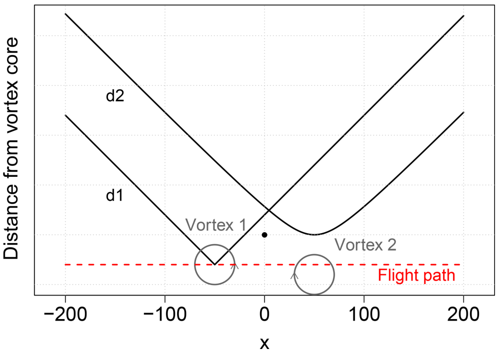

Figure 12. Qualitative example of an ideal flight path (vortex 1) and a passing one with a little offset (vortex 2) of the UAS. For the field measurement, the distances d_1 and d_2 are calculated from the UAS GPS position and the location (offset) of the vortex in relative coordinates, with WEC at $(0, 0)$ indicated with a black dot. The vortex position can be derived from the extent of the tangential velocity V_t measured by the UAS and the peak-to-peak distance, explained in the previous sections. In this example, $d_{1,2} = \sqrt{\Delta x^2 + \Delta y^2}$ with $\Delta y_1 = 0$ for d_1 and $\Delta y_2 = \text{const.} \neq 0$ for d_2.

3.3 Analytical reconstruction

As shown above, blade-tip vortices can be identified by their distinct "dent" feature, when the $\Delta y < r_c$ criterion is met. Basic geometry and the BH model further allow for a reconstruction (analytical solution) of the individually measured vortex, which is helpful to verify the measurements and evaluation technique. With Eqs. (15) and (16), the distance to each vortex core (centre), to and along the UAV flight path, can be calculated (Fischenberg, 2011). In Fig. 12, the distances of the UAS to two vortices spinning in opposite directions are shown. In the figure, vortex 1 is passed through its core and vortex 2 is passed with a slight offset. The flight path of the UAS is indicated with a dashed red line. Those distances are inserted into Eqs. (17) and (18) using the relation of Eq. (4); the tangential velocity along the meteorological x axis (u' component) and y axis (v' component) can be calculated:

$$d_1 = \sqrt{\Delta x^2 + \Delta y^2} = \sqrt{(x - x_{\text{Vortex 1}})^2 + (y - y_{\text{Vortex 1}})^2} \tag{15}$$

$$d_2 = \sqrt{\Delta x^2 + \Delta y^2} = \sqrt{(x - x_{\text{Vortex 2}})^2 + (y - y_{\text{Vortex 2}})^2}. \tag{16}$$

While the y coordinate can be derived from the measurement (using Δy and the UAS position, s.a. Sect. 4.3) the x coordinate of the vortex $x_{\text{Vortex 1,2}}$ is the x coordinate of the flight path at the position "3", e.g. Fig. 9.

$$u' = V_t(d_1)\left(\frac{y - y_{\text{Vortex 1}}}{d_1}\right) - V_t(d_2)\left(\frac{y - y_{\text{Vortex 2}}}{d_2}\right) \tag{17}$$

$$v' = -V_t(d_1)\left(\frac{x - x_{\text{Vortex 1}}}{d_1}\right) + V_t(d_2)\left(\frac{x - x_{\text{Vortex 2}}}{d_2}\right) \tag{18}$$

4 Results

4.1 Vortex measurement

Figure 13a shows the $v_\mathrm{h} = \sqrt{u^2 + v^2}$ component of the wind measurement behind the WEC at hub height. The data reveal several (near)-wake specific features. This flight leg shows two measurements of a tip vortex, indicated by the arrows in Fig. 13a. In between those two peaks, the wake deficit is measurable by a significant drop of the horizontal wind velocity. Due to the near vicinity to the nacelle, the wake deficit is dominated by turbulence created by the blade root vortices. Figure 14 shows a zoomed-in look at the measured vortices depicted in Fig. 13. Figure 14a shows the vortex measured while entering the wake (vortex 1) and 14b while leaving the wake (vortex 2). Both Fig. 14a and b show the plain UAS measurements.

Figure 14c and d show the same measurement but the UAS coordinate system is rotated into the vortex rotational plane. This data rotation is necessary since the UAS travels and measures in the horizontal plane; the vortex rotational plane, however, differs slightly from the horizontal plane. This can be seen in the w component of the plain UAS measurement which is non-zero. To compensate for this fact, for the vortex evaluation, the data are rotated into the vortex rotational plane. This can be understood as the UAS canting into the rotational plane of the vortex to capture the rotational energy in a 2-D plane. Through the (individual) transformation, an error in the residual time series is introduced, but at a distance of $\pm r_\mathrm{c}$ around the vortex core where the evaluation takes place, the data are corrected. Meaning, in Fig. 14c, d, the dashed purple and solid purple lines are overlaid. A good indicator that the data rotation was successful is when the norm of the wind vector (dashed purple line) and the v_h in between the dashed grey lines are about the same magnitude. Then it can be concluded that the two-dimensional vortex rotation (u and v components) includes the entire kinetic energy; i.e. the vertical wind component is now neglectable.

Examining both vortices, the velocity distribution pattern of the UAS passing at distance $r < r_\mathrm{c}$ is visible in the v_h measurement. The horizontal wind velocity v_h is a superposition of the tangential velocity, turbulence and the horizontal wind of the undisturbed inflow. The characteristics of the tangential velocity of vortex 1 (Fig. 14a, c) are almost solely determined by the v component, while in Fig. 14b, d the u component inheres an equal part. In the plain UAS measurement (i.e. before coordinate transformation), vortex 2 has a significant non-zero w component (Fig. 14b), indicating that the vortex did not rotate in the $x - y$ plane. Especially Fig. 14d shows a significant reduction of the w component after the data rotation. Dashed purple lines indicate the velocity deficit $\mathrm{d}V_\mathrm{t}$ (dent); dashed grey lines indicate the peak-to-peak distance. The dot-dashed purple line can be interpreted as an extension of the horizontal wind velocity by the w component, essentially giving the norm of the wind vector:

$$|\boldsymbol{v}| = \sqrt{u^2 + v^2 + w^2}. \tag{19}$$

Table 2 shows the derived parameters from the vortices depicted in Fig. 14. It has to be mentioned that vortex 1 made for a better and clearer measurement, since vortex 2 is influenced by the wind deficit and turbulence inside the wake. Vortex 1 shows a sharp jump in the tangential velocity which makes it easier to obtain the necessary quantities and provides more reliable results. The average of the obtained circulations is $\overline{\Gamma} = 74.17\,\mathrm{m^2\,s^{-1}}$; the average core radius is $\overline{r}_\mathrm{c} = 0.61\,\mathrm{m}$.

Figure 16 shows a two-dimensional cut through a skewed or canted vortex that results in an ellipse where the peak-to-peak distance is $2\ L'$. This peak-to-peak distance is underpredicted ($2\ L' < 2\ L$). The introduced error $\Delta y'$ is visualised in Fig. 16 by dotted red lines. To overcome this issue, the measured data are rotated into the vortex hose if necessary. This simulates the UAS canting to follow the oblique vortex hose.

4.2 Quality control and error estimation

The wake of a WEC, especially as close as 0.25 D behind the nacelle, is a highly turbulent region. When measuring with an autonomous UAS, it is of interest whether the UAS is capable of manoeuvring stably in such an environment and if the measurement instrument (e.g. five-hole probe) is operating within its operational specifications. Figure 15a shows the attitude of the UAS while passing the WEC for the consulted flight leg and the angle of attack, sideslip and true air speed (panel b). The UAS is affected by the wake entry and exit. The motions of the UAS are well recognised by the IMU and auto-pilot (see Fig. 15a) and taken into account for the later post-processing. The UAS handles these motions without loss of control.

Dashed grey lines in Fig. 15b indicate the limit of the calibrated range of ±20° of the five-hole probe. Passing a tip vortex at $\Delta y < r_\mathrm{c}$ is an extreme event, not only for the aircraft but also for the pressure probe. Angle of attack and sideslip are within the calibrated ranges, with one exception of vortex 1. Here, the sideslip is extrapolated. An examination of the true air speed (TAS) for the measurement (blue line in Fig. 15b) clearly shows the entry and exit of the wake. Changes in true air speed cannot be avoided. Usually small deviations from the calibrated TAS value of the five-hole probe do not result in significant changes in the calculated wind speed. The peaks visible in the TAS measurement, however, will have an effect on the wind velocity calculation. The influence of different air speed calibrations on UAS measurements is studied by Rautenberg et al. (2019a). There it is concluded that the deviation from the "true" wind speed is about 10 % or at most $1\,\mathrm{m\,s^{-1}}$, e.g. for a TAS error measured at vortex 2 of about $8\ \mathrm{m\ s^{-1}}$. So the peak velocities may be underestimated by $1\ \mathrm{m\ s^{-1}}$.

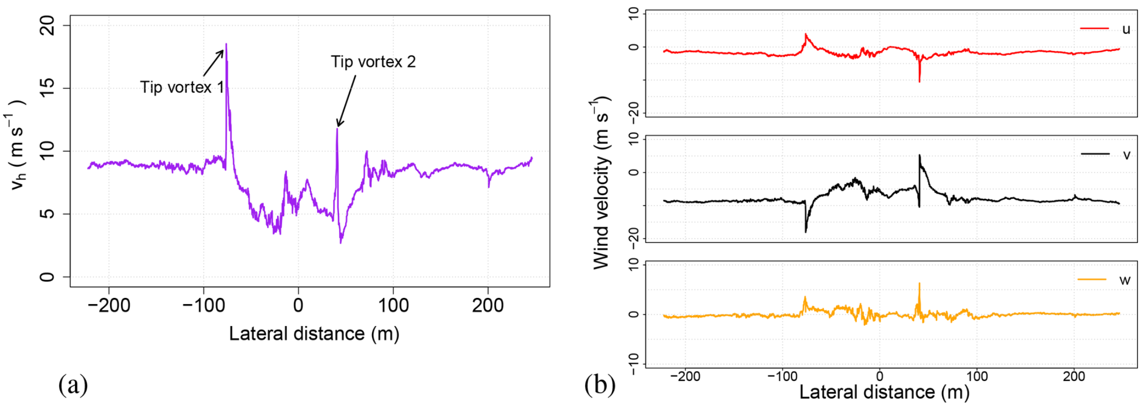

(a) (b)

Figure 13. **(a)** Horizontal wind v_h measurement at hub height in the WEC wake at a distance of 0.25 D to the nacelle. The two tip vortices are indicated by the arrows. **(b)** The same measurement split into the three wind components (u, v, w). The x axis is relative easting with the WEC position as origin (Δx in Fig. 7).

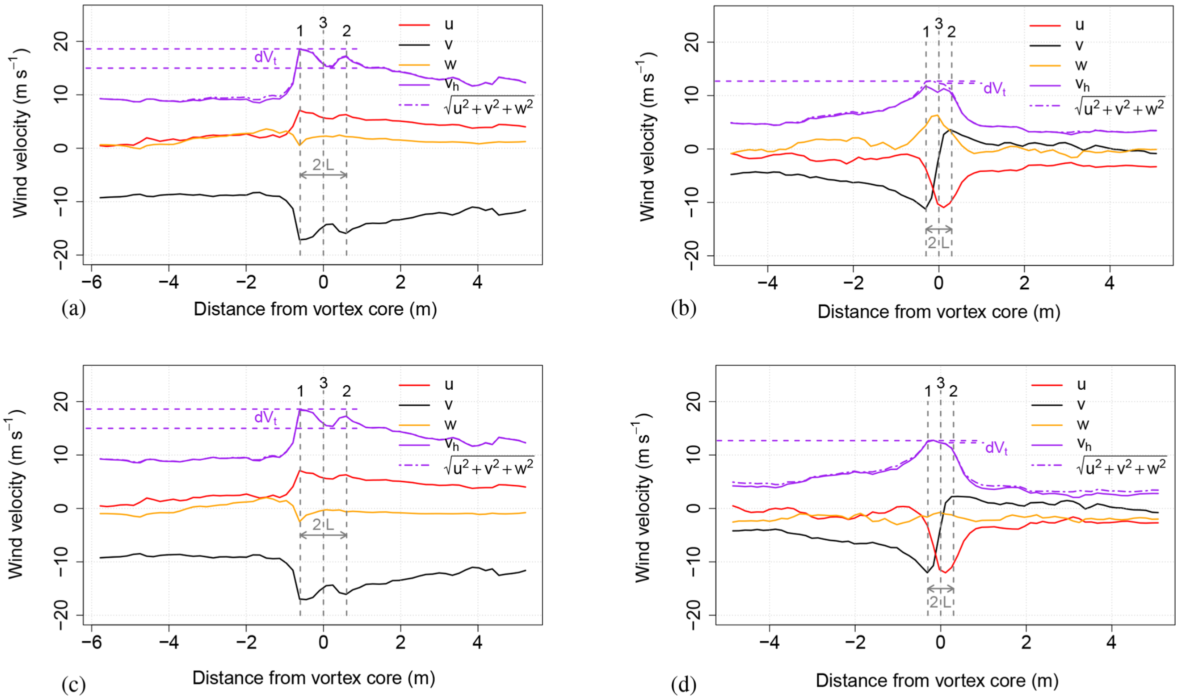

Figure 14. Measured tip vortex 1 and tip vortex 2 from Fig. 13a. Dashed purple lines indicate the velocity deficit (dent), dashed grey lines the peak-to-peak distance. The horizontal wind velocity v_h is a superposition of the tangential velocity and the horizontal wind of the inflow/surroundings. To eliminate the w component, the data have been rotated into the vortex coordinate system. This is necessary to measure the vortex correctly. Panels **(a)** and **(b)** show the plain UAS measurement of the vortices. **(c, d)** The UAS has been rotated into the vortex coordinate system (vortex plane) to capture the whole two-dimensional rotation.

While this error has no significant influence on the $V_{\mathrm{t},\Delta y}/V_{\mathrm{t,max}}$ ratio, it is significant when calculating the circulation Γ from Eq. (5). In the presented case, the circulation of vortex 2 is underpredicted by about 10 %.

4.3 Vortex reconstruction

The BH model provides a solution for two vortices spinning in opposite directions, as, for example, found in an aircraft wake. A similar constellation of vortex pairs can be found in a WEC wake at hub height (see Fig. 7), with their vortex cores positioned along the x axis. This approximation can only be done when the flight path is perpendicular to the wind

Table 2. Determined parameters from vortex measurements.

Vortex	$\mathrm{d}V_\mathrm{t}$ ($\mathrm{m\,s^{-1}}$)	$V_{\mathrm{t,max}}$ ($\mathrm{m\,s^{-1}}$)	$V_{\mathrm{t},\Delta y}$ ($\mathrm{m\,s^{-1}}$)	$V_{\mathrm{t},\Delta y}/V_{\mathrm{t,max}}$ (–)	L (m)	L/r_c (–)	r_c (m)	Γ ($\mathrm{m^2\,s^{-1}}$)
Vortex 1	3.4	9.6	6.2	0.65	0.61	0.93	0.66	81.30
Vortex 2	0.2	9.7	9.5	0.98	0.3	0.55	0.55	67.04

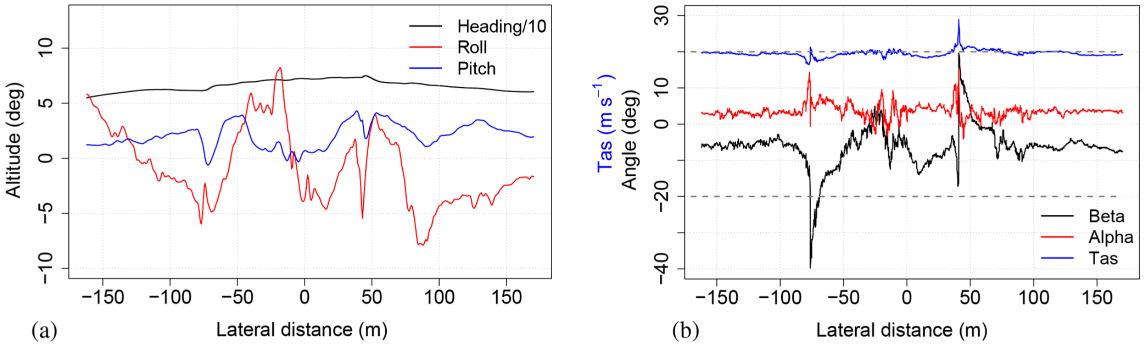

(a) (b)

Figure 15. (a) Attitude angles of the UAS from flight leg taken for the tip vortex evaluation. **(b)** Angle of attack (alpha) and sideslip (beta) at the five-hole probe. Dashed grey lines indicate the calibration range of the five-hole probe. Overstepped angles are extrapolated in post-processing. In blue is the true air speed of the UAS.

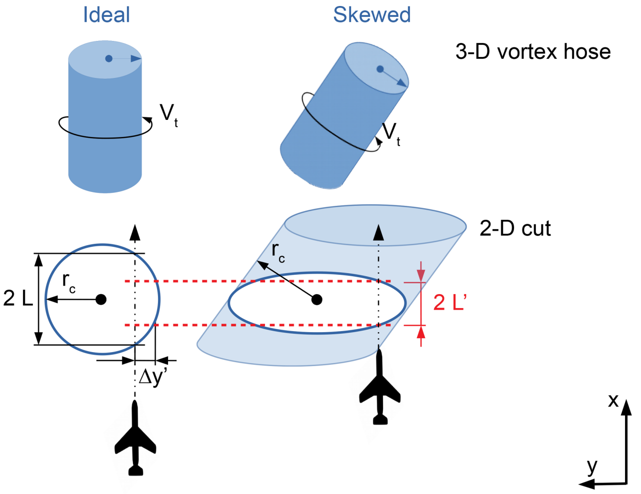

Figure 16. Sketch of an ideal and skewed (exaggerated) vortex hose at hub height. The simplifications in the evaluation method only consider components in the $x-y$ plane, which leads to an underprediction of the real peak-to-peak distance. The fact that the real "r_c" does not lie in the $x-y$ plane leads to an error. A horizontal cut through the vortex has an ellipsoidal geometry instead of a circular one, as in ideal measurement conditions.

(wake) direction to assure that the measured vortices are of the same age.

With the average values $\overline{\Gamma}$ and $\overline{r}_\mathrm{c}$ retrieved from Table 2, the minimum measured tangential velocity between the two peaks (position "3" in Fig. 14) as well as a distance Δy can be derived. The resulting distance to the vortex core Δy can then be fed to a model, based on the BH approach. Figure 17 shows the analytical solution of u' and v' overlain with measured data of u an v. Overlain to the in situ data, the tangential velocity still contains the mean horizontal wind $V_\mathrm{t}=\sqrt{u'^2+v'^2}$. For the analytical solution, the measured data have been rotated slightly (approximately 10°) into the mean wind direction to fit the meteorological coordinate system with the vortex coordinate system, so the u component equals zero on average, and v is the predominant horizontal wind direction. In addition to the solely BH solution for the v' component (dotted line in Fig. 17b), the long dashed line shows the same solution but multiplied with a correction factor to satisfy for the wind deficit in the wake. The general vortex model does not consider the mean horizontal velocity, so it needs to be accounted for, especially when there is a artificially induced drop behind the WEC in the wake (wake deficit). In the present case, the velocity deficit was measured to be about 65 %. It is visible as a jump in the mean horizontal wind between the two measured vortices. Similar deficits were already measured by Wildmann et al. (2014a) or Bartl et al. (2012). The velocity correction function is simply an upside-down Tukey window. The analytical solution remains uncorrected until it enters the wake of the WEC. After incorporating a deficit correction to the analytical solution, it is visible that the deficit in the wake plays an important role in the structure (placement, intensity, etc.) of the vortex, especially since the two vortices do not interact with each other, as the two vortices in the BH model for aircraft wakes do.

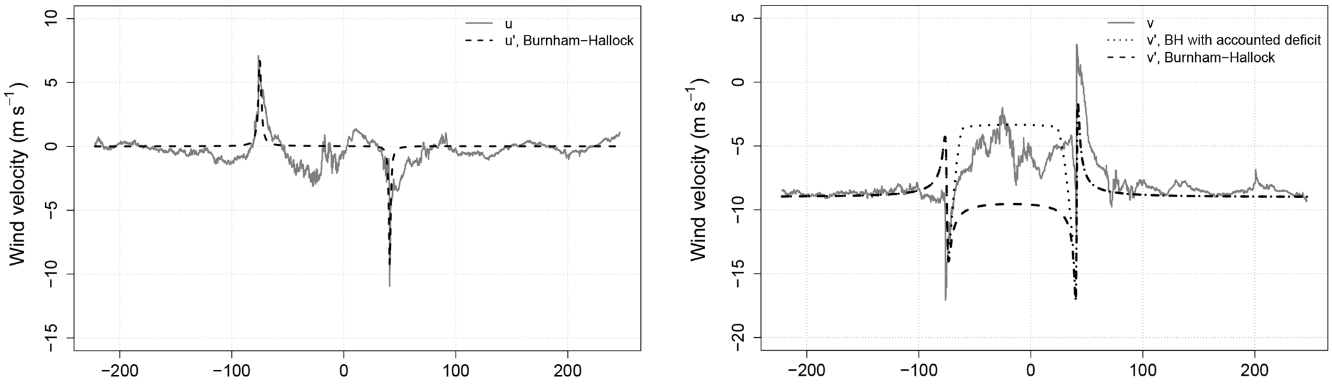

(a) (b)

Figure 17. Analytical solution (dashed lines) for u' and v' of the two vortices from the parameter evaluation. The corresponding wind components (u and v) from Fig. 13b from the UAS measurements are in grey. The long dashed solution in panel **(b)** additionally accounts for the deficit in the wake.

5 Discussion

Here, we compare the airborne measured circulation Γ with data of the WEC itself. Equation (20) allows for a calculation of the blade-tip vortex strength by given parameters and describes the circulation for a rotor of constant thrust coefficient, e.g. (Sørensen et al., 2014):

$$\Gamma = \frac{\pi v_\infty^2 C_\mathrm{T}}{\Omega N_\mathrm{b}} \approx 66.2\,\mathrm{m}^2\,\mathrm{s}, \tag{20}$$

with N_b being the number of blades and Ω the rotational velocity provided by the owner of the WEC. For the determination of the thrust coefficient C_T, the following estimation is done.

The relatively low wind speed ($v_\infty = 8.8\,\mathrm{m\,s^{-1}}$ by UAS measurement) implies a pitch angle of $\beta = 0°$ when approximating the E-112 with the NREL 5 MW offshore WEC (Jonkman et al., 2009).

The tip-speed ratio ($\mathrm{TSR} = \frac{\Omega R}{v_\infty}$) can also be calculated, and thus a thrust coefficient $C_\mathrm{T} \approx 0.8$ can be estimated from the C_T–TSR relationship by Al-Solihat and Nahon (2018).

The calculated value for Γ from WEC-specific and atmospheric parameters is similar to the vortex strength that was extracted from the vortex measurements (average $\overline{\Gamma} = 74.17\,\mathrm{m}^2\,\mathrm{s}^{-1}$). The presented method, to calculate gamma from UAS data using a geometric simplification of the tip vortex and the application of the BH vortex model, provides reasonable results.

The BH vortex model does work for aircraft-induced vortices, as shown by Ahmad et al. (2014) as well as Fischenberg (2011), and as the results imply, it can be used to describe WEC wake vortex properties. Not least, both phenomena can be described by two vortices spinning in opposite directions, yet there is no interaction of the two opposite vortices, as usually intended in the aircraft wake model. Vortex patterns of a WEC wake show higher complexity than aircraft wake vortices. The whole wake is in motion, and different turbulence and shear forces interact with each other. Therefore, for the wake vortices, some simplifications had to be made; e.g. the shown evaluation method is only valid for a 2-D cut of the whole vortex hose. Also the blade root vortex was not analysed any further.

In this study, also the fact that the UAS experiences a change in TAS when entering the wake is addressed. Theoretically, the calibration range of the used five-hole probe is for a fixed air speed which changes when entering the wake. Since this evaluation uses the ratio of two velocities, the influence of a different calibration for the five-hole probe does not lead to a significant error. For the calculation of the circulation Γ, however, absolute velocities are necessary and a small error can be expected due to a change in TAS when entering and leaving the wake velocity deficit. The error is estimated to be ±10 % for the calculated wind velocities (Rautenberg et al., 2019a). An error estimation is given in Sect. 4.2.

6 Conclusions and outlook

The resulting circulation strength Γ derived from UAS data shows good accordance with the results obtained from Eq. (20). It can be concluded that the evaluation method, using the basic geometrical properties of a vortex, can be used to derive vortex properties in a WEC wake. Turbulence acting on the vortex and on the surrounding atmospheric flow can aggravate an evaluation since the evaluation is done mainly graphically. For example, the second tip vortex is embedded in a relatively high level of turbulence (wake deficit, shear, etc.). It also does not show a clear border to the undisturbed atmosphere as tip vortex 1 does. The reference velocity levels for the evaluation are therefore harder to extract from the measurements. Also a hit of a blade-tip vortex in flight changes the TAS locally and temporally, resulting in an error in the velocity measurement (usually 5 %–10 % off).

In addition, this method still has to be proven at larger distances to the WEC nacelle, where the vortices might begin to meander and get unstable. However, to our knowledge, this is the first quantitative analysis of WEC tip vortices using in situ measured turbulence data by a fixed-wing UAS.

The MASC Mk 3 system is capable of measuring detached-tip vortices in the wake of a WEC. The spatial and temporal resolution is sufficient to detect vortex patterns in the measurements. However, on many occurrences, the measured sideslip β left the calibration range of the five-hole probe in a matter that the corresponding pressure transducer was off the measuring range, leaving data lags in the time series. In conclusion, those measurements could not have been used.

For future measurements, the calibration of the (conical) five-hole probes could simply be expanded to larger angles up to ±40° (Fingersh and Robinson, 1998). This then allows for a lower TAS of the UAV, which in turn results in lower pressures at the pressure transducers and a better spacial resolution of the data. The path accuracy of the UAS will be upped by using an RTK (real-time kinematic) GPS. This will allow for precise back-calculations of the positions of the vortices. Wake meandering, wake and vortex widening can then be documented.

The proposed analytical vortex model by Burnham and Hallock is capable of describing WEC wake vortices. Yet, as for most analytical models, the analytical solution shown in this paper can and should be improved, e.g. to better fit the WEC wake (velocity deficit, blade root vortex near the nacelle). This evaluation was conducted with data obtained at 0.25 D from the nacelle. For a future additional field campaign, blade-tip vortices in the further wake shall be investigated.

Data availability. The measurent UAS data can be provided by the authors (Moritz Mauz, Jens Bange, Andreas Platis) by ftp. Due to the amount and complexity of the data, we advise a brief introduction by the authors.

Author contributions. MM and JB developed the theoretical formalism and performed the analytic calculations and the UAS data evaluation. MC performed the numerical simulations and provided insights from a numerical point of view. AR added to the theory, piloted the aircraft and carried out the experiments with MM. All authors provided critical feedback and helped shape the research, analysis and paper.

Competing interests. The authors declare that they have no conflict of interest.

Acknowledgements. We thank Enercon GmbH for cooperation and WRD GmbH for the provision of a generic recreation of the E-112 geometry for the numerical simulations. For extensive technical support in the field campaign, we want to thank Martin Schön and Patrick Manz.

Financial support. This research has been supported by the Projekträger Jülich, the BMWi (Federal Ministry for Economic Affairs and Energy) that funded the HeliOW project (0324121C) and the Deutsche Forschungsgemeinschaft.

This open-access publication was funded
by the University of Tübingen.

Review statement. This paper was edited by Sandrine Aubrun and reviewed by two anonymous referees.

References

Ahmad, N. N., Proctor, F. H., Duparcmeur, F. M. L., and Jacob, D.: Review of Idealized Aircraft Wake Vortex Models, 52nd AIAA Aerospace Sciences Meeting, 13–17 January 2014, National Harbor, MD, USA, 2014.

Al-Solihat, M. K. and Nahon, M.: Flexible Multibody Dynamic Modeling of a Floating Wind Turbine, Int. J. Mech. Sci., 142–143, 518–529, https://doi.org/10.1016/j.ijmecsci.2018.05.018, 2018.

Barthelmie, R., Pryor, S., Wildmann, N., and Menke, R.: Wind turbine wake characterization in complex terrain via integrated Doppler lidar data from the Perdigão experiment, J. Phys. Conf. Ser., 1037, 052022, https://doi.org/10.1088/1742-6596/1037/5/052022, 2018.

Bartl, J., Pierella, F., and Sætrana, L.: Wake Measurements Behind an Array of Two Model Wind Turbines, Enrgy. Proced., 24, 305–312, https://doi.org/10.1016/j.egypro.2012.06.113, 2012.

Bodini, N., Zardi, D., and Lundquist, J. K.: Three-dimensional structure of wind turbine wakes as measured by scanning lidar, Atmos. Meas. Tech., 10, 2881–2896, https://doi.org/10.5194/amt-10-2881-2017, 2017.

Burnham, D. C. and Hallock, J. N.: Chicago Monoacoustic Vortex Sensing System, Wake Vortex Decay, 4, 590–599, 1982.

Cormier, M., Caboni, M., Lutz, T., Boorsma, K., and Krämer, E.: Numerical analysis of unsteady aerodynamics of floating offshore wind turbines, J. Phys. Conf. Ser., 1037, 072048, https://doi.org/10.1088/1742-6596/1037/7/072048, 2018.

Fingersh, L. and Robinson, M.: Wind tunnel calibration of 5-hole pressure probes for application to wind turbines, 35th Aerospace Sciences Meeting and Exhibit, AIAA, USA, https://doi.org/10.2514/6.1997-854, 1998.

Fischenberg, D.: Charakterisierung von Wirbelschleppen aus In-Situ-Flugmessdaten der Falcon D-CMET, Tech. rep., DLR Institut für Flugsystemtechnik, available at: https://elib.dlr.de/70300/ (last access: 21 August 2019), 2011.

Jeong, J. and Hussain, F.: On the identification of a vortex, J. Fluid Mech., 285, 69–94, 1995.

Jonkman, J., Butterfield, S., Musial, W., and Scott, G.: Definition of a 5-MW Reference Wind Turbine for Offsore System Development, Technical report, National Renewable Energy Laboratory, Colorado, 2009.

Kim, Y., Jost, E., Bangga, G., Weihing, P., and Lutz, T.: Effects of ambient turbulence on the near wake of a wind turbine, J. Phys. Conf. Ser., 753, 032047, https://doi.org/10.1088/1742-6596/753/3/032047, 2016.

Kroll, N. and Fassbender, J. K.: MEGAFLOW – Numerical Flow Simulations for Aircraft Design, Springer Verlag GmbH, Berlin Heidelberg, 2005.

Lamb, H.: Hydrodynamics, Cambridge University Press, Cambridge, 1939.

Menke, R., Vasiljević, N., Hansen, K. S., Hahmann, A. N., and Mann, J.: Does the wind turbine wake follow the topography? A multi-lidar study in complex terrain, Wind Energ. Sci., 3, 681–691, https://doi.org/10.5194/wes-3-681-2018, 2018.

Menter, F.: Two-equation eddy-viscosity turbulence models for engineering applications, AIAA J., 32, 1598–1605, https://doi.org/10.2514/3.12149, 1994.

Pixhawk-Organisation: PixHawk 2.1 Autopilot description, available at: http://pixhawk.org, last access: 1 July 2019.

Rautenberg, A., Allgeier, J., Jung, S., and Bange, J.: Calibration Procedure and Accuracy of Wind and Turbulence Measurements with Five-Hole Probes on Fixed-Wing Unmanned Aircraft in the Atmospheric Boundary Layer and Wind Turbine Wakes, Atmosphere, 10, 124, https://doi.org/10.3390/atmos10030124, 2019a.

Rautenberg, A., Schön, M., zum Berge, K., Mauz, M., Manz, P., Platis, A., van Kesteren, B., Suomi, I., Kral, S. T., and Bange, J.: The Multi-Purpose Airborne Sensor Carrier MASC-3 for Wind and Turbulence Measurements in the Atmospheric Boundary Layer, Sensors, 19, 2292, https://doi.org/10.3390/s19102292, 2019b.

Sørensen, J. N., Mikkelsen, R., Sarmast, S., Ivanell, S., and Henningson, D.: Determination of Wind Turbine Near-Wake Length Based on Stability Analysis, J. Phys. Conf. Ser., 524, 012155, https://doi.org/10.1088/1742-6596/524/1/012155, 2014.

Subramanian, B., Chokani, N., and S. Abhari, R.: Drone-Based Experimental Investigation of Three-Dimensional Flow Structure of a Multi-Megawatt Wind Turbine in Complex Terrain, J. Sol. Energ.-T. ASME, 137, 1007–1017, 2015.

Vermeer, N.-J.: Local circulation on rotating wind turbine blades from velocity measurements in the wake of a model rotor, British Wind Energy Association Annual Wind Energy Conference 1992, Nottingham, 117–121, 1992.

Wang, Z. Y., Plate, E. J., Rau, M., and Keiser, R.: Scale effects in wind tunnel modelling, J. Wind Eng. Ind. Aerod., 61, 113–130, https://doi.org/10.1016/0167-6105(96)00049-9, 1996.

Wildmann, N., Hofsäß, M., Weimer, F., Joos, A., and Bange, J.: MASC – a small Remotely Piloted Aircraft (RPA) for wind energy research, Adv. Sci. Res., 11, 55–61, https://doi.org/10.5194/asr-11-55-2014, 2014a.

Wildmann, N., Ravi, S., and Bange, J.: Towards higher accuracy and better frequency response with standard multi-hole probes in turbulence measurement with remotely piloted aircraft (RPA), Atmos. Meas. Tech., 7, 1027–1041, https://doi.org/10.5194/amt-7-1027-2014, 2014b.

Wildmann, N., Vasiljevic, N., and Gerz, T.: Wind turbine wake measurements with automatically adjusting scanning trajectories in a multi-Doppler lidar setup, Atmos. Meas. Tech., 11, 3801–3814, https://doi.org/10.5194/amt-11-3801-2018, 2018.

Zhang, W., Markfort, C. D., and Porté-Agel, F.: Near-wake flow structure downwind of a wind turbine in a turbulent boundary layer, Exp. Fluids, 52, 1219–1235, https://doi.org/10.1007/s00348-011-1250-8, 2012.

A.2 Towards higher accuracy in wind farm deficit decay modelling - a comparison

Meteorol. Z. (Contrib. Atm. Sci.), Early Access DOI 10.1127/metz/2023/1183

Energy Meteorology

Towards higher accuracy in wind farm deficit decay modelling – a comparison

Moritz Mauz[1*], Stefan Emeis[2], Frederick Hoeckh[1], Bram van Kesteren[1], Andreas Platis[1] and Jens Bange[1]

[1]Department of Geoscience, Environmental Physics, University of Tübingen, Tübingen, Germany
[2]Institute for Meteorology and Climate Research, Karlsruhe Institute of Technology, Garmisch-Partenkirchen, Germany

(Manuscript received December 12, 2022; in revised form July 13, 2023; accepted July 18, 2023)

Abstract

Wind farm wake behaviour and forecasting is gaining the importance recently. It is especially relevant in the German Bight where space for wind farm clusters is limited, and wind farm wake lengths of up to 60 km have been measured. In this investigation newly proposed simple wind farm far-field recovery analytical wake model called SWIFFR is compared to the analytical EFFWAKE (Emeis, 2010) (Efficiency and Wake) wind farm wake model and the established Frandsen model (Frandsen et al., 2006). The models in this study are compared to measured in-situ airborne data, captured during the WIPAFF (wind park far field) project. Three specific flights are shown and compared to the respective model result of each analytical model. The SWIFFR model is derived from the Reynolds-averaged Navier-Stokes equation for the momentum conservation. It describes the wind speed recovery, as for example, in the wake of a wind farm from an atmospheric point of view, by acknowledging turbulent momentum from the atmosphere aloft of the wind farm wake and from the sides as well. A gain in accuracy in comparison to the EFFWAKE model is achieved. Analytical models provide computationally inexpensive results based on some assumptions and simplifications of the governing equations, which distinguishes this approach from purely empirical models.

Keywords: wind energy, off-shore wind farms, wake recovery, airborne measurements, analytical model, turbulence

1 Introduction

Regenerative energy sources have become a reliable power source for many countries, while the share of fossil energy sources is declining. One of the main regenerative sources is wind energy harvesting. Wind turbines (WTs) are spread all over the countryside, often providing decentralised power to the existing grid. However, energy production is achieved more efficiently in off-shore wind farms. In the early days of off-shore wind farm design, the dominating focus was cost per turbine or cost per surface area, ignoring wakes, their lengths and recovery. Looking back, the first wind farms are not among the most efficient ones. The spacing of individual WTs has become an important aspect in wind farm design and a lot of effort has been put into research to find a realistic cost ratio and to define minimum distances between WTs (Meyers and Meneveau, 2012; Yang et al., 2012). While the individual wake of a WT in an off-shore wind farm received a lot of attention, experimental in-situ studies evaluating the entire off-shore wind farm wake have only be conducted recently. The WIPAFF (wind park far field) project (Platis et al., 2020b; Platis et al., 2020a; Emeis et al., 2016) provides a unique data set of in-situ wind farm wake measurements. The data were captured at different thermal atmospheric conditions. Wake lengths of up to 60 km were found in stable atmospheric conditions.

Siedersleben et al. (2018) studied large off-shore wind farms and their effect on local wind fields using WRF (weather research and forecast) models under various atmospheric conditions. Off-shore wind farms can be expected to influence the meso-scale wind field (Siedersleben et al., 2018) and a turbine-atmosphere interaction on on-shore wind farms has been documented recently (Antonini and Caldeira, 2021). For weather forecast and wind farm efficiency considerations, these meso-scalic effects need to be quantifiable. Also Zhan et al. (2020) confirmed wake variability for different atmospheric stabilities using lidar (light detection and ranging) measurements for an on-shore wind farm.

Emeis (2010) proposed a simple analytical model to describe the flow field behind an off-shore wind farm. The model describes an exponential decay of the wind deficit and introduces a constant wind deficit decay rate α. In the presented work WIPAFF data are compared against the analytical model (EFFWAKE) proposed by Emeis (2010); Emeis (2022). The EFFWAKE (Efficiency and wake) model (Emeis, 2022) is an easy to set up model. Yet, it lacks accuracy in the wake recovery and does not take into account the wind farm ge-

---

[*]Corresponding author: Moritz Mauz, Department of Geoscience, Environmental Physics, University of Tübingen, Germany, e-mail: moritz.mauz@uni-tuebingen.de

DOI 10.1127/metz/2023/1183
Gebrüder Borntraeger Science Publishers, Stuttgart, www.borntraeger-cramer.com

ometry (Platis et al., 2018). An unsolved problem of the EFFWAKE model is the determination of one of its key parameters; the separation height Δz that separates the wind farm wake from the undisturbed flow above (Platis et al., 2020a). The results in Emeis (2010); Emeis (2017) were obtained by putting $z/\Delta z = 2$, with z the hub height of the wind farm.

In general, the influence of the wind farm geometry (WT spacing and density) and lateral momentum influx along the wake need also to be accounted for in the determination of the wind farm wake decay (Platis et al., 2018). Thus, there are still some uncertainties influencing the wind deficit decay rate that the EFFWAKE model can not formally address, since it assumes an infinite lateral extent of the wind farm. Therefore, an analytical model that could estimate any wind farm wake, determined by a few parameters, would help to quantify wind farm wakes properly while using little computational capacities.

Canadillas et al. (2020) compared the WIPAFF data to a median exponential best fit of the EFFWAKE model and additionally to the engineering software suite ‘WindFarmer’ (Hassan and Partners Ltd., 2014) which provides a modified wind farm wake model (Katik et al., 1987; Jensen, 1983). The WindFarmer bottom-up modelled results were found to be adequate for the data measured in neutral conditions. For stable conditions the wake lengths were significantly underestimated (Canadillas et al., 2020). Canadillas et al. (2020) showed that the wind farm wake can be described by an exponential function, best-fitting unknown parameters of the EFFWAKE model.

With wind farm wakes up to 60–80 km length it is likely that wind farms will interfere with each other, if they are not planned accordingly. Thus, also considering commercial software suites, there is a need for an easy to implement model that accounts for atmospheric stability. The proposed SWIFFR model provides such an analytical solution for the recovery of a wind velocity depression, e.g. typically found behind farm wakes, derived from the momentum conservation equation of the free flow.

One advantage of the proposed top-down model is that this model provides an analytical solution, with one less unknown parameter (vertical separation height), compared to the EFFWAKE model. Another advantage is that the wind farm is treated like a ‘black box’, resulting in a wake centre-line, without the need to compute the wake for each single turbine in the wind farm (bottom-up approach) as shown e.g. in Niayifar and Porté-Agel (2016) or the quite popular Frandsen model (Frandsen et al., 2006). Frandsen et al. (2006) relates the wake velocity directly to the thrust coefficient C_T of the wind turbine. This model uses a wake expansion parameter k, to effectively calibrate the model. This parameter varies, depending on turbine spacing, boundary layer conditions and turbine dimensions. Hence, it is problematic and almost impossible to define a common expansion factor (Andersen et al., 2014). Simple top-down analytical solutions can circumvent such problems and are also interesting for meso-scale WRF simulations or quick wake length assessments. The proposed model can also be applied to estimate off-shore wind farm spacings and studying wind farm wake interactions and shadowing. It is shown below that the SWIFFR model can be used with several forms of parametrisation.

2 Theory and methods

2.1 The EFFWAKE model

In this study the wind farm wake model derived by Emeis (2010) is referred to as the EFFWAKE model. It has been used by Platis et al. (2018); Platis et al. (2020a) and Canadillas et al. (2020) to compare in-situ airborne wind farm wake measurements to an analytical model. A detailed derivation is given in Emeis (2010); Emeis (2017). Nevertheless, a brief introduction of the model is given below.

The model is using a semi-empirical approach and assumes a wind farm with an infinite lateral extent. The EFFWAKE model further assumes a homogeneous inflow along the infinite lateral extent of the wind farm and is based on an equilibrium between momentum dissipation by the wind farm and a resupply of momentum by turbulent fluxes from the layer atop. Therefore, the momentum influx that restores the kinetic energy back to the flow has to come from the airflow above the wind farm. For its derivation the EFFWAKE model considers an accelerating air parcel with its remaining or residual wind speed u_r along the wake at hub height.

$$\frac{\partial u_r}{\partial t} = -\frac{\partial \overline{u'w'}}{\partial z} \tag{2.1}$$

The Reynolds-averaged turbulent vertical momentum flux in mean wind direction (right side of Eq. 2.1), where the primes describe the fluctuation from the mean quantity, is substituted using a bulk parametrisation (gradient method), introducing a turbulent momentum transfer coefficient K_m which varies with height in the Prandtl layer, however it is assumed constant at hub height z:

$$\overline{u'w'} = -K_m \frac{u_0 - u_r}{\Delta z} \tag{2.2}$$

The free stream velocity u_0 aloft and in front of the wind park or wind turbine is separated by Δz from the hub height, the assumed vertical wake-centre line. Thus the momentum transfer takes place along a vertical distance Δz (s.a. Figure 1). Since only the two velocities u_r in the wake at hub height and u_0 in the free stream (above the wind farm) are assumed, distance differentials can be written as differences and a first order differential equation can be formed:

$$\frac{\partial u_r}{\partial t} + \frac{K_m}{\Delta z^2} u_r = \frac{K_m}{\Delta z^2} u_0, \tag{2.3}$$

which has the solution

$$u_r(t) = u_0 + c\ \exp\left(-\frac{K_m}{\Delta z^2}t\right). \tag{2.4}$$

Applying the initial conditions $u_r(t = 0) = u_{r0} = u_0 + c$ gives a time dependent solution for the normalised residual wind velocity $u_r(t)/u_0$ at hub height h:

$$\frac{u_r(t)}{u_0} = 1 + \left(\frac{u_{r0}}{u_0} - 1\right)\exp\left(-\alpha_\mathrm{E} t\right), \text{ with: } \alpha_\mathrm{E} = \frac{K_\mathrm{m}}{\Delta z^2} \tag{2.5}$$

Platis et al. (2020a) resolve the temporal dependency by substituting t with $\bar{t} = \frac{x_i}{u_{50\,\%}}$, which gives an average time of flight of an air parcel from the beginning of the wake to the position x_i in the wake. This parcel travels with an average velocity $u_{50\,\%}$ through the wake. This is also the velocity at which the wind deficit is recovered by 50 %. The wake deficit decay rate α_E (index E indicating the EFFWAKE wake deficit decay rate) is assumed constant along the wake with momentum transfer from $z = h + \Delta z$ aloft the wake. The atmospheric thermal stratification or stability influences K_m by the friction velocity u_* and a stability correction function ϕ_m, in the lower atmosphere (Garratt, 1994a).

$$K_m = \frac{\kappa u_* z}{\phi_m(z/L)} \tag{2.6}$$

While for a neutral stratification $\phi_m(z/L) = 1$ can be applied, for unstable and stable stratifications different corrections apply (Businger et al., 1971).

$$\phi_m\left(\frac{z}{L}\right) = \begin{cases} 1/\gamma & \text{for } \frac{z}{L} < 0 \\ 1 & \text{for } \frac{z}{L} = 0 \\ 1 + a\frac{z}{L} & \text{for } \frac{z}{L} > 0 \end{cases} \tag{2.7}$$

With $\gamma = (1 - b\ z/L)^{0.25}$ and L the Obukhov length, $a = 5$ and $b = 16$. A numerical modeller that has access to stability data could now insert a stability correction into the model. In the EFFWAKE model the atmospheric stability is represented by the stability correction function ϕ_m, if apprehensible. But since the ϕ_m stability correction is essentially a constant, it effectively simply weights the momentum transfer coefficient K_m (same as a change in Δz). Meaning that whenever the EFFWAKE model is tuned or set up, it is not distinguishable whether the stratification correction or the separation height Δz is adjusted. Thus, as Δz and the Obukhov length are not obtainable for the presented cases (e.g. lack of surface virtual potential temperature flux data), the EFFWAKE model will be used for $\phi_m = 1$. Both parameters influence the wind deficit decay rate α_E, and since the thermal stability also impacts the boundary layer aloft the wind farm, only Δz will later be modified to fit the EFFWAKE model to the data. This treats α_E as a 'black box', as done by Platis et al. (2020a).

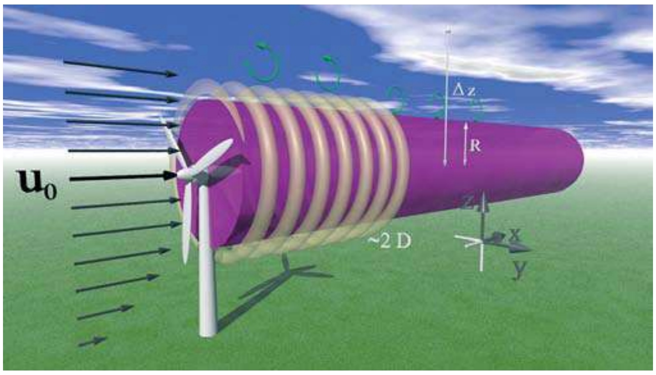

Figure 1: Wake characteristics displayed at a single turbine. The incoming horizontal wind u_0 ($= u_f|_{x=0}$) is almost steady over the rotor plane. The helical blade-tip vortex absorbs turbulent momentum flux from aloft, until the helix disintegrates (at ≈ 2D) and turbulent influx can refill the wake deficit. The EFFWAKE model assumes this distance to be Δz. Since this parameter is usually not determinable and unknown in the EFFWAKE model; the new proposed model approach uses the rotor radius R as the characteristic distance associated to the turbulent momentum influx.

Canadillas et al. (2020) tested the EFFWAKE model from an engineering point of view by calculating the initial wind velocity deficit u_{r0}/u_0 as a function of ambient turbulent intensity I_u, the farm thrust coefficient c_t, effective drag coefficient C_D and individual converter spacing (WTs per certain distance). For more details and the implementation the reader is referred to appendix B in Canadillas et al. (2020). In contrast to this full-on calculated wind farm wake, Platis et al. (2020a) substituted the initial wind deficit behind the wind farm u_{r0}/u_0 with a measured value from the WIPAFF campaign and compares the EFFWAKE model to these measured in-situ data.

Both studies described above, with different approaches, show a certain level of flexibility of the EFFWAKE model. A drawback of the EFFWAKE model is the unknown separation height parameter Δz. In the novel analytical model, presented in this work, this separation height is set fix to the rotor radius R of the wind turbines in the wind farm. It is used as a characteristic length associated to the wind farm wake, defining an altitude (boundary) above the wind farm through which all vertical momentum transfer has to transverse.

2.2 The SWIFFR model

For the SWIFFR (simple wind farm far-field recovery) model derivation we start with a flow around an offshore wind farm. Equation 2.8, the starting point for the newly proposed analytical wind deficit model, is the conservation of momentum in the incompressible mean flow using Einstein summation notation (Stull, 1988). After Reynolds averaging and applying the Boussinesq eddy viscosity assumption, the conservation of momentum can be written as:

$$\underbrace{\frac{\partial \overline{u_i}}{\partial t}}_{\text{I}} + \underbrace{\overline{u_j}\frac{\partial \overline{u_i}}{\partial x_j}}_{\text{II}} + \underbrace{\delta_{i3} g}_{\text{III}} \underbrace{- f_c \epsilon_{ij3} \overline{u_j}}_{\text{IV}} + \underbrace{\frac{1}{\overline{\rho}}\frac{\partial \overline{p}}{\partial x_i}}_{\text{V}} - \underbrace{\frac{\nu \partial^2 \overline{u_i}}{\partial x_j^2}}_{\text{VI}} + \underbrace{\frac{\partial \overline{u_i' u_j'}}{\partial x_j}}_{\text{VII}} = 0 \qquad (2.8)$$

Here, $i, j = 1, 2, 3$ for all three directions in space, g is the gravitational acceleration, p the static pressure, f_c the Coriolis parameter, ν the kinematic viscosity, ϵ the Levi-Civita symbol and ρ the density of air.

Term I	represents storage of mean momentum.
Term II	describes advection of mean momentum by the mean wind.
Term III	allows gravity to act in the vertical direction only.
Term IV	describes the influence of the Coriolis force.
Term V	describes the mean pressure-gradient force.
Term VI	represents the influence of viscous stress on the mean motions.
Term VII	represents the influence of Reynolds stress on the mean motions.

Various terms in the Navier-Stokes equations can be neglected in boundary-layer flows with very low friction (Prandtl, 1904). Thus, assuming only very small changes in atmospheric pressure along the wind farm wake, term V can be neglected. Term VI represents the viscous stress but observations in the atmosphere indicate that the molecular diffusion is several order of magnitudes smaller compared to the other terms and can be neglected (Stull, 1988). Satellite imagery using synthetic aperture radar (SAR) show wake lengths up to 50 km and larger which show no to little deflection by Coriolis forces (Djath et al., 2018). Also for the sake of simplification term IV is neglected in this study. Considering only the wake-centre line of a one-dimensional ($i = 1$) steady-state flow, term I and III are zero and can also be deleted. Equation 2.8 can now be simplified. The mean reduced horizontal wind speed $\overline{u}$ in the wake at hub height in x-direction along the wake-centre line for an incompressible flow, with the remaining terms II and VII, can be approximated as:

$$\overline{u}\frac{\partial \overline{u}}{\partial x} + \overline{v}\frac{\partial \overline{u}}{\partial y} + \overline{w}\frac{\partial \overline{u}}{\partial z} = -\frac{\partial \overline{u'u'}}{\partial x} - \frac{\partial \overline{u'v'}}{\partial y} - \frac{\partial \overline{u'w'}}{\partial z} \qquad (2.9)$$

Applying the product rule to each term on the left hand side of Eq. 2.9 yields:

$$\overline{u}\frac{\partial \overline{u}}{\partial x} = \frac{\partial \overline{u}^2}{\partial x} - \overline{u}\frac{\partial \overline{u}}{\partial x}; \qquad (2.10)$$

$$\overline{v}\frac{\partial \overline{u}}{\partial y} = \frac{\partial (\overline{u}\,\overline{v})}{\partial y} - \overline{u}\frac{\partial \overline{v}}{\partial y}; \qquad (2.11)$$

$$\overline{w}\frac{\partial \overline{u}}{\partial z} = \frac{\partial (\overline{u}\,\overline{w})}{\partial z} - \overline{u}\frac{\partial \overline{w}}{\partial z}; \qquad (2.12)$$

The left side of Eq. 2.9 can now be rewritten as:

$$\frac{\partial \overline{u}^2}{\partial x} - \overline{u}\frac{\partial \overline{u}}{\partial x} + \frac{\partial (\overline{u}\,\overline{v})}{\partial y} - \overline{u}\frac{\partial \overline{v}}{\partial y} + \frac{\partial (\overline{u}\,\overline{w})}{\partial z} - \overline{u}\frac{\partial \overline{w}}{\partial z} = \frac{\partial \overline{u}^2}{\partial x} + \frac{\partial (\overline{u}\,\overline{v})}{\partial y} + \frac{\partial (\overline{u}\,\overline{w})}{\partial z} - \overline{u}\underbrace{\left[\frac{\partial \overline{u}}{\partial x} + \frac{\partial \overline{v}}{\partial y} + \frac{\partial \overline{w}}{\partial z}\right]}_{=0} \qquad (2.13)$$

Since a steady-state incompressible flow is considered, the part in brackets in Eq. 2.13 is zero (divergence-free flow). The left side of Eq. 2.9 can now be written using Eq. 2.13, which results in Eq. 2.14:

$$\underbrace{\frac{\partial (u_r \cdot u_r)}{\partial x}}_{A} + \underbrace{\frac{\partial (\overline{v} \cdot u_r)}{\partial y}}_{B} + \underbrace{\frac{\partial (\overline{w} \cdot u_r)}{\partial z}}_{C} = -\underbrace{\frac{\partial (\overline{u'u'})}{\partial x}}_{D} - \underbrace{\frac{\partial (\overline{u'v'})}{\partial y}}_{E} - \underbrace{\frac{\partial (\overline{u'w'})}{\partial z}}_{F} \qquad (2.14)$$

With $u_r = \overline{u}$ the reduced wind speed in the wind farm wake along the centre-line and the Reynolds shear stresses on the right-hand side.

Furthermore the continuity equation for incompressible steady-state flow is valid:

$$\frac{\partial v}{\partial y} + \frac{\partial w}{\partial z} = -\frac{\partial u_r}{\partial x} \qquad (2.15)$$

The left hand side (term A, B and C) of Eq. 2.14 at the centre line can now be simplified using Eq. 2.15:

$$\frac{\partial (u_r \cdot u_r)}{\partial x} + \underbrace{u_r\frac{\partial \overline{v}}{\partial y} + u_r\frac{\partial \overline{w}}{\partial z}}_{-u_r \frac{\partial u_r}{\partial x}} + \underbrace{\overline{v}\frac{\partial u_r}{\partial y}}_{=0} + \underbrace{\overline{w}\frac{\partial u_r}{\partial z}}_{=0} = 2u_r\frac{\partial u_r}{\partial x} - u_r\frac{\partial u_r}{\partial x} = u_r\frac{\partial u_r}{\partial x} = \frac{1}{2}\frac{\partial u_r^2}{\partial x} \qquad (2.16)$$

At the wake-centre line the mean lateral velocity component $\overline{v} = 0$ due to symmetry reasons. For simplicity, the same argument can be made for the vertical wind component $\overline{w}$, considering a homogenous rectangular cross-section of the wake (lateral).

Let us now consider the right-hand side (terms D, E and F) of Eq. 2.14. Concerning term D, it is common, to neglect this longitudinal change (i.e. in x-direction) of the longitudinal turbulent flux of longitudinal momentum in comparison to $\partial u_r^2/\partial x$. The lateral Reynolds shear stress created by a WT in a wind farm is considered to be of same extent as the vertical shear stress due to the radial symmetry of the rotor plane. Thus, we can write:

$$\overline{u'v'} \approx \overline{u'w'} \tag{2.17}$$

Since furthermore a steady-state and stationary solution is considered, and no implicit dependencies of u are present, we use the total derivative instead of the partial. The remaining terms E and F of the right-hand side of Eq. 2.14 can therefore be rewritten:

$$-\frac{d\overline{u'w'}}{dy} - \frac{d\overline{u'w'}}{dz} = -\frac{d\overline{u'w'}}{f \cdot dz} - \frac{d\overline{u'w'}}{dz} = -\frac{d\overline{u'w'}}{dz}\left(\frac{1}{f} + 1\right) \tag{2.18}$$

With dy the lateral separation of the wind farm centre line from the free stream velocity u_0 and dz the vertical separation from the free stream velocity u_0. The lateral separation length is a manifold of dz, therefore $dy = f \cdot dz$, and since dz is the rotor blade length, for wind farms that consist of at least two rows of wind turbines along the wind direction $f > 1$. This introduces a way to recognise wind farm geometry when considering turbulent momentum influx into the wake from the sides affecting the wind deficit at the wake-centre line. Note that for the case of a single WT $dy = dz$ and therefore, $\frac{1}{f} + 1 = 2$, or $f = 1$ which would be the solution for the Reynolds stress terms for a single WT. Also, the wider a wind farm is built, the less prevalent is the lateral influx. The narrower a wind farm is built, the larger the influence of lateral momentum influx becomes.

The Reynolds shear stress is further simplified by an empirical relation (gradient method), assuming a first order distribution of the vertical Reynolds shear stress, s.a. Eq. 2.2. Therefore, the Reynolds shear stress is expressed using a momentum transfer coefficient K_m (s.a. Eq. 2.6) and is brought to a finite difference form at the wake-centre line at hub height h. In this approach we substitute Δz with the rotor length R, neglecting wake expansion:

$$\frac{d\overline{u'w'}}{dz} \to \frac{\Delta\overline{u'w'}}{R} = \frac{\overline{u'w'}(h + R/2) - \overline{u'w'}(h - R/2)}{R} \tag{2.19}$$

In order to obtain the flux-divergence at height h for all x, assuming a symmetric wake flow above and below the centre line, the resulting form is:

$$\begin{aligned} \frac{\Delta\overline{u'w'}}{R} &= -K_\mathrm{m}\frac{(u_0 - u_r)/R - (u_r - u_0)/R}{R} \\ &= -2K_\mathrm{m}\frac{u_0 - u_r}{R^2} \end{aligned} \tag{2.20}$$

$u_0 - u_r$ is the difference (wake deficit) between the free flow velocity u_0 above the wind farm and the residual wind speed u_r at the wind farm wake-centre line. Equation 2.14 is now simplified introducing the wake decay rate α.

$$\frac{du_r^2}{dx} = \underbrace{\frac{CK_\mathrm{m}}{R^2}\left(\frac{1}{f} + 1\right)}_{\alpha}(u_0 - u_r) = \alpha u_0 - \alpha u_r, \tag{2.21}$$

with here: $C = 4$ and $f \gg 1$

In this symmetric bulk approximation it is assumed that the turbulent momentum influx from aloft is the same as from below. In reality this is not the case. This is why the geometric factor C is smaller than 4 in reality and should at least be halved. Also the lateral inflow of turbulent momentum flux is primarily responsible for the shape of the wind farm wakes, i.e. shaping and shifting the outer boundary of the wind farm wake. Therefore, we assume a minimum influence of lateral influx at the wake-centre line. Hence, a factor $C = 1$ is considered in this study.

We continue to find an approximate solution of Eq. 2.21:

$$\frac{du_r^2}{dx} = 2u_r\frac{du_r}{dx} = \alpha u_0 - \alpha u_r$$

Rearranging and moving dx to the other side

$$\Longleftrightarrow \; du_r = \left(\frac{\alpha u_0}{2u_r} - \frac{\alpha}{2}\right)dx \tag{2.22.1}$$

the next step is integrating over du_r on the left and over dx on the right. However:

Equation 2.22.1 is the difference form of a non-homogeneous non-linear differential equation (DE) of first order. The solutions u_r^hom of the corresponding homogeneous DE are of the form:

$$u_r^\mathrm{hom} = \pm\sqrt{\alpha u_0 x} \tag{2.22.2}$$

which actually is realistic: the reduced wind speed u_r increases by the square-root of the horizontal distance x – quite similar to the vertical development of a turbulent boundary layer or an internal boundary layer in heterogeneous terrain (Garratt, 1987; Garratt, 1994b; Hanna, 1987). However, a particular solution of the non-homogeneous DE 2.21 could not be found. In order to find an approximated solution, u_r is treated as a constant on the right-hand side of Eq. 2.22.1 and the simplified DE is solved in the following continuing from Eq. 2.22.1.

$$\Longleftrightarrow \; u_r = \left(\frac{\alpha u_0}{2u_r} - \frac{\alpha}{2}\right)x + c$$

A short assessment of the order of magnitude assures that the introduced error by treating u_r as a constant for the integration step, is small, using observed wind farm wake lengths up to 60 km (Platis et al., 2018; Siedersleben et al., 2018). It is assumed that the change of the velocity gradient along x is small (with the velocity gradient in the order of $\frac{\Delta u}{\Delta x} = -\frac{u_0 - u_r(0)}{60000\,\mathrm{m}} \approx -\frac{1}{10000}\,\mathrm{s}^{-1}$), which is several orders of magnitude smaller than the Reynolds shear stress terms or its gradient approximation wrapped in α. Let us now work with this simplified equation, where we focused on integrating u_r over du_r and neglected any dependency of u_r over small dx (considering a wind farm wake length of at least 40000 m). Thus assuming that the solution of 2.22.1 is carried by solving for u_r by solely integrating over du_r and neglecting its dependency over dx, treating the latter dependency as quasi-constant.

Rearranging again and multiplying with u_r

$$\iff u_r^2 + \frac{\alpha u_r x}{2} - cu_r - \frac{\alpha u_0 x}{2} = 0$$

rewrite as a quadratic equation

$$\iff u_r^2 + u_r\left(\frac{\alpha x}{2} - c\right) - \frac{\alpha u_0 x}{2} = 0 \qquad (2.22.3)$$

This quadratic equation has two solutions:

$$u_{r_{1,2}}(x) = \frac{1}{2}\left(\left(c - \frac{\alpha x}{2}\right) \pm \sqrt{\left(\frac{\alpha x}{2} - c\right)^2 + 2u_0\alpha x}\right) \qquad (2.23)$$

While only the positive solution is physically relevant, resulting in positive wind speeds, c can now be determined using initial boundary conditions, i.e. for $x = 0$. The initial conditions can be measured, calculated or a theoretical value can be taken, e.g. $u_r(0) \approx 0.3u_0$ using Betz law (Betz, 1920), if applicable, resulting in $c = 0.3u_0$ (e.g. behind a single wind turbine). For the wind farm wakes used in this study, the values shown in Table 2 are used.

Equation 2.23 describes the residual wind speed u_r at each position x along the wake-centre line. The wind-deficit decay rate α, with K_m the momentum transfer coefficient, which will be assumed constant over x.

The predicted wake length is an important parameter that serves as quality control for any wake model. The wake length depends, aside of the horizontal wind speed at hub height, primarily on the thermal stability (McKay et al., 2012). As such, the SWIFFR model also has to work for different thermal atmospheric stabilities. The atmospheric stability can be implemented in the same way as in the EFFWAKE model as shown in Eq. 2.6. We assume that Eq. 2.6 is applicable for a WTs with hub heights $h = 90$ m.

The SWIFFR model is similar to the EFFWAKE model in the way the wake is treated and simplified. However, the EFFWAKE uses a Lagrangian point of view, solving Term I and Term VII of Eq. 2.8, while the SWIFFR model follows an Eulerian approach by solving for a stationary solution of Eq. 2.8, in particular, using Term II and Term VII.

2.3 Similarity to the Frandsen model

The square-root function of the SWIFFR model, Eq. 2.23, is similar to the Frandsen et al. (2006) model in regard of the proposed wind farm wake shape. The model handles a regular array geometry with straight rows of wind turbines and equidistant spacing between units in each row and equidistant spacing between rows (Frandsen et al., 2006), as does the SWIFFR model. The Frandsen model can be utilized to get a wind farm wake shape by using an effective wind farm thrust coefficient C_T^*, a wind farm parameter, instead of the rotor diameter D, and an effective wake expansion coefficient k, the latter two can be written as single parameter k^*:

$$\frac{u_r}{u_0} = \frac{1}{2}\left(1 + \sqrt{1 - \frac{2C_\mathrm{T}^*}{1 + 2k^* x}}\right) \qquad (2.24)$$

The normalisation wind speed u_0 is the free stream velocity corresponding to the first measurement, closest to the wind farm, which is presumably the velocity in the inflow, at the time of the measurement.

While the Frandsen model is a popular representative of a bottom-up model and the SWIFFR model constitutes a top-down approach, resulting in a similar equation, a comparison of the two models is shown in Section 4. The differences and commonalities of the two models will be discussed in Section 6.

3 Data treatment and model setup

3.1 In-situ wake data

The airborne-measured wind farm wake data from the WIPAFF project are accessible to the community via the PANGAEA database (Bärfuss et al., 2019; Lampert et al., 2020). The data used in this particular study was measured on August 8, 2017. Three measurement flights (#30, #31, #41) collectively contain seven wind farm wakes behind four different wind farms, Amrumbank West (AW), Nordsee Ost (NO), Meerwind Süd/Ost (MSO), and Gode Wind I/II (GW I/II) are used in the following. An overview of all flights is given in Platis et al. (2018).

The measurements were performed with the research aircraft Dornier Do-128 of the Technische Universität of Braunschweig. It is equipped among others with sensors for temperature, humidity, pressure, and wind components, sampling with a frequency of 100 Hz. Details about the measurement devices can be found in Lampert et al. (2020). The airspeed of the aircraft during the measurements flights was 66 m s^{-1}.

Figure 2 shows an exemplary measurement of the horizontal wind field u_hor normalised by the free, undisturbed flow velocity u_f, around and in the wake of the wind farm cluster AW/NO/MSO. The main wind direction is along the x-axis. To determine u_f, the mean wind speed is determined to the left and right of the wind farm cluster for each flight leg (straight part of the flight track) at various distances x and a minimum distance of about four kilometres from the adjacent wakes.

The flight track is indicated by a black solid line. The dashed black line is following the wake minimum

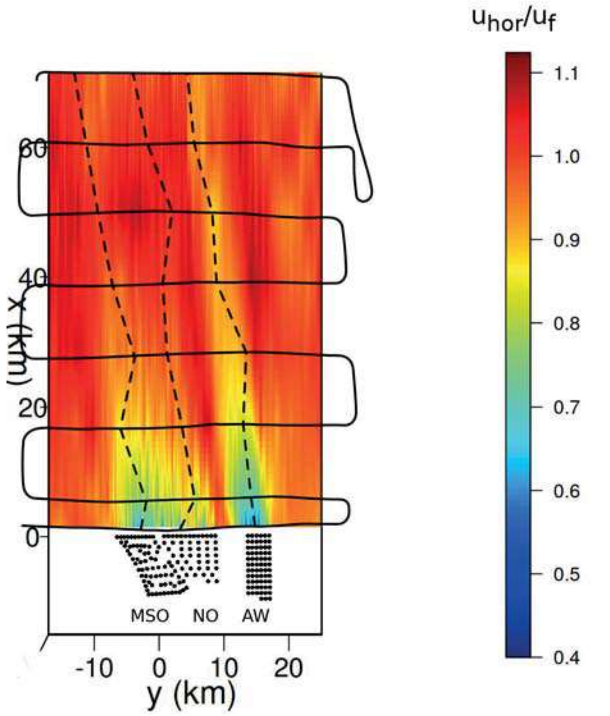

Figure 2: Normalised horizontal wind speed from an exemplary measurement (flight #31) behind the three wind farms Amrumbank West (AW), Nordsee Ost (NO), and Meerwind Süd/Ost (MSO) with eastern wind direction. The data is linearly interpolated between flightpaths in x-direction. The flight path (meander pattern) is indicated as a black solid line. The dashed black line follows the wake minimum. Black dots indicate individual WTs.

where the residual wind velocity $u_r(x)$ in the wake is calculated. Along the flight path, with the wake minimum in its centre, the measurements of an ≈ 260 m section (400 data points) are averaged.

The EFFWAKE and SWIFFR models need an average wind velocity of the undisturbed atmospheric flow at hub height (u_0) as input. But since there are also free-stream velocity measurements available along the wake, the normalisation velocity at each distance x is set to be $u_f(x)$, instead of the incoming wind speed u_0 in front of the wind farm, throughout this study (s.a. Figure 3). This has been applied to both models, and increases the prediction accuracy, since the wind field is slightly changing over the time span of the measurements due to meso-scale effects (s.a the slight wind velocity gradient in Figure 2).

For a successful analytical solution only one more parameter aside u_f or u_0 is needed; the friction velocity u_*. This parameter has been directly taken from Table 4 ($u_{*\text{FINO}}$) from Platis et al. (2020a) for the respective flights which has been measured either by the FINO 1 or the FINO 3 mast in the German Bight. Platis et al. (2020a) calculated $u_{*\text{FINO}}$ using the direct method (calculation by the vertical fluxes of horizontal momentum).

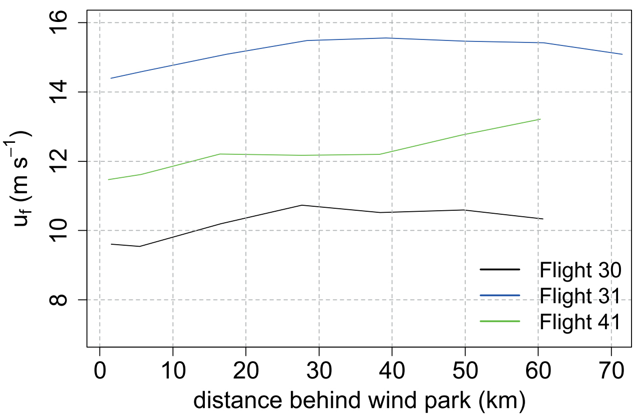

Figure 3: Free flow u_f velocities along the main wind direction next to the wind farm clusters AW/NO/MSO (flights #30 and #31) and GW I/II (flight #41).

3.2 EFFWAKE

The EFFWAKE model relies on a separation layer Δz. This separation height is not determinable from the measured data and is a function of stability, wind farm geometry and atmospheric boundary conditions, e.g. a possible inversion near the hub height (Platis et al., 2020a). Therefore, aside different exponential fits with different Δz, an exponential best fit of the EFFWAKE model is shown in Section 4. The fit is done the same way as implemented in Platis et al. (2020a). Equation 3.1 uses a wind deficit decay rate α_{Ebf} that fits best to the in-situ wind farm wake data, using the first measurement at distance $x_1 \approx 2$ km as a constraint.

$$\frac{u_r(x)}{u_f(x)} = 1 - \left(1 - \frac{u_r(x)}{u_f(x)}\right)\exp(-\alpha_{\text{Ebf}}t(x)) \tag{3.1}$$

The best fit solution is the solution with the smallest root-mean-square deviation (RMSD):

$$\text{RMSD} = \sqrt{\frac{1}{N}\sum_{i=1}^{N}\left(u(x)_i^{\text{model}} - u(x)_i^{\text{meas}}\right)^2} \tag{3.2}$$

N is the number of averaged wake measurements per wake, $u(x)_i^{\text{model}}$ and $u(x)_i^{\text{meas}}$ are the modelled and the measured residual wind velocities in the wake.

The time dependency in Eq. 3.1 is solved by substituting $t(x_i)$:

$$t(x_i) = \frac{x_i}{u_f(x_i)} \tag{3.3}$$

which is approximately the travel-time of an air parcel to position x_i outside of the wake taking into account slight variations in the mean wind speed in the incoming flow. This systematically introduces an error in the model which decreases with distance x, as the wind deficit

Table 1: Determination of the geometrical factor f from wind farm dimensions considering the main wind direction in the SWIFFR model.

Wind farm	lateral extent [m]	vertical extent [m]	f [–]
AW	2400	60	40
NO	3000	60	50
MSO	2500	60	42
GW I/II	5000	60	80

$(u_f - u_r)$ decreases, and the wind speed in the wake is getting closer to the free flow velocity u_f.

Starting from the wind deficit decay rate of the EFFWAKE model:

$$\alpha_{\mathrm{Ebf}} = \frac{K_\mathrm{m}}{\Delta z_\mathrm{bf}^2} = \frac{\kappa u_*(h + \Delta z_\mathrm{bf})}{\Delta z_\mathrm{bf}^2}, \tag{3.4}$$

which is a computed best-fit (least-square fit) wind-deficit decay rate α_{Ebf}. From there, Δz_bf is solved for each wind farm wake by:

$$\Delta z_\mathrm{bf} = \frac{1 + \sqrt{1 + 4\alpha_* h}}{2\alpha_*}, \text{ with } \alpha_* = \frac{\alpha_{\mathrm{Ebf}}}{\kappa u_*}, \tag{3.5}$$

which is then used for comparison and discussion.

3.3 SWIFFR

In contrast to the EFFWAKE model, the proposed analytical solution in this study is using a fixed distance R (the rotor blade length) to the vertical wake boundary, measured from hub height. However, aside the free flow velocity u_f the SWIFFR model needs an additional parameter c which is derived from initial conditions (s.a. Section 2.2). These conditions were estimated, and the exact value is taken that the analytical solution passes through the measurement at distance $x_1 \approx 2000$ m. The wind farm capacity is also considered at the time of the measurement to check for plausibility (www.energy-charts.info).

The geometrical factor f used in the SWIFFR model for the respective wind farms by calculating f from the cross-section of the wind farm perpendicular to the main wind direction:

$$f = \frac{\text{lateral extent from wake centre line}}{\text{vertical extent from hub height}} \tag{3.6}$$

The resulting values are shown in Table 1.

3.4 Comparison with the Frandsen (2006) model

For the comparison of the Frandsen and the SWIFFR model parameters from Table 2 are used. The thrust coefficient C_T^* is set to match $u_r(0)/u_f$ from Table 2. The normalised wake widening coefficient k^* is set to coincide with $u_r(60000)/u_0$ of the SWIFFR model. For this comparison the SWIFFR model is set up using Eq. 2.23 with $u_0 = u_f(0)$ assuming that the initial wind velocity in front of the wind park $u_0 \approx u_f(0)$. Keep in mind that $u_f(0)$ is measured at around 500–600 m in the wake and cannot be measured at $x = 0$ m due to practical and safety reasons.

In this comparison the SWIFFR model is used as sole prediction tool as the Frandsen model as well. Hence, assuming constant wind conditions and no adjustment of the free flow wind velocity $u_f(x)$ along the wake.

4 Results

The results of the wind farm wake analysis is given in the following by looking into three flights from the WIPAFF campaign 2017. The data for flights #30 and #31 were captured on August 8, 2017. Flight #30 in the morning from 08:30 to 12:30 UTC, flight #31 in the afternoon from 13:00 to 17:00 UTC. Those two flights are especially interesting, since they provide measurements throughout a whole day as the marine boundary layer evolves. These two flights also enable a comparison of three wind farm wakes with the same inflow conditions, due to the vicinity of the three wind farms.

Table 2 lists all model parameters for the presented flights and wind farm wakes. The EFFWAKE model is represented by the exponential best fit in the table, from which a Δz_bf has been back-calculated assuming the friction velocity u_* associated with this flight (s.a. Section 3.1) and the present atmospheric conditions. The wind deficit decay rate α has also been normalised by the mean inflow conditions, calculated from u_f (s.a. Figure 3). This way the wind deficit decay rate is also more tangible.

4.1 Flight #30

For flight 30 the atmospheric conditions were similar to flight #31, but the stratification was slightly less stable. The friction velocity u_*, taken from Platis et al. (2020a), was 0.22 m s^{-1}, the average free stream velocity was $\overline{u_f} = 10.2$ m s^{-1} with easterly wind from 80°. The Amrumbank West wind farm was operating between 42–76 % capacity during the time span of the measurements (www.energy-charts.info). During flight #30 the thermal stratification shows an almost neutral gradient, with a thermal inversion at 160 m above sea level. Thus, with the inversion at 160 m, the rotor blade area remains completely in the neutral layer (Platis et al., 2020a). Figure 4 shows the measurements behind the wind farms and the analytical solutions for the SWIFFR and EFFWAKE model. The latter is shown for different Δz and also for the best-fit wind deficit decay rate.

Figure 4 shows the in-situ measurements, the SWIFFR model solution (thick black line), the EFFWAKE best fit (red dashed line) and EFFWAKE solution for different Δz (grey-shaded lines).

Table 2: Model parameters and root-mean-square deviations (RMSD) of the EFFWAKE and SWIFFR model for all presented cases. With $u_r(0)/u_f(0) = c$ and C_T the thrust coefficient of the wind farm derived from the Frandsen model.

Flight No.	**Wind farm**	u_* [m s^{-1}]	α_Ebf [h^{-1}]	$\alpha/\overline{u}_f$ [km^{-1}]	Δz_bf [m]	$c\vert_{x=0}$ [–]	C_T [–]	**Π** [–]	**RMSD · 10³** [m s^{-1}]
EFFWAKE (best fit)									
30	AW	0.22	1.26	0.034	320	0.73	0.45	0.33	41
30	NO	0.22	2.76	0.075	170	0.59	0.49	0.29	40
30	MSO	0.22	2.26	0.061	200	0.78	0.39	0.30	27
31	AW	0.29	1.40	0.026	370	0.61	0.50	0.31	41
31	NO	0.29	3.40	0.062	180	0.63	0.49	0.31	38
31	MSO	0.29	3.60	0.066	180	0.70	0.45	0.32	22
41	GW I/II	0.21	1.00	0.022	430	0.68	0.48	0.33	39
SWIFFR			α [h^{-1}]		R [m]				
30	AW	0.22	13.5	0.365	60	0.65	0.45	0.29	33
30	NO	0.22	13.4	0.362	60	0.55	0.49	0.27	45
30	MSO	0.22	13.4	0.365	60	0.73	0.39	0.28	17
31	AW	0.29	17.8	0.325	60	0.35	0.50	0.18	47
31	NO	0.29	17.7	0.322	60	0.55	0.49	0.27	21
31	MSO	0.29	17.6	0.321	60	0.65	0.45	0.29	25
41	GW I/II	0.21	9.0	0.200	60	0.60	0.48	0.29	37
Frandsen					$k^* \cdot 10^5$ [m^{-1}]		C_T^*		
30	AW				6.25	0.66	0.45	0.30	39
30	NO				5.31	0.57	0.49	0.28	45
30	MSO				7.10	0.74	0.39	0.28	20
31	AW				3.11	0.50	0.50	0.25	44
31	NO				4.70	0.57	0.49	0.28	22
31	MSO				5.50	0.65	0.45	0.29	21
41	GW I/II				3.40	0.60	0.48	0.29	47
super-SWIFFR				Λ [km^{-1}]			C_T^*		
30	AW			0.343			0.45	0.28	37
30	NO			0.343			0.49	0.28	44
30	MSO			0.343			0.39	0.28	19
31	AW			0.343			0.50	0.28	70
31	NO			0.343			0.49	0.28	23
31	MSO			0.343			0.45	0.28	23
41	GW I/II			0.343			0.48	0.28	62

4.2 Flight #31

For flight #31 (s.a. Figure 5) of the WIPAFF campaign, the same atmospheric parameters as calculated in the flight evaluation by Platis et al. (2020a) are used: $u_* = 0.29\,\mathrm{m\,s^{-1}}$ and an average free stream velocity of 15.1 m s^{-1} with an easterly wind from 80°. According to the temperature profile, measured in the vicinity of the wind farm cluster, a thermally stable layer was present up to approximately 100 m above sea level (Platis et al., 2020a). The hub height of the turbines of the wind farm cluster is around 90 m, with a rotor diameter of 120 m; thus, the total turbine height reaches 150 m. In this case, with the detected surface layer up to 100 m, the turbines are in the stable layer, but the rotor blades do cut into the neutral layer above (Platis et al., 2020a). During the time span of the measurements the wind farm operated at a capacity between 90–95 %. This results in a very low residual wind velocity at the beginning of the wake, especially visible at the Amrumbank West wind farm (Figure 5a).

4.3 Flight #41

In contrast to the preceding two measurement flights, flight #41 (Figure 6) does not allow an inter-comparison of wind farm wake behaviour for the same atmospheric boundary conditions, since the wind farms Gode Wind I and II are overflown in sequence by the prevailing atmospheric flow. An evaluation of this flight still serves as a comparison of the EFFWAKE and SWIFFR models. Flight #41 took place on October 15 2017 between approximately 12:00 and 16:00 UTC with dominating southerly wind direction (190°) with an average wind speed of 12 m s^{-1}. The thermal gradient indicates a stable stratification from the sea surface up to hub height with half the rotor plane then being in a continuing neutral to slightly stable thermal atmospheric stratification

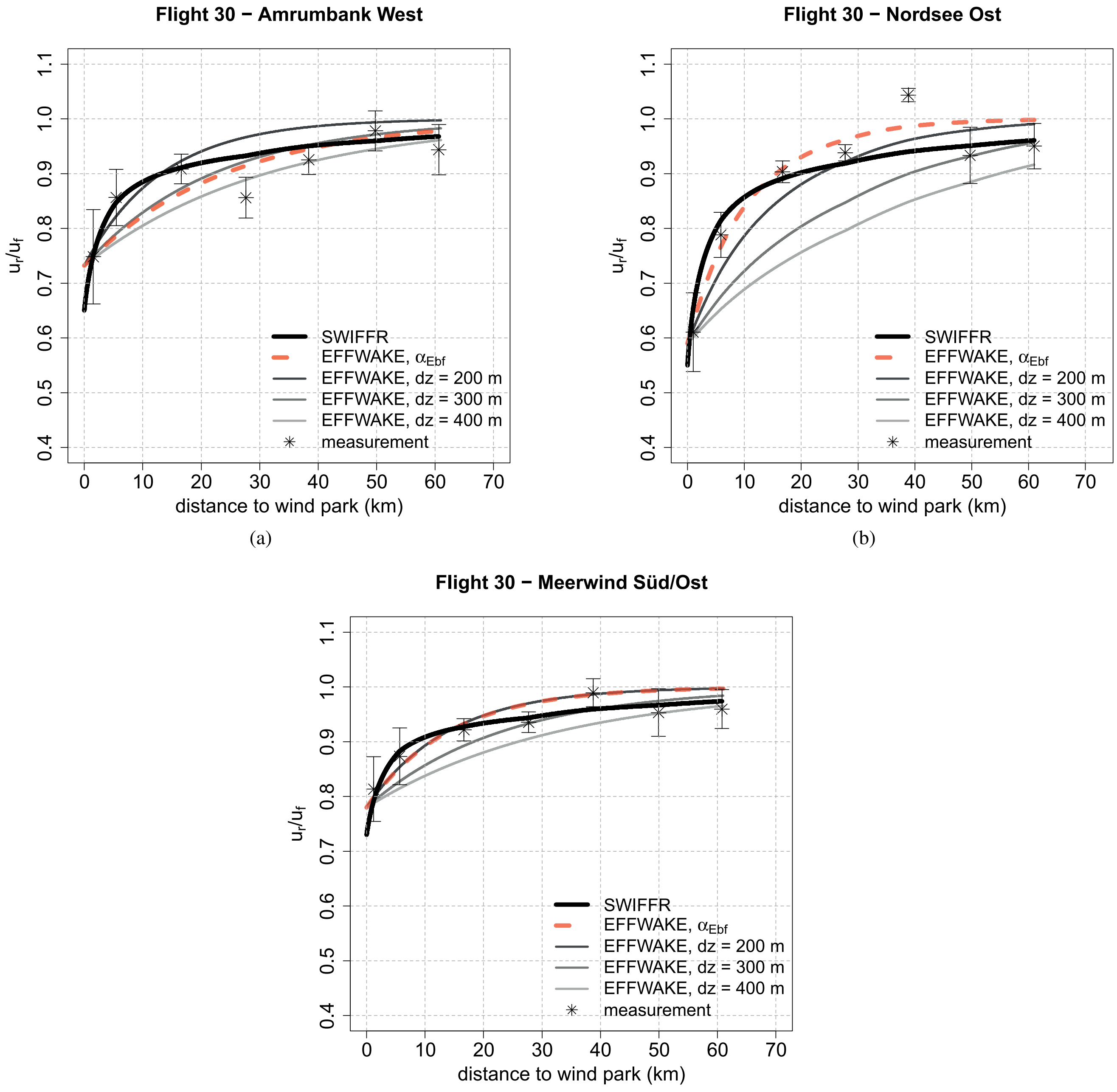

(a)

(b)

(c)

Figure 4: Evaluation of the three wind farm wakes AW (a), NO (b) and MSO (c) for flight #30. Same atmospheric boundary conditions are assumed for all three wakes, due to the vicinity of the three wind farms.

up to a beginning inversion at 400 m. A friction velocity $u_* = 0.21\,\mathrm{m\,s^{-1}}$ has been calculated from FINO 1 data as done by Platis et al. (2020a).

Figure 6a shows two different wind velocities left and right of the wind farm wake. This makes it difficult to define a free flow velocity. Such an uncertainty may impact the model accuracy, and concretely the normalisation of the calculated residual wind speeds.

4.4 Super-SWIFFR derivation

Figure 7 shows the comparison of the Frandsen model, the SWIFFR models as presented in Eq. 2.23 and a fully parametrised version (super-SWIFFR) which derivation is shown below. Observing the results of the Frandsen and SWIFFR solution in Figure 7, both models provide a square-root-shape result and are derived from momentum equations. The respective predictions of the two models coincide, except at Flight #31 – AW. Here, the initial wind deficit is greater than 50 %. To overcome this issue, for this specific wake the Frandsen solution is shifted by 620 m.

The wind farm thrust coefficient C_T^* and wind farm wake widening factor k^* $[\mathrm{m}^{-1}]$ that were used for each wake modelling are shown in each subplot.

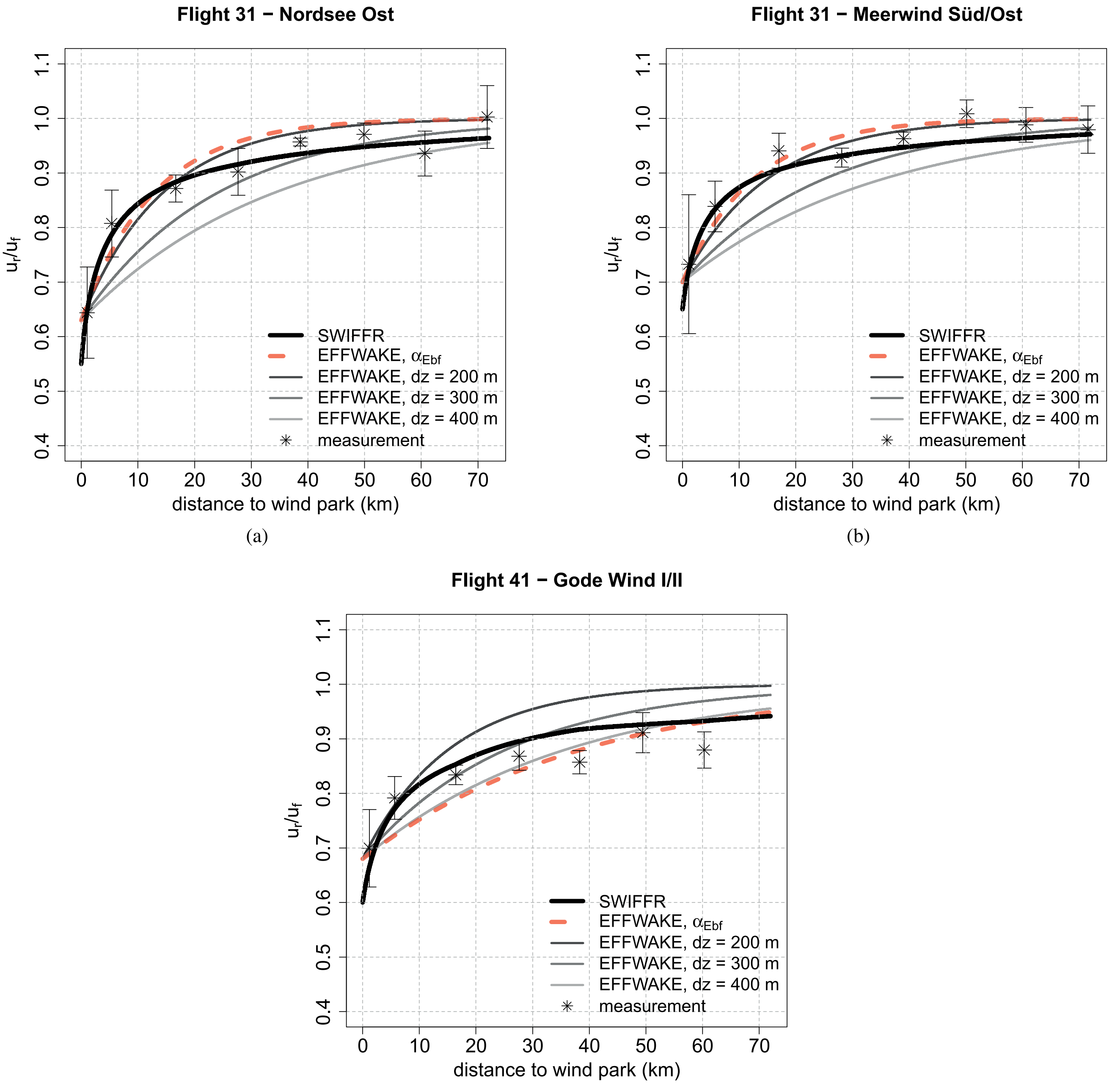

(a) (b) (c)

Figure 5: Evaluation of the three wind farm wakes AW (a), NO (b) and MSO (c) for flight 31.

Considering the overlapping results of the Frandsen and SWIFFR solution, the data can be used to derive an empirical relation between $c|_{x=0}$ and the thrust coefficient C^*_T. Since both parameters negatively correlate (a high thrust coefficient is expected for a low c-value) the product Π(s.a. Table 2) is checked for proportionality, i.e. in its simplest form a constant relationship:

$$\Pi_i = c_i|_{x=0} \cdot C^*_{\mathrm{T}i} = \text{constant} \approx 0.28 \qquad (4.1)$$

With i each of the seven flights and neglecting #31 AW, the average product seems to be nearly constant at $\Pi = 0.28$.

Using this first parametrisation, the modified SWIFFR solution utilising the thrust coefficient derived from the Frandsen solution, can then be calculated using:

$$u_r(x) = \frac{1}{2}\left(\left(\frac{\Pi u_0}{C^*_\mathrm{T}} - \frac{\alpha x}{2}\right) + \sqrt{\left(\frac{\alpha x}{2} - \frac{\Pi u_0}{C^*_\mathrm{T}}\right)^2 + 2u_0\alpha x}\right) \qquad (4.2)$$

For the final simplification, the a priori unknown parameter α is substituted. Therefore, Λ is introduced:

$$\Lambda = \overline{\frac{\alpha_i}{\overline{u}_{fi}}} \approx 0.343. \qquad (4.3)$$

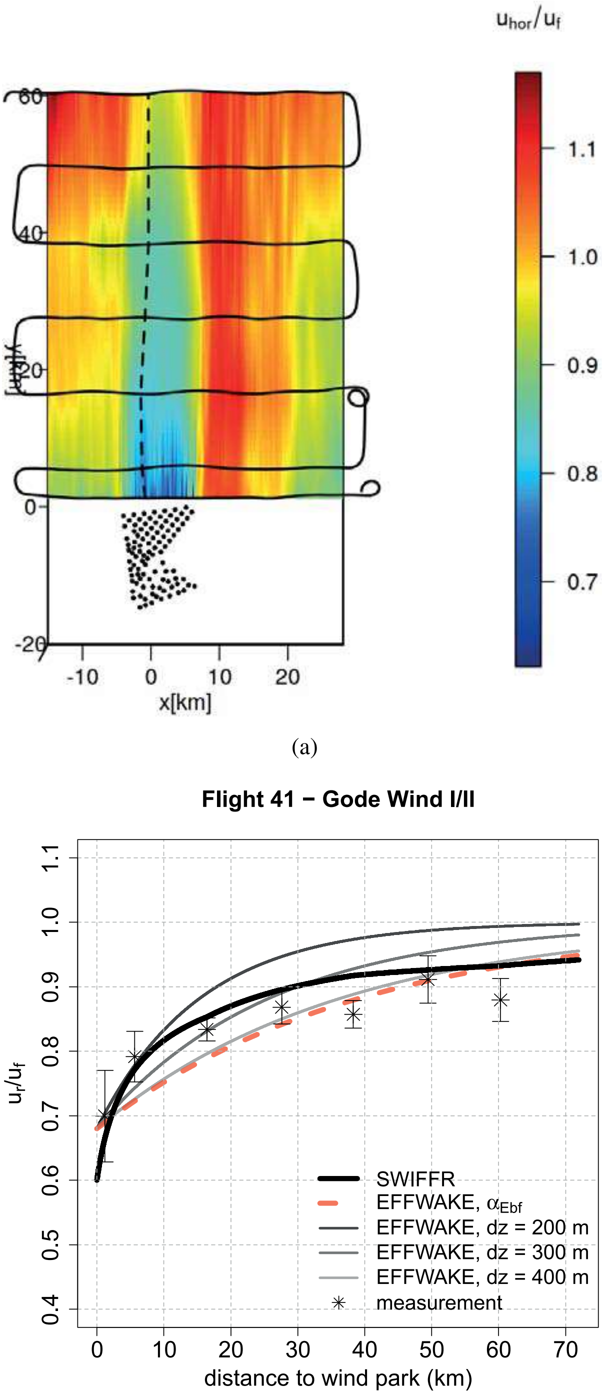

(a)

(b)

Figure 6: Evaluation of the common wake of Gode Wind I and II (flight #41). (a) In-situ wake measurements from the WIPAFF campaign. (b) Comparison of the analytical solutions from EFFWAKE and SWIFFR along the wake-minimum line indicated by the dashed line in (a).

Since Λ is the average of a normalised parameter (excluding GW I/II), its insertion into the final equation needs to be accompanied by a velocity: the free stream velocity at hub height u_f, preferably in front of the wind farm u_0. The super simplified version then becomes:

$$u_r(x) = \frac{1}{2}\left(\left(\frac{\Pi u_0}{C_\mathrm{T}^*} - \frac{\Lambda u_0 x}{2}\right) + \sqrt{\left(\frac{\Lambda u_0 x}{2} - \frac{\Pi u_0}{C_\mathrm{T}^*}\right)^2 + 2u_0^2\Lambda x}\right) \tag{4.4}$$

Dividing by u_0 yields the relative residual wind velocities behind the wake, depending only on the thrust coefficient C_T^*:

$$\frac{u_r(x)}{u_0} = \frac{1}{2}\left(\left(\frac{\Pi}{C_\mathrm{T}^*} - \frac{\Lambda x}{2}\right) + \sqrt{\left(\frac{\Lambda x}{2} - \frac{\Pi}{C_\mathrm{T}^*}\right)^2 + 2\Lambda x}\right) \tag{4.5}$$

A graphical comparison of Eq. 4.5 is given in Figure 7 (blue line). Worth noting is the solution for the GW I/II wind farms that is only about maximum 5 % off, despite using Λ that is 58 % larger than $\frac{\alpha}{u_f}$. The special status of the GW I/II measurements is explained in Section 4.3.

5 Limitations

Emeis (2022) compiled a list of limitations that top-down models still have to battle with. This list consists of the following assumptions:

1. indefinite lateral extent of the wind farms,
2. stationarity,
3. horizontal homogeneity,
4. wind turbines are small compared to the boundary layer height,
5. governing equations from different boundary-layer descriptions fit together,
6. vertical turbulent momentum flux is shear-driven only.

Since the Frandsen model is a bottom-up model and has no intended link to atmospheric boundary conditions, this model will not be regarded in the following assessment.

5.1 Indefinite lateral extent of wind farms

This is an assumption that is made in the EFFWAKE model. The SWIFFR model approach is different and the model is able to incorporate the lateral extent of a wind farm into its turbulent momentum flux parametrisation (s.a. Eq. 2.18). While for large wind farms the effect of lateral momentum flux is negligible, the formalism allows to describe single wind turbine wakes that can be considered 'wind farm' wakes with a lateral extent of one rotor radius R from the wake centre line.

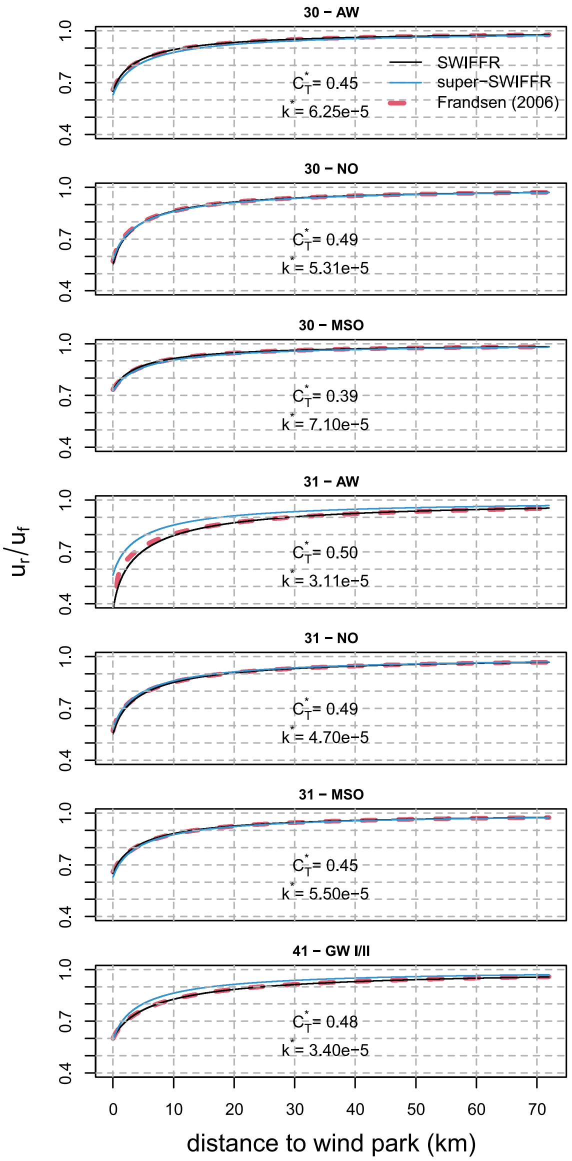

Figure 7: Comparison between the model by Frandsen et al. (2006) and two SWIFFR models; one 'stock' model and one parametrised using dependencies derived from Table 2. While SWIFFR uses a top-down approach, the Frandsen model is a typical representative of a bottom-up model. Despite the difference in their respective derivation, the SWIFFR and Frandsen model predictions coincide, except Flight #31 – AW, where the initial wind deficit is exceeding 50 %.

5.2 Stationarity

EFFWAKE and SWIFFR, both assume steady-state conditions, neglecting synoptic changes and Coriolis effects. Since off-shore atmospheric conditions do not change rapidly, it can be argued that a quasi-non-steady-state solution can be computed using a series of steady-state computations with adjusted input parameters (e.g. mean inflow velocity, friction velocity u_*, wind deficit decay rate α) that resemble the change of the boundary conditions.

5.3 Horizontal homogeneity

The simplified steady-state solutions of analytical models, e.g. the present EFFWAKE and SWIFFR models, are not designed to handle heterogeneities. Any surface patterns that can cause inhomogeneity, like a coast line or a neighbouring wind farm, must not negate the steady-state model assumptions. Therefore, for the model to be applied, the distance to the next surface inhomogeneity should be a manifold of the characteristic length of the wind farm.

Wind turbine spacing is also a factor that influences wind farm efficiency but can not be directly used by the top-down models. Both models describe the recovery of a wind velocity depression, thus EFFWAKE and SWIFFR consider the wind farm and its respective wind turbine spacing as a 'black box'-momentum sink.

5.4 Wind turbine height compared to surface layer height

In the course of the models derivations some assumptions about the vertical wind profiles are made. On the one hand the top-down models assume the hub height of the wind turbines to be at the edge of the surface or Prandtl layer (requirement for Eq. 2.6 to be valid). On the other hand, it is assumed that the mean wind velocity does not further increase above hub height nor decrease significantly below $h - R$. With increasing wind turbine heights in the future, the validity of these assumptions needs to be evaluated.

5.5 Governing equations from different boundary-layer descriptions fit together

See above.

5.6 Shear-driven vertical turbulent momentum flux

Emeis (2022) summarises the following: Generally, the friction velocity is linked to vertical wind shear when closing the full set of equations of motion. This means that vertical profile laws and also the geostrophic drag law, which involve the friction velocity, are based on the presence and dominance of shear-driven turbulence, which in turn is responsible for vertical turbulent momentum fluxes. This assumption leads to problems in strongly stable conditions where well-defined turbulence is no longer present, and in strongly unstable conditions where thermally driven turbulence dominates the shear-driven turbulence (see, e.g., Stull (1988)).

However, both presented analytical top-down models are capable of mapping very long wind farm wakes, typically found in very stable conditions.

6 Discussion and conclusions

Provided the EFFWAKE and SWIFFR models both use the same atmospheric input parameters (u_*, u_f) the newly proposed SWIFFR model can stand out with an easy to determine analytical fit for given atmospheric conditions. The major disadvantage of the EFFWAKE model is the dependency of a precise Δz, which is usually impossible to determine. Also Δz is a parameter that is a function of turbine spacing and atmospheric conditions, since it is essentially the height of the internal boundary layer above a wind farm.

The SWIFFR model gives a good prediction with less unknown variables, derived from the flow-governing equations (top-down approach). The initial conditions need to be known for both models and can be calculated using established bottom-up engineering models. These bottom-up models formulate the wake-governing equation starting from the behaviour of a single wind energy turbine, usually modelled as a rotating disk. Alternatively to calculating initial conditions, empirical values can be used for a quick assessment. Or, as for the validation of this model in this study, measured data can be used. In practice, this could be sonic anemometers on top of wind turbines or, maybe the better choice, forward looking lidar measurements on top of wind turbines scanning the inflow and the wake. This means that the SWIFFR model, for a distinct wind deficit, computes a development of the wind recovery, based on relatively easy to obtain parameters: the (average) radius of the rotor plane R of the wind turbines in the wind farm, the friction velocity u_* and the mean wind speed u_0 or, if applicable, $u_f(x)$ at hub height. Additionally, it was shown that the SWIFFR model can be altered to use a wind farm thrust coefficient C_T as an input variable, making the model independent of initial wake deficit measurements. For this study the thrust coefficients determined by the well established Frandsen model have been used. The constant $\overline{\Pi} \approx 0.28$ is expected to be independent of atmospheric stability, since it is derived from the initial wind farm wake deficit that we consider independent of thermal stratification. Equation 4.2 represents the first simplification of the SWIFFR model by removing c from the equation. The next and final simplification consists of embedding an average, normalised wind deficit decay rate Λ. For the present cases the gained simplification is worth the small loss of accuracy. Λ indirectly contains informations like atmospheric stability, friction velocity u_* and wind turbine spacing. Thus, Λ is not to be understood as a value that will work in all circumstances, and should be further investigated. But Table 2 and Figure 7 suggest that a variation of $\Lambda \pm 10\,\%$ still provides solutions with acceptable RMSDs for a fairly wide range of u_* values.

Table 2 shows that the SWIFFR model uses roughly identical wind deficit decay rates α for the different wind parks for the evaluated flights. They only differ slightly due to the f-parameter, a parameter which is given by the wind farm geometry. This behaviour is expected, since we argue that the wind deficit decay rate is largely depending on the atmospheric boundary conditions (stability and mean incoming wind velocity) which are the same for the wind farms AW, NO, and MSO in flight #30 and again for flight #31, respectively, since the three wind parks are clustered together. Thus, Table 2 indicates that the wind deficit decay rates α mostly change with the friction velocity u_* or a change in the mean flow velocity u_0 at the inflow. The normalised wind deficit decay rate $\alpha/\overline{u}_f$ suggests a correlation to the incoming mean flow velocity. In simple terms, $\alpha/\overline{u}_f$ is a measure of turbulent influx per wind velocity (e.g. at the inlet). Mathematically, u_* directly influences α. Physically, higher wind velocities may also lead to higher shear stress above/around a wind farm and therefore also impact α. At the latest, when normalising α and yielding Λ.

Also note, that the SWIFFR model was not stability corrected, i.e. no z/L-correction as in Eq. 2.6 was implemented, at this point of the data evaluation. Using the measured values for u_* and u_0 (or $u_f(x)$) was sufficient for the SWIFFR model to fit to the wind farm wake measurements. Thus, it is hard to argue which parameter is the dominating factor defining the behaviour of α, having only the available data (s.a. Table 2). The super-SWIFFR solution uses Λ, a parameter that incorporates stability affected behaviour of the wake. But to proof this, further studies and more data is needed.

Regarding the model accuracy, both models provide a similar accuracy, considering the EFFWAKE best fit. However, the EFFWAKE best fit can only be modelled to the data, there is no possible way of knowing Δz for the different wind parks in different atmospheric conditions, also illustrated in Figure 4-6. See also the varying Δz_bf in Table 2 for the different wind parks, yet the same atmospheric conditions. Well pictured in Figure 5, where the best corresponding best fit Δz values are approximately halved when the wind farms AW and NO are compared. Thus, Δz might be considered more a geometrically influenced parameter. At this point, the EFFWAKE model lacks in terms of a prediction model, since there is no source on how to choose Δz for different wind farm configurations.

The SWIFFR model is additionally compared to the Frandsen model that is used to calculate the wind deficit behind a single wind turbine, but is also used to calculate the wind deficit behind wind farms. Both square-root-shape models are derived from momentum conservation equations. Also, both models use at least one parameter that is not easily calculated: the wake widening coefficient k or k^* in the Frandsen model and the wind deficit decay rate α in the SWIFFR model. Despite the difference in their respective derivation, both models generally coincide and predict identical wake lengths. This indicates that the SWIFFR model can be used to determine and predict wind farm wake lengths in a similar way as the Frandsen model. It simply uses other input parameters. In contrast to the wind farm (wake) properties that are used as inputs in the Frandsen model, the SWIFFR model uses atmospheric flow properties. Therefore, the SWIFFR model has the potential to be used for wind and weather forecasting, i.e. for computations whenever effects of changing atmospheric conditions are of interest.

7 Outlook

The EFFWAKE and SWIFFR model provide a quick and simple way to model a wind-farm wake using only few input parameters. In the presented cases the SWIFFR model can give a prediction of the wake length, whereas the EFFWAKE model only works applying a best fit to observational data, since Δz is a priori unknown. The obtained accuracy from the beginning of the wake till the end of the wake is more or less comparable (according to the RMSD). Yet, the SWIFFR model solely provides an actual prediction of the wind-farm wakes, so does the Frandsen model. While the latter model uses wind turbine properties to describe the wake, the SWIFFR model relies on atmosphere-related parameters. Thus, the SWIFFR model is suited for weather forecasting models that already utilise the friction velocity and mean wind speed. The super-SWIFFR altercation of the model expands the model applicability further by providing a possibility to use the model with a common wind farm modelling parameter (only), the thrust coefficient C_T. Thus, Eq. 4.5 combines an element of a bottom-up approach (thrust coefficient), and through the parametrisation of atmospheric data, elements of a top-down approach (u_*, u_0, K_m). To further specify the parameters Λ and Π more studies are necessary, especially in different atmospheric thermal stabilities present.

The ease of use of the super-SWIFFR model would increase tremendously, should future investigations and data evaluations show, that the wind deficit decay rate α correlates sufficiently with the incoming mean wind velocity and a credible Λ could be retrieved. Therefore, we need reliable atmospheric measurements also to derive stability parameters for further investigations of the atmospheric thermal stability relation. Such data sets would also provide an opportunity to revisit a comparison of the SWIFFR and EFFWAKE model, since it would allow further investigations into the Δz parameter of the EFFWAKE model.

So far this model assessment is only valid with no significant inversion present. With ever-increasing wind turbine dimensions, both models need to be eventually adjusted due to this development.

Authorcontribution

Moritz Mauz derived the model formalism and the equations and evaluated the data. Frederick Höckh provided the sets of processed WIPAFF data. Bram van Kesteren contributed to the formalism. Andreas Platis, Stefan Emeis and Jens Bange added to the general discussion of the topic and added valuable input to shape this study.

Acknowledgments

The project WIPAFF was funded by the German Federal Ministry for Economic Affairs and Energy (Bundesministerium für Wirtschaft und Energie) on the basis of a decision by the German Bundestag grant number: FKZ 0325783

This open-access publication was funded by the University of Tübingen.

References

Andersen, S., J. Sørensen, S. Ivanell, R. Mikkelsen, 2014: Comparison of engineering wake models with CFD simulations. – J. Phys. Conf. Ser. **524**, 012161, 10.1088/1742-6596/524/1/012161. Content from this work may be used under the terms of the Creative Commons Attribution 3.0 licence. Any further distribution of this work must maintain attribution to the author(s) and the title of the work, journal citation and DOI. – Published under licence by IOP Publishing Ltd; 5th International Conference on The Science of Making Torque from Wind 2014, TORQUE 2014.

Antonini, E.G., K. Caldeira, 2021: Atmospheric pressure gradients and coriolis forces provide geophysical limits to power density of large wind farms. – Appl. Energy **281**, 116048, DOI: 10.1016/j.apenergy.2020.116048.

Bärfuss, K., R. Hankers, M. Bitter, T. Feuerle, H. Schulz, T. Rausch, A. Platis, J. Bange, A. Lampert, 2019: In-situ airborne measurements of atmospheric and sea surface parameters related to offshore wind parks in the German Bight. – PANGAEA, published online, https://doi.pangaea.de/10.1594/PANGAEA.902845.

Betz, A., 1920: Das maximum der theoretisch möglichen ausnützung des windes durch windmotoren. – Z. gesamte Turbinenwesen **26**, 307–309.

Businger, J.A., J.C. Wyngaard, Y. Izumi, E.F. Bradley, 1971: Flux-profile relationships in the atmospheric surface layer. – J. Atmos. Sci. **28**, 181–189, DOI: 10.1175/1520-0469(1971)028<0181:FPRITA>2.0.CO;2.

Canadillas, B., R. Foreman, V. Barth, S. Siedersleben, A. Lampert, A. Platis, B. Djath, J. Schulz-Stellenfleth, J. Bange, S. Emeis, T. Neumann, 2020: Offshore wind farm wake recovery: Airborne measurements and its representation in engineering models. – Wind Energy **23**, DOI: 10.1002/we.2484.

Djath, B., J. Schulz-Stellenfleth, B. Canadillas, 2018: Impact of atmospheric stability on x-band and c-band synthetic aperture radar imagery of offshore windpark wakes. – J. Renew. Sustain. Energy **10**, 043301, DOI: 10.1063/1.5020437.

Emeis, S., 2010: A simple analytical wind park model considering atmospheric stability. – Wind Energy **13**, 459–469, DOI: 10.1002/we.367.

Emeis, S., 2017: Wind Energy Meteorology. – Springer, Heidelberg, Germany, 144–146.

Emeis, S., 2022: Analysis of some major limitations of analytical top-down wind-farm models. – Bound.-Layer Meteor. **187**, 423–435, DOI: 10.1007/s10546-021-00684-4.

Emeis, S., S. Siedersleben, A. Lampert, A. Platis, J. Bange, B. Djath, J. Schulz-Stellenfleth, T. Neumann, 2016: Exploring the wakes of large offshore wind farms. – J. Phys. Conf. Ser. **753**, 092014, DOI: 10.1088/1742-6596/753/9/092014.

Frandsen, S., R. Barthelmie, S. Pryor, O. Rathmann, S. Larsen, J. Højstrup, M. Thøgersen, 2006: Analytical modelling of wind speed deficit in large offshore wind farms. – Wind Energy **9**, 39–53, DOI: 10.1002/we.189.

Garratt, J., 1994a: The Atmospheric Boundary Layer. – Cambridge Atmospheric and Space Science Series. – Cambridge University Press.

Garratt, J., 1994b: Review: the atmospheric boundary layer. – Earth-Sci. Rev. **37**, 89–134, DOI: 10.1016/0012-8252(94)90026-4.

Garratt, J.R., 1987: The stably stratified internal boundary layer for steady and diurnally varying offshore flow. – Bound.-Layer Meteor. **38**, 369–394, DOI: 10.1007/BF00120853.

Hanna, S.R., 1987: An empirical formula for the height of the coastal internal boundary layer. – Bound.-Layer Meteor. **40**, 205–207, DOI: 10.1007/BF00140077.

Hassan, G., Partners Ltd., 2014: Windfarmer tutorial: Introduction to windfarmer. – Technical report.

Jensen, N., 1983: A note on wind generator interaction Number 2411 in Risø-M. – Risø National Laboratory.

Katić, I., J. Højstrup, N.O. Jensen, 1987: A simple model for cluster efficiency. – In: Palz, W., E. Sesto (Eds), EWEC'86, Proceedings. Vol. 1, 407–410).

Lampert, A., K.B. Bärfuss, A. Platis, S.K. Siedersleben, B. Djath, B. Cañadillas, R. Hankers, M. Bitter, T. Feuerle, H. Schulz, T. Rausch, M. Angermann, A. Schwithal, J. Bange, J. Schulz-Stellenfleth, T. Neumann, S. Emeis, 2020: In-situ airborne measurements of atmospheric and sea surface parameters related to offshore wind parks in the German Bight. – ESSD **12**, 935–946.

McKay, P., R. Carriveau, D.S.T. Ting, T. Newson, 2012: Turbine Wake Dynamics. – IntechOpen, 10 Lower Thames Street, London, EC3R 6AF, UK.

Meyers, J., C. Meneveau, 2012: Optimal turbine spacing in fully developed wind farm boundary layers. – Wind Energy **15**, 305–317, DOI: 10.1002/we.469.

Niayifar, A., F. Porté-Agel, 2016: Analytical modeling of wind farms: A new approach for power prediction. – Energies **9**, 741, DOI: 10.3390/en9090741.

Platis, A., S.K. Siedersleben, J. Bange, A. Lampert, K. Bärfuss, R. Hankers, B. Canadillas, R. Foreman, J. Schulz-Stellenfleth, B. Djath, T. Neumann, S. Emeis, 2018: First in situ evidence of wakes in the far field behind offshore wind farms. – Scientific Reports **8**, 2163, DOI: 10.1038/s41598-018-20389-y.

Platis, A., M. Hundhausen, M. Mauz, S. Siedersleben, A. Lampert, K. Bärfuss, B. Djath, J. Schulz-Stellenfleth, B. Canadillas, T. Neumann, S. Emeis, J. Bange, 2020a: Evaluation of a simple analytical model for offshore wind farm wake recovery by in situ data and weather research and forecasting simulations. – Wind Energy **24**, 212–228, DOI: 10.1002/we.2568.

Platis, A., J. Bange, K. Bärfuss, B. Canadillas, M. Hundhausen, B. Djath, A. Lampert, J. Schulz-Stellenfleth, S. Siedersleben, T. Neumann, S. Emeis, 2020b: Long-range modifications of the wind field by offshore wind parks – results of the project WIPAFF. – Meteorol. Z. **29**, 355–376, DOI: 10.1127/metz/2020/1023.

Prandtl, L., 1904: über flüssigkeitsbewegung bei sehr kleiner Reibung. – Verhandlungen des III. Intern. Math. Kongr. Heidelberg. –Gesammelte Abhandlungen **2**, 484–491.

Siedersleben, S.K., A. Platis, J.K. Lundquist, A. Lampert, K. Bärfuss, B. Cañadillas, B. Djath, J. Schulz-Stellenfleth, J. Bange, T. Neumann, S. Emeis, 2018: Evaluation of a wind farm parametrization for mesoscale atmospheric flow models with aircraft measurements. – Meteorol. Z.**27**, 401–415, DOI: 10.1127/metz/2018/0900.

Stull, R.B., 1988: An introduction to boundary layer meteorology. – Kluwer Academic Publishers, Dordrecht, the Netherlands.

Yang, X., S. Kang, F. Sotiropoulos, 2012: Computational study and modeling of turbine spacing effects in infinite aligned wind farms. – Phys. Fluids **24**, 115107, DOI: 10.1063/1.4767727.

Zhan, L., S. Letizia, G. Valerio Iungo, 2020: Lidar measurements for an onshore wind farm: Wake variability for different incoming wind speeds and atmospheric stability regimes. – Wind Energy **23**, 501–527, DOI: 10.1002/we.2430.

A.3 Miniature high-frequency chilled-mirror hygrometer for atmospheric measurements aboard fixed-wing UAS

Meteorol. Z. (Contrib. Atm. Sci.), Vol. **29**, No. 6, 439–449 (published online July 17, 2020)

Measurement Techniques

Miniature high-frequency chilled-mirror hygrometer for atmospheric measurements aboard fixed wing UAS

Moritz Mauz[1]*, Bram van Kesteren[1], Wolfgang Junkermann[2], Kjell zum Berge[1], Martin Schön[1], Andreas Platis[1] and Jens Bange[1]

[1]Centre for Applied Geoscience, University of Tübingen, Germany
[2]Institute for Meteorology and Climate Research, Karlsruhe Institute of Technology, Garmisch-Partenkirchen, Germany

(Manuscript received January 2, 2020; in revised form April 30, 2020; accepted April 30, 2020)

Abstract

A small light-weight in-house made miniature chilled-mirror hygrometer (CMH) for fixed wing UAS (unmanned aircraft system) is presented, with its features and limitations. Therefore, first measurements of the CMH equipped on the small research UAS of type MASC-3 (multi-purpose airborne sensor carrier) operated by the University of Tübingen are shown. A comparison against a very accurate state of the art capacitive industrial humidity sensor (SHT31) is done. The sensor consists of a TEC (thermoelectric cooler) covered by a gold mirror. The TEC is controlled by a commercially available microprocessor with an on-board PID (proportional-integral-derivative) controller. The results of the CMH measurements are in good agreement with the industrial-made capacitive sensor. The absolute accuracy of the measured dew point temperature by the CMH is in the range of ±0.2 K. Spectra show evidence that the CMH is capable to measure turbulent humidity fluctuations in the atmosphere with a temporal resolution of up to 10 Hz. Such a fast humidity sensor aboard a small UAS has the potential to study humidity fluxes in the surface layer over complex terrain, behind wind energy converters and humidity variations over land and sea surfaces in general.

Keywords: Chilled mirror hygrometer, Unmanned Aircraft System, high frequency humidity measurement, Boundary Layer Measurements

1 Introduction

Together with temperature, pressure, and the 3D wind vector, water vapour is a key parameter to describe the state of the atmosphere. Water vapour is the most important greenhouse gas on Earth and plays an important role in energy transfer through the atmosphere because of its heat capacity. Furthermore, evapotranspiration of water at the surface contributes substantially to the energy budget at the Earth surface, due to the high enthalpy of evaporation. Because of its low molar mass, moisture increases the buoyancy of air and thus affects atmospheric stability, especially over sea surfaces and vegetated soils (Koufang Lo, 1996; Stull, 2000). The water vapour transport into the atmosphere is essentially turbulent; and as such, water vapor fluxes are one of the key observational parameters in established monitoring networks like FLUXNET (Baldocchi et al., 2001), TERENO (Bogena et al., 2015), ICOS (Rebmann et al., 2018) and NEON (neonscience.org, 2019) and several large field campaigns in complex terrain, e.g. Scalex (Wolf et al., 2017) and LITFASS (Beyrich et al., 2002b; Beyrich et al., 2002a; Beyrich et al., 2006).

Fast-response humidity sensors that can capture the relevant turbulence time-scales are open- or closed-path optical absorption techniques, such as Lyman alpha, TDL (tunable diode laser) or IR (infrared) absorption. These sensors can accurately determine the variance, the structure parameter, or other relevant turbulent humidity parameters (De Bruin et al., 1993). In combination with fast-response anemometers, these point-source measurements additionally allow for accurate estimates of the humidity flux on times scales of 15–30 min (Shuttleworth, 2007). In combination with laser scintillometers, sampling time of humidity fluxes can be reduced to 1 min under homogeneous conditions (Van Kesteren et al., 2013a; Van Kesteren et al., 2013b). However, the above presented methods are impossible to implement on mobile platforms and only represent small geographic areas, which especially in heterogeneous conditions limits their applicability as a reference in e.g. numerical models or water-balance estimates (Foken, 2008). Microwave scintillometers allow for determining the structure parameter of humidity, or in combination with a large aperture scintillometer also fluxes, under heterogeneous conditions over scales of up to 10 km (Meijninger et al., 2006; Ward et al., 2015a; Ward et al., 2015b). But scintillometers only provide an average quantity over the length of the measurement path.

Alternatively, Lyman-alpha and infrared absorption hygrometers can be installed on helipod (pod of me-

---

*Corresponding author: Moritz Mauz, Centre for Applied Geoscience, University of Tübingen, Hölderlinstr. 12, 72074 Tübingen, Germany, e-mail: moritz.mauz@uni-tuebingen.de

DOI 10.1127/metz/2020/1026
Gebrüder Borntraeger Science Publishers, Stuttgart, www.borntraeger-cramer.com

teorological equipment dragged by a helicopter) or manned aircraft to obtain spatial information on the turbulent exchange of humidity, e.g. (Platis et al., 2017; Lampert et al., 2018; Bange and Roth, 1999; Muschinski et al., 2001). However, these airborne systems are expensive and limited in their mobility by aviation laws. Manned aircraft are typically restricted to flight altitudes of approximately 150 m above ground, and special permissions are required for lower flight altitudes. In some occasions lower altitudes down to 25 m have been reported using small environmental research aircraft (SERAs) (Metzger et al., 2011; Neininger and Hacker, 2012). Recent technical developments in drone technique led to an increased application of cheap, light-weight unmanned aerial systems (Spiess et al., 2007; van den Kroonenberg et al., 2012; Rautenberg et al., 2019). However, so far suitable fast response-humidity sensors have not been available.

For (small) unmanned aircraft systems (UAS), the weight of a measuring instrument is an important factor. Instruments that work well on a manned aircraft or helipods typically weigh more than 2 kg, which exceeds the payload for these small aircraft. Low weight capacitive moisture sensors, which are typically installed on meteorological towers (Kuner et al., 2015), are light enough; but their response time is smaller than 1 Hz. As such, these sensors are not fast enough to capture the relevant turbulent scales. Wildmann et al. (2014a) attempted to increase the response time of a capacitive sensor by post-processing the humidity data, while implying an inverse model. This method allows to obtain humidity data up to 3 Hz. However, despite careful calibration, data accuracy suffers because of an increased noise level, which in practice makes the method unsuitable.

An alternative to capacitive sensors are lightweigth dew point mirrors or chilled-mirror hygrometers (CMHs). Their measurement principle is based on cooling the surface of a small mirror until condensation occurs, while monitoring its temperature. With a properly designed feedback system, the mirror is maintained at the temperature at which the rate of condensation equals the rate of dew evaporation. In this state, the condensed water is in equilibrium with the water vapour pressure of the surrounding air, thus defining the dew point temperature (Stull, 2000). This kind of dew point sensors are applied in radiosondes, where they measure moisture with a measurement frequency of up to 1 Hz (Vömel et al., 2003). Comparison and evaluation of a commercial chilled-mirror hygrometer to a capacitive sensor (Humicap) show that this type of sensor performs well, even for the challenging radiosonde application (Fujiwara et al., 2003). Unfortunately, commercial sensors still lack the temporal resolution required for accurate turbulent humidity measurements.

In this work, an approach for doing accurate high-frequency measurements of water vapour is presented that can capture the smallest turbulent time scales. The goal of such a sensor is to be able to study the underlying processes related to water vapour fluctuations and water vapour transport in the lower atmosphere. To this end, a small chilled-mirror hygrometer is tuned to allow for a high-frequency output and mounted it on a small UAS, the MASC-3, that operates in the lower parts of the atmospheric boundary layer (in this study up to about 200 m) (Rautenberg et al., 2019). The hygrometer performance is compared against capacitive humidity sensors mounted on a meteorological observation tower and a capacitive sensor mounted on the UAS. As we will show, our tuned hygrometer provides a high measurement frequency (>5 Hz) with a minimal need of maintenance.

2 Setting-up the chilled-mirror hygrometer

A chilled-mirror hygrometer (CMH) measures the dew point temperature of the air that ventilates it. By cooling the polished metallic surface of the mirror, water condenses on its surface and this dew causes a strong signal change on the luminosity sensor that monitors the brightness of the mirror. Consequently, the crucial parts are: a temperature sensor, a thermoelectric cooler (TEC) controller that regulates the temperature of the surface that is measured and a high frequency luminosity sensor. The heat capacity of the golden mirror is also a critical parameter. Of course, the heat capacity of the golden mirror can be calculated and the mirror should be as thin as possible, yet, this delaying parameter is only available implicitly. To circumvent this problem, only small currents are applied to the TEC, so that an equilibrium between the inflow of the air that reheats the mirror and the current that cools the mirror, is achieved.

Our humidity sensor is made from commercially available parts (cf. Table 1). Figure 1 shows a schematic of the hygrometer and its components. Basically, a light-sensitive diode (the luminosity sensor) measures the reflection of light emitted by a light-emitting diode (LED) from the mirror. Increasing dew accumulation on the mirror decreases the direct reflection into the luminosity sensor, whereas the amount of diffusely scattered light is increased. The proportional-integral-derivative (PID) controller regulates the voltage output to the TEC (values between 0–4.5 V), ensuring a constant reflected light level. In default mode the TEC surface is actively cooled, whereas the thermal energy of the inflowing air is used to heat the mirror. In our airborne application, ventilation is achieved by using the dynamic air pressure at the inlet (ram air), channelled to the measurement chamber onto the TEC reflective surface. At a typical true air speed of 18.5 $\mathrm{m\,s^{-1}}$ (speed relative to the air), a calculated volumetric flow of $\approx 0.27\,\mathrm{l\,min^{-1}}$ is achieved through the inlet (aperture 0.25 $\mathrm{mm^2}$).

2.1 Specifications

The Arduino Nano has a CPU (central processing unit) clocking speed of 16 MHz. This is enough to provide

Table 1: Various parts of the in-house built CMH. * Component from a Snow White® CMH from Meteolabor AG

Function	Component
Light source	white LED
Luminosity sensor	Adafruit TSL2561
Temperature measurement	TC type T *
Temperature read-out	Adafruit MAX31856
Microcontroller	Arduino Nano
Thermo-electric cooling	≈2.5 W *

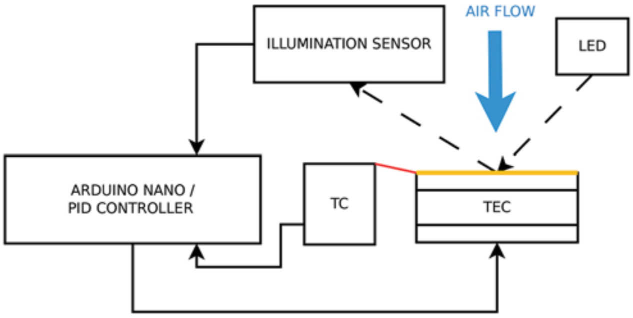

Figure 1: Schematic of the CMH mode of operation. The CMH consists of commercially available parts, e.g. the microprocessor (Arduino Nano) that, among other routines, hosts the PID controller that regulates the voltage output to the thermoelectric cooler (TEC). The golden layer on the TEC is the mirror that is in direct contact with the inflowing air. The thermocouple (TC) thermometer measures the mirror temperature.

a logging speed of 52 Hz, causing one measurement cycle to be about 19 ms long. Consequently, the integration time for the PID controller is also 19 ms. The temperature measurement (TC) is sensor-wise digitally limited to roughly 12 Hz, which correspondingly is the theoretical maximum attainable output-frequency of our hygrometer.

The light source of the sensor is a white LED supplied with a constant voltage stabilised by a Z-diode. The PID controller is set to hold a fixed illumination which is equivalent to the dew point criterion on the TEC surface. For this prototype, the target illumination is 1150 lux. An advantage of the PID controller is that the voltage sent to the TEC to cool the mirror is not only proportional to the illumination signal, but also takes into account an integral term that is proportional to both the magnitude of the error and the duration of the error (time the signal is off the set-point) as well as the derivative representing the past rate of cooling.

Here, the error is the deviation of the current illumination level from the target value (also called the set point). This kind of cooling regulation minimises overmodulation or forced oscillations that result from operation of on/off controllers or simple P (proportional) controllers (Narvekar and Upadhye, 2016). A PID controller is recommended when dealing with higher order capacitive processes (Rao and Mishra, 2014).

A long-term drift, as in open-path humidity sensors (Mammarella et al., 2009), does not occur in chilled-mirror humidity sensors. Also LED ageing (fading) is not a concern. Typically LEDs fade to a value of 98 % of their initial luminosity after 2000–6000 operating hours. Similar values can be assumed for the illumination detection diode. However, a potential source of error is contamination of the mirror surface by any pollutant transported in the air that may condense or adhere to it. Regular inspection and cleaning of the surface, when polluted, e.g. by pollen, will prevent erroneous measurements. Furthermore, due to the high performance of the TEC, an appropriate heat sink is required. In our airborne application, the heat sink is exposed to the air flow along the fuselage of the UAS, providing sufficient heat release.

2.2 Calibration of the CMH

A dew point sensor does not need a calibration like for example a resistance thermometer (e.g. five point calibration). However, for each sensor it is necessary to define a dew point criterion, i.e. target illumination for the illumination sensor. This target illumination was found by operating the chilled-mirror hygrometer next to the SHT31 sensor in a small wind tunnel. The wind tunnel provides a steady stream of air, with laminar flow at a constant humidity. Correct tuning of the target illumination is achieved when the dew point measurement of the chilled-mirror hygrometer matches that of the SHT31. This procedure does not assure absolute accuracy of the chilled-mirror sensor, but provides a good estimate for the necessary target illumination.

A small offset between both sensors has been found to yield the fastest response time for our sensor. This bias corresponds to an undercut of the target illumination. Undercutting the illumination helps stabilising the PID controller, i.e. minimising over-regulation, by providing a stable layer of dew on the mirror.

3 Measurement system and measurement site for data comparison

3.1 Research UAS

The research UAS MASC-3 (multi-purpose airborne sensor carrier) (see Figure 2 and Table 2) is a fixed wing airborne measurement system designed and operated by the University of Tübingen (Wildmann et al., 2013; Wildmann et al., 2014b; Wildmann et al., 2014a; Wildmann et al., 2014c). Depending on payload and batteries, it has a take-off weight between 5 and 8 kg and the UAS has an endurance between 1.5 and 2 hours. To reduce disturbance introduced by the air of the MASC-3's propeller and engine; a pusher configuration was selected, i.e. the propulsion system is located at the back of the aircraft. For automatic

Figure 2: MASC-3 UAS shortly after take-off. The winch cable is still attached to the fuselage. Photo taken at the ISOBAR campaign 2018, courtesy Astrid Lampert

Table 2: System characteristics of the MASC-3 UAS at a usual measurement campaign.

wingspan	4 m
total weight	≈7 kg
sci. payload	≈1 kg
cruising speed	19 m s^{-1}
endurance	up to 2.5 h
propulsion	electrical pusher engine
take-off	bungee or winch

flight control, it uses a Pixhawk 2.1 "Cube" autopilot (Pixhawk-Organisation, 2019) to follow waypoints defined by the ground station operator at a constant airspeed typically around 18 m s^{-1}.

The MASC-3 system allows in-situ high-frequency measurements of the atmospheric flow (pressure) using a five-hole probe and air temperature using a fine wire platin resistance thermometer, thus it is able to resolve turbulent structures at very small scale (Mauz et al., 2019). All measured data is stored using a logging frequency of 500 Hz. After post-processing all data are scaled and available in 100 Hz. Additionally to atmospheric parameters the necessary GPS positioning and orientation angles and angular accelerations are logged by an IMU (inertial measurement unit). A detailed description of the UAS and its instrumentation can be found in Rautenberg et al. (2019). The chilled-mirror high-frequency humidity sensor has been implemented into the sensor system of the MASC-3 and can be post-processed in the same manner as all on-board sensors. The sensor weighs approximately 200 g and the hardware is in a 92 mm × 60 mm × 30 mm (L×W×H) box (cf. Figure 3).

3.2 Data for comparison and measurement site

In order to test and evaluate the system, a measurement flight took place at the WINSENT wind-energy test site at the Swabian Alb near the town of Donzdorf, Germany. The aim of the WINSENT project is to evaluate the local wind field, and to investigate orographical induced turbulence, and the stress it induces on wind energy converter blades, caused by the transition from a plateau to low lands by a steep escarpment of about 200 m height. The site is still in preparation, and two wind energy converters (WECs) will be installed until autumn 2020. At present, a 100 m tall meteorological tower (location 48.6652 N, 9.8348 E) is installed on the plateau, directly behind the forested escarpment. The tower (Figure 4) has a lateral distance of 80 m to the escarpment. On the tower, meteorological parameters are measured at several heights. To minimize the impact of the tower structure on the measurements for the predominant westerly as well as easterly winds, all sensors are installed on horizontal booms of 1 to 3 m length extending towards north and south.

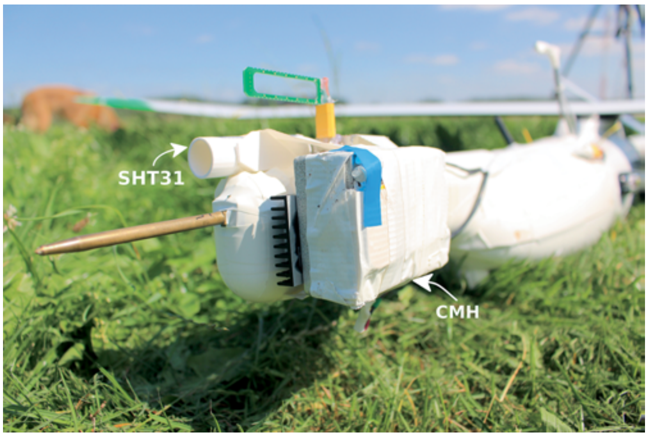

Figure 3: Sensor dome of the research UAS MASC-3 shortly before take-off, holding the five-hole probe (brass tube), CMH with radiator (white box with blue stripe) and SHT31 thermo- and hygrometer (inside the white radiation shield). The green bracket is holding a fine wire platinum resistance thermometer.

The MASC-3 measurements are captured in so-called 'flight legs'. A leg is the straight and level section of a UAS flight pattern (see logged flight path in Figure 5).

The UAS captured data starting at 20 m a.g.l up to 140 m a.g.l in 20 m intervals and as well in 180 and 220 m a.g.l. At each altitude, four to six flight legs were flown. The pink 'x' in Figure 5 marks the location of the meteorological observation tower. For the tower comparison, only data in-between the blue planes in Figure 5 are used. The main wind direction is 100° with an average horizontal wind velocity of $v_h \approx 5\,\mathrm{m\,s^{-1}}$. The measurements took place on August 23rd, 2019, on a sunny day from 10:00 to 12:00 UTC (12:00 to 14:00 LT). During the flights the stratification of the atmosphere was slightly unstable and the surface temperature was 18.5 °C.

The in-house made high-response humidity sensor is compared against a capacitive humidity sensor (Sensirion SHT31) aboard MASC-3, as well as against several capacitive hygrometers mounted on the

Table 3: Sensors used in dew point comparison with CMH.

Location	Manufacturer	Measurand	Range	Accuracy	Meas. element	Response time
Tower	Thies	Temperature	−30…+70 °C	±0.1 K	Electr. resistance	$\tau_9 0 < 20$ s
Tower	Thies	Humidity	0…100 % r.H.	±2 % r.H.	Capacitive	$\tau_9 0 < 20$ s
MASC-3	Sensirion SHT31	Temperature	0…+90 °C	±0.2 K	Electr. resistance	$\tau_6 3 > 2$ s
MASC-3	Sensirion SHT31	Humidity	0…100 % r.H.	±2 % r.H.	Capacitive	$\tau_6 3 \approx 8$ s

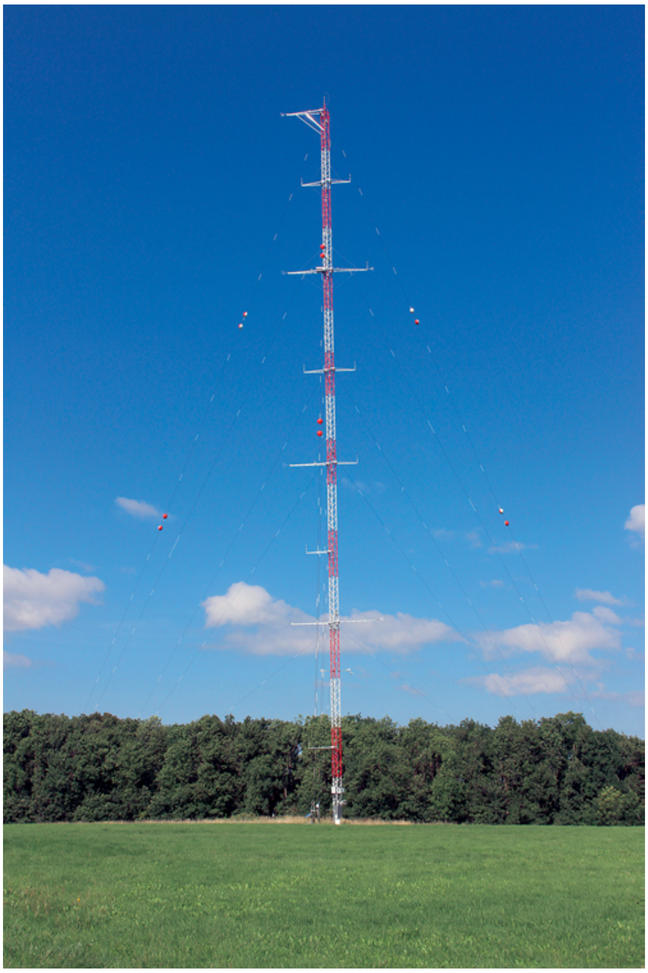

Figure 4: Meteorological 100 m measurement tower at the WINSENT test site on a plateau. Capacitive hygrometers are installed at different altitudes (23, 45, 73, 96 m a.g.l). The photograph is facing west. (Photo taken by the author).

meteorological tower (Figure 4). The tower sensors are Thies thermo- and hygrometers (model numbers 1.1005.54.34x) mounted at heights of 23 m, 45 m, 72 m and 96 m (see also Table 3 and Figure 5). All capacitive humidity sensors yield data at a low temporal resolution (1 Hz), which makes them suitable for comparison at low frequencies only. Leg averages of 130 m (approximately 700 data points) of the MASC-3 measurements directly in front of the met-tower are compared to temporal averages of the tower data using an equivalent fetch of about 4 min, which is the same time frame as the MASC-3 measurement took place.

3.3 Data conversion

The Thies thermo- and hygrometers and the SHT31 sensor both measure ambient temperature ϑ (°C) and relative humidity r (% r.H). To convert the relative humidity measurement (r) to dew point temperature (ϑ_d), the relation given in Eq. 3.1 and the Magnus formula Eq. 3.2 are used, giving the saturation pressure for water vapour (E) with r ranging from 0 to 1.

$$E(\vartheta_\mathrm{d}) = r \cdot E(\vartheta) \tag{3.1}$$

$$E(\vartheta) = E_0 \cdot \exp\left(\frac{a \cdot \vartheta}{b + \vartheta}\right), \tag{3.2}$$

with $E_0 = 6.111$ hPa, $a = 17.51$ and $b = 241.2$ °C

$$E(\vartheta_\mathrm{d}) = E_0 \cdot \exp\left(\frac{a \cdot \vartheta_\mathrm{d}}{b + \vartheta_\mathrm{d}}\right) = r \cdot E_0 \cdot \exp\left(\frac{a \cdot \vartheta}{b + \vartheta}\right) \tag{3.3}$$

Solving Eq. 3.3 for the dew point temperature ϑ_d yields Eq. 3.4. This equation can then be used to calculate the dew point directly from the relative humidity and ambient temperature measurement (Sonntag and Heinze, 1982).

$$\vartheta_\mathrm{d}(r, \vartheta) = \frac{b \cdot \ln(r) + \frac{a \cdot b \cdot \vartheta}{b + \vartheta}}{a - \ln(r) - \frac{a \cdot \vartheta}{b + \vartheta}} \tag{3.4}$$

4 Results

This section is divided into three subsections. In the first subsection exemplary spatial series of the CMH and SHT31 aboard MASC-3 are examined, as well as a short quality control is presented. Secondly, a low frequency response evaluation and a comparison of CMH measurements to tower measurements by averaged values is presented. Finally, the high frequency results (spectra, structure function) are presented.

4.1 Quality control and low frequency response

Figure 6 shows an exemplary spatial series of the high-response CMH and the capacitive SHT31 sensor mounted on the sensor dome (Figure 3) of the MASC-3 measured during a flyby at 120 m a.g.l. The spatial series shows that both sensors measured the same low-frequency changes in humidity, i.e. peak position and trend. The spatial series shows an expected dew point distribution in a well mixed layer near the surface. The

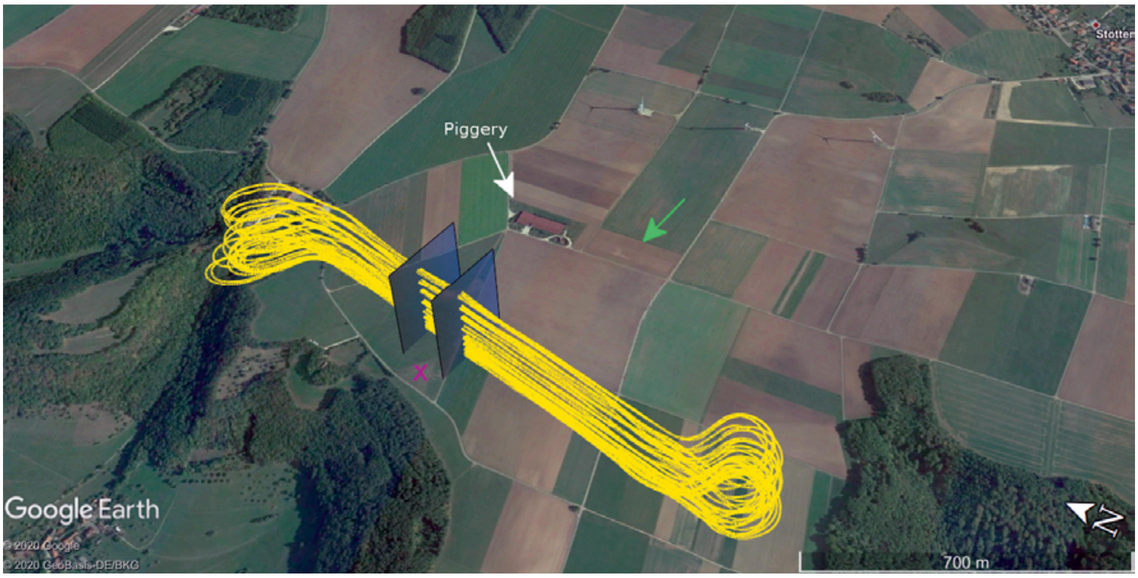

Figure 5: Top view of the measurement site from Google Earth. The pink 'x' marks the position of the met-tower near the town of Stötten. The N–S oriented flight path of the UAS is shown in yellow, tracked by the GPS system of the UAS, a green arrow indicates the easterly wind direction. For the tower comparison only data captured in-between the two blue planes is used. The measurements took place on August 23rd, 2019, on a sunny day from 10:00 to 12:00 UTC (12:00 to 14:00 LT).

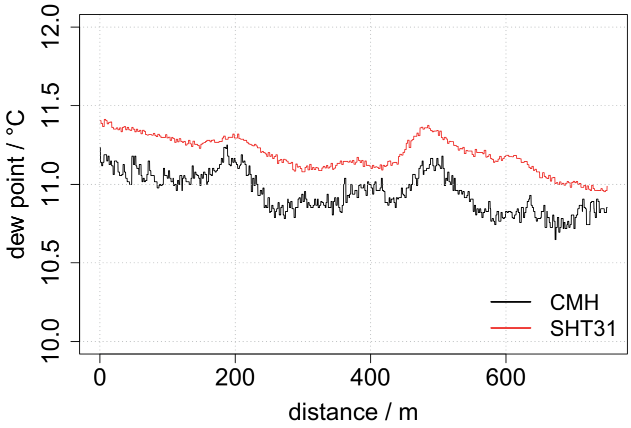

Figure 6: Spatial series along the whole distance of the measurement leg with the two sensors mounted onto the sensor dome of the MASC UAS. Both sensors measure the same signal. Noticeable is the constant offset between the two measurements. Also the SHT31 shows a distinct inertness (time constant of 8 s according to the manufacturer).

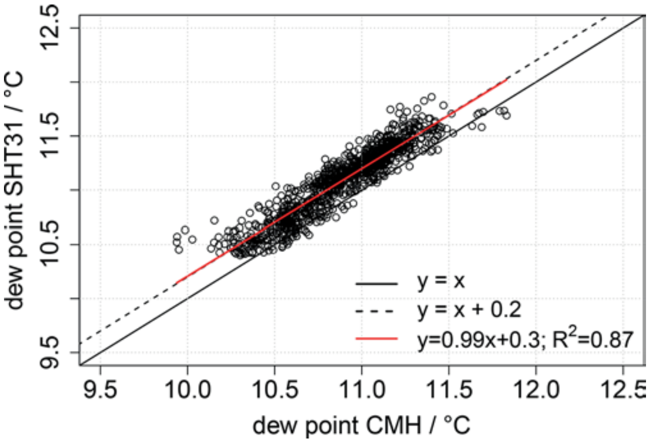

Figure 7: Scatter plot of all data obtained in 30 legs in various altitudes. The measurements are block averaged over 100 data points (1 s). The black solid line marks a 1:1 relationship, the black dashed line takes account of the constant offset between both sensors. The red solid line is the actual linear relationship of both sensors.

peaks are advected moisture by the piggery upstream. The correlation coefficient of both sensors for this measurement leg is 0.81. The high-response hygrometer shows more variations and resolves small-scale changes of the dew point temperature. It responses much faster than the SHT31, that has a response time τ_{63} of 8 s, according to the manufacturer at a flow velocity of $1\ \mathrm{m\,s^{-1}}$. With τ_{63} the time that it takes for the sensor to measure 63 % of a signal at a change of input. Thus, the SHT31 signal shows a distinct inertness, compared to the CMH signal.

As mentioned in Section 2.2, the chilled-mirror hygrometer and the capacitive SHT31 sensor show a constant offset of ca. 0.2 K that is caused by setting the illumination target level criterion in the calibration.

For a more in depth evaluation of the measured data of the CMH and the SHT31 sensor, Figure 7 shows a scatter plot of all measurements taken in several flight legs over various altitudes. For the scatter plot evaluation, the data were block averaged over 100 data points (1 s). Both sensors show good correlation $R^2 = 0.87$ or $R = 0.93$, resulting in a good linear regression (red line) with a slope of $0.99 \approx 1$. In the scatter plot the dashed black line is taking account of the constant offset between both sensors of 0.2 K and almost superimposes with the linear regression.

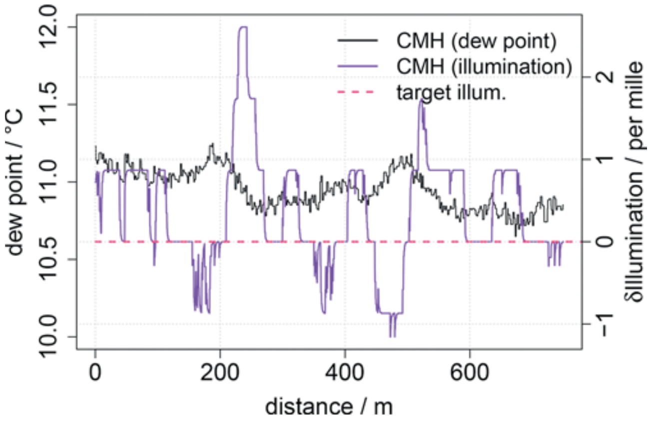

Figure 8: Spatial series of the CMH dew point temperature and the corresponding deviation of the illumination signal. The illumination fluctuates around 2 ‰ of its target value.

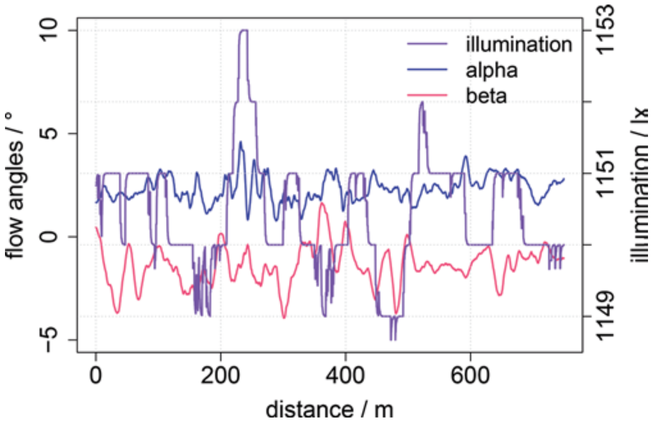

Figure 9: Flow angles alpha (angle of attack) and beta (side-slip) in degrees and absolute illumination at the TEC surface. A moving average over 50 data points (0.5 s) has been applied onto the time series of the flow angles.

In addition to the CMH spatial series, Figure 8 shows the measured deviation of the illumination signal (reflected light) of the CMH (purple line) from the target illumination (red dashed line). The illumination signal is the input parameter for the PID controller that regulates the voltage applied to the TEC. The maximum deviation in this exemplary measurement is approximately 2.5 ‰ from the target illumination (±3 lx at 1150 lx). A constant illumination is equatable to an equilibrium of evaporation (of condensed dew) and condensation (of water vapour). Thus, the mirror coating is held continuously at the mirror with only remaining insignificant variations. These are the variations that induce the PID regulation, but are kept down to a very minimum of ±3 lx.

To rule out that changes of the ram air affect the illumination, the measured flow angles (angle of attack and sideslip) for the exemplary flight leg in this study are calculated and shown in Figure 9. The angle of attack is the angle between the body's reference line (longitudinal axis through the fuselage of the UAS, i.e. back to front) and the oncoming flow in the vertical direction. The side-slip is the angle relating to the rotation of the aircraft centreline from the relative wind.

The blue and pink line are the angle of attack and side-slip of the airflow. The purple line is the measured illumination. The correlation coefficient between the illumination and alpha or beta equals 0.15 and −0.08 respectively. Note, that for this study, and for turbulence measurements in general, if a correlation is calculated in the order of $r \approx |0.2|$ to $|0.25|$ and it can be seen as a criterion of 'not correlated'. Hence, it can be concluded that at least for these angles, the CMH operates independently and is not affected by slight flow variations.

4.2 Comparison with tower data

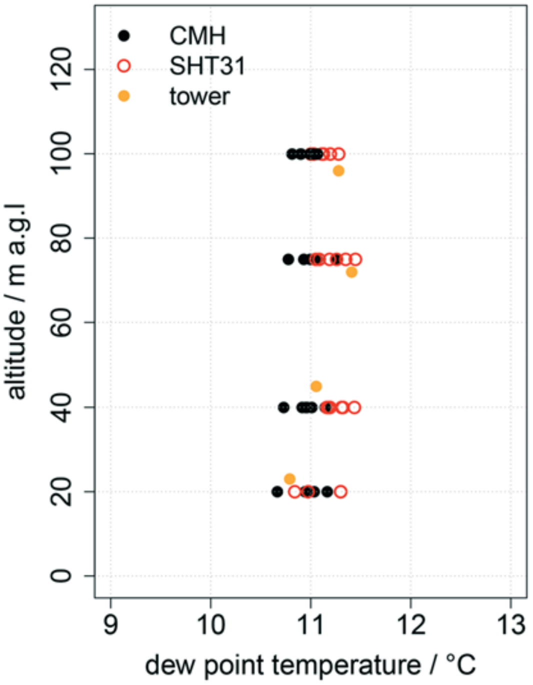

Figure 10: Measured dew point temperatures with a capacitive humidity sensor SHT31 and the CMH aboard the MASC-3 UAS. The measurements marked in orange are from capacitive hygrometers mounted on a meteorological tower about 50 m downstream.

Figure 10 shows averaged data of the available flight legs for each altitude. The offset between CMH (black) and SHT31 (red) is clearly visible. the tower measurements are seemingly systematically lower than the UAS measurements at low altitudes and systematically higher at high altitudes, even if there is no clear explanation for that at the moment. It might be that the installation position on the met-tower influences the measurement, a calibration error or drifting of the capacitance sensor.

Each level shows six data points, with each point corresponding to the one of the six flight-leg's sections of ca. 130 m. The standard deviation for the measurements at each level is approximately 0.1 K. The orange circles (Figure 10) are the values obtained from the Thies hygrometers on the meteorological tower, which is located approximately 50 m downstream of the MASC-3 flight path. Averages of each tower level were obtained

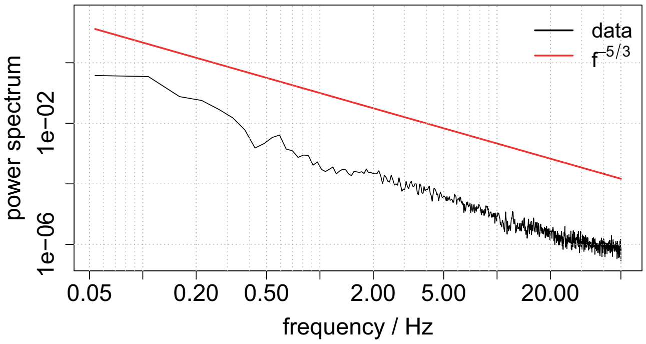

Figure 11: Frequency response (f) from an average power spectrum calculated from 14 measurement legs over the first four altitudes.

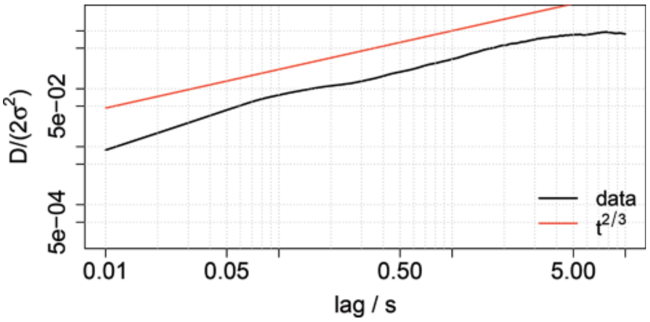

Figure 12: Exemplary structure function D of a measurement along a flight path in 120 m a.g.l in front of the meteorological tower. The red line is the reference lag$^{2/3}$.

over a time window of approximately 4 min during which the MASC-3 UAS measured at the corresponding altitude, i.e. one average over the whole duration of all six flight legs. For a horizontal wind speed of approximately 5 m s^{-1}, this window corresponds to a 1250 m fetch. Considering that the location of the tower sensors and MASC-3 flight-sections of each leg do not coincide, the averaged tower-based data is in good agreement ($\Delta K \approx 0.5$–$1\ K$) with the MASC measurements.

4.3 High frequency response

The main goal of developing a high-frequency humidity sensor for an unmanned airborne platform is to measure humidity fluctuations related to atmospheric turbulence. Consequently, the sensor requires a temporal resolution of at least 5–10 Hz to resolve eddies of 2 m size when measuring at an air speed of 20 m s^{-1}. For the high frequency analysis, power spectra of the CMH signal are evaluated. Figure 11 shows the average of 14 power spectra captured at the lowest four measurement altitudes (20, 30, 40 and 60 m a.g.l). The spectrum shows resolved turbulence in the inertial sub-range up to ca. 10 Hz, visible by the black curve following the KOLMOGOROV (1941) five-thirds law (red line). For higher frequencies a bend is visible.

As a second quality check of high-frequency response functionality, the structure function D of a single leg is calculated. The eddy-size distribution of a turbulent flow in the inertial sub-range, or the local structure of a turbulent flow, was first and foremost quantified using the (auto-) structure function (KOLMOGOROV, 1941), see also BANGE (2009) and WILDMANN et al. (2013).

$$D_{\phi(\tau)} = \frac{1}{D-\tau}\int_0^{D-\tau} dt\,[\phi(t+\tau)-\phi(t)]^2 \tag{4.1}$$

where τ is the lag or shift, ϕ is the physical quantity, D is the total length of the time series and t is the time.

To simplify the interpretation of structure functions, they can be normalized by dividing by twice the variance of the corresponding time series:

$$\frac{D_\phi}{2\sigma^2} = \begin{cases} 0 & : \text{fully correlated} \\ 1 & : \text{non-correlated} \\ 2 & : \text{fully anti-correlated} \end{cases} \tag{4.2}$$

Now, it is desired that the investigated data follows the $t^{2/3}$ line to the lowest lags possible, since the lowest point of parallelism is equal to the time constant of the sensor.

The structure function in Figure 12 shows a near parallel distribution to the Kolmogorov distribution (red line). Clear deviations from this line are observed for $\tau < 0.1$ s, or $1/\tau = 10$ Hz. This is in accordance with the characteristics observed in the averaged spectra presented in Figure 11. At the low frequency end the Kolmogorov inertial sub-range of locally isotropic turbulence is left at about 5 s. With an average flight velocity of 18 m s^{-1} this corresponds to eddies with diameters of 90 m, and might mark the beginning of the turbulent production range due to the relatively low flight altitude. The minor deviations from the ‘ideal’ Kolmogorov distribution between 0.1 s and 5 s could be explained by the heterogeneous inflow due to the complex terrain (escarpment, forests).

5 Conclusions and outlook

The first measurements of the in-house built high-frequency CMH aboard of an UAS type MASC-3 show good agreement compared to two industrial-made capacitive sensor types. One of the capacitive sensors is directly mounted next to the CMH and in good agreement with it (it shows the same peaks and trends). An offset of the CMH with respect to the capacitive sensor is related to the calibration that optimizes the sensor’s data output. Due to the same mean variation of the CMH and the SHT31, we estimate an achieved accuracy of the CMH of ±0.2 K. For obvious reasons the hygrometers mounted on the meteorological observation tower do not measure identical values as the MASC-3 based sensors. Nonetheless, the averages of the tower measurements are in good agreement with the UAS-based measurements. Considering the difficulty in comparing mobile line data to tower data, we find all sensors in good accordance (0.2 K off-set between both sensors aboard the UAS) to each other.

Concerning the high-frequency response of the CMH, it can be concluded that the CMH resolves the atmospheric dew point up to ≈ 10 Hz. Taking all measurements and the frequency response evaluation into account, the overall accuracy is promising. Measurements to compare the CMH sensor against absorption high-frequency instruments are planned. This will then allow for a comparison of turbulent latent heat fluxes. All measurements have been made along straight flight legs. The CMH is optimised for a constant air flow (constant TAS), regulated by the Pixhawk autopilot. Also changes in air flow are not critical as long as these changes occur slowly. It has been shown that the CMH sensor is not prone to small variations in flow angles (Figure 9).

The presented sensor has been assembled out of spare parts (TEC, mirror, TC). The signal processing is based on a microcontroller. In our first attempt an Arduino Nano has been chosen. A possible next step is using a more powerful microprocessor. This would increase the logging/processing frequency and therefore decrease the regulation intervals of the PID controller. A more precise and instant regulation of the TEC would then be possible. Another major improvement can be done by upgrading the temperature measurement. At the moment the TC read-out is one of the bottlenecks of the sensor.

Yet, a faster read-out of the temperature measurement does not equal a faster sensor. An important factor is also the thickness of the mirror, and TEC insulation. The thicker (and bigger) all these components are, the higher is the cumulative heat capacity that slows down heat transfer. An ideal TEC (or CMH) should have a heat capacity of zero, thus this is not possible, since all parts inherit mass. However, the cumulative heat capacity can be minimised by downsizing the TEC and mirror.

The next step is to improve the aerodynamics of the sensor. This contributes to the complete sensor system and handling of the aircraft. Also the inlet for the ram air will be reaching farther into the undisturbed air, to minimise the impact of the fuselage and its boundary layer.

In this study the presented prototype was equipped on an UAS. It is also possible to use the CMH system in eddy covariance (EC) stations once the sensor is ventilated properly. The CMH can also be used in still air, as long as the heat sink is cooled down properly. It is also possible to tune the PID controller to other wind/flow conditions than in the present case.

The CMH can also be calibrated against an absorption hygrometer (e.g. IRGASON, a combined gas analyser and sonic anemometer) to determine the absolute accuracy of the sensor. At the time of the study, no such high accuracy hygrometer was available.

Acknowledgements

We acknowledge support by the Projektträger Jülich (PtJ) for the WINSENT test site (project grant number: 0324129D) funded by the BMWi (German Federal Ministry for Economic Affairs and Energy). We also thank the Zentrum für Sonnenenergie und Wasserstoff-Forschung Baden-Württemberg (ZSW) for providing the tower measurement data. For technical support we thank Claudio Crazzolara, Hasan Mashni and Henrik Rieth.

We also acknowledge support by Open Access Publishing Fund of University of Tübingen.

References

Baldocchi, D., E. Falge, L. Gu, R. Olson, D. Hollinger, S. Running, P. Anthoni, C. Bernhofer, K. Davis, R. Evans, J. Fuentes, A. Goldstein, G. Katul, B. Law, X. Lee, Y. Malhi, T. Meyers, W. Munger, W. Oechel, K.T. Paw U, K. Pilegaard, H.P. Schmid, R. Valentini, S. Verma, T. Vesala, K. Wilson, S. Wofsy, 2001: Fluxnet: A new tool to study the temporal and spatial variability of ecosystem-scale carbon dioxide, water vapor, and energy flux densities. – Bull. Amer. Meteor. Soc. **82**, 2415–2434.

Bange, J., 2009: Airborne Measurement of Turbulent Energy Exchange Between the Earth Surface and the Atmosphere. – Sierke Verlag, Göttingen.

Bange, J., R. Roth, 1999: Helicopter-borne flux measurements in the nocturnal boundary layer over land – a case study. – Bound.-Layer Meteor. **92**, 295–325, DOI: 10.1023/A:1002078712313.

Beyrich, F., S.H. Richter, U. Weisensee, W. Kohsiek, H. Lohse, de H.A.R. Bruin, T. Foken, M. Göckede, F. Berger, R. Vogt, E. Batchvarova, 2002a: Experimental determination of turbulent fluxes over the heterogeneous litfass area: Selected results from the litfass-98 experiment. – Theor. Appl. Climatol. **73**, 19–34, DOI: 10.1007/s00704-002-0691-7.

Beyrich, F., H.J. Herzog, J. Neisser, 2002b: The litfass project of dwd and the litfass-98 experiment: The project strategy and the experimental setup. – Theor. Appl. Climatol. **73**, 3–18, DOI: 10.1007/s00704-002-0690-8.

Beyrich, F., J.P. Leps, M. Mauder, J. Bange, T. Foken, S. Huneke, H. Lohse, A. Lüdi, W.M.L. Meijninger, D. Mironov, U. Weisensee, P. Zittel, 2006: Area-averaged surface fluxes over the litfass region based on eddy-covariance measurements. – Bound.-Layer Meteor. **121**, 33–65, DOI: 10.1007/s10546-006-9052-x.

Bogena, H.R., R. Bol, N. Borchard, N. Brüggemann, B. Diekkrüger, C. Drüe, J. Groh, N. Gottselig, J.A. Huisman, A. Lücke, A. Missong, B. Neuwirth, T. Pütz, M. Schmidt, M. Stockinger, W. Tappe, L. Weihermüller, I. Wiekenkamp, H. Vereecken, 2015: A terrestrial observatory approach to the integrated investigation of the effects of deforestation on water, energy, and matter fluxes. – Sci. China Earth Sci. **58**, 61–75, DOI: 10.1007/s11430-014-4911-7.

De Bruin, H.A.R., W. Kohsiek, B.J.J.M. Van Den Hurk, 1993: A verification of some methods to determine the fluxes of momentum, sensible heat, and water vapour using standard deviation and structure parameter of scalar meteorological quantities. – Bound.-Layer Meteor. **63**, 231–257, DOI: 10.1007/BF00710461.

Foken, T., 2008: The energy balance closure problem: an overview. – Ecolog. Appl. **18**, 1351–1367, DOI: 10.1890/06-0922.1.

Fujiwara, M., M. Shiotani, F. Hasebe, H. Vömel, S.J. Oltmans, P.W. Ruppert, T. Horinouchi, T. Tsuda, 2003: Performance of the meteolabor "snow white" chilled-mirror hygrometer in the tropical troposphere: Comparisons with the vaisala rs80 a/h-humicap sensors. – J. Atmos. Ocean. Technol. **20**, 1534–1542, DOI: 10.1175/1520-0426(2003)020<1534:POTMSW>2.0.CO;2.

Kolmogorov, A.N., 1941: The Local Structure of Turbulence in Incompressible Viscous Fluid for Very Large Reynolds' Numbers. – In: Dokl. Akad. Nauk SSSR, Volume **30**, 301–305.

Koufang Lo, A., 1996: The importance of humidity effect in determining flux-profile parameters of a marine surface layer. – J. Appl. Meteor. **35**, 978–986, DOI: 10.1175/1520-0450(1996)035<0978:TIOHEI>2.0.CO;2.

Kuner, R., S. Rudersdorf, O. Schulze, 2015: Vorschriften und Betriebsunterlagen Nr. 3: Technikhandbuch für Wettermeldestellen des synoptisch-klimatologischen Mess- und Beobachtungsnetzes. – Technikhandbuch, Deutscher Wetterdienst, Offenbach.

Lampert, A., J. Hartmann, F. Pätzold, L. Lobitz, P. Hecker, K. Kohnert, E. Larmanou, A. Serafimovich, T. Sachs, 2018: Comparison of lyman-alpha and li-cor infrared hygrometers for airborne measurement of turbulent fluctuations of water vapour. – Atmos. Measur. Techn. **11**, 2523–2536, DOI: 10.5194/amt-11-2523-2018.

Mammarella, I., S. Launiainen, T. Gronholm, P. Keronen, J. Pumpanen, U. Rannik, T. Vesala, 2009: Relative humidity effect on the high-frequency attenuation of water vapor flux measured by a closed-path eddy covariance system. – J. Atmos. Ocean. Technol. **26**, 1856–1866, DOI: 10.1175/2009JTECHA1179.1.

Mauz, M., A. Rautenberg, A. Platis, M. Cormier, J. Bange, 2019: First identification and quantification of detached-tip vortices behind a wind energy converter using fixed-wing unmanned aircraft system. – Wind Energy Sci. **4**, 451–463, DOI: 10.5194/wes-4-451-2019.

Meijninger, W.M.L., F. Beyrich, A. Lüdi, W. Kohsiek, H.A.R. De Bruin, 2006: Scintillometer-based turbulent fluxes of sensible and latent heat over a heterogeneous land surface – a contribution to litfass-2003. – Bound.-Layer Meteor. **121**, 89–110, DOI: 10.1007/s10546-005-9022-8.

Metzger, S., W. Junkermann, B.B. K, H. Schmid, T. Foken, 2011: Measuring the 3-d wind vector with a weight-shift microlight aircraft. – Atmos. Meas. Tech. **4**, DOI: 10.5194/amtd-4-1303-2011.

Muschinski, A., R. Frehich, M. Jensen, R. Hugo, A. Hoff, F. Eaton, B. Balsley, 2001: Fine-scale measurements of turbulence in the lower troposphere: An intercomparison between a kite- and balloon-borne, and a helicopter-borne measurement system. – Bound.-Layer Meteor. **98**, 219–250, DOI: 10.1023/A:1026520618624.

Narvekar, S.V., V.K. Upadhye, 2016: Review of PI and PID controllers. – Int. J. Recent Trends Engineer. Res. **2**, 381–387.

Neininger, B., J. Hacker, 2012: Manned or unmanned – does this really matter?. – International Archives of the Photogrammetry, Remote Sensing and Spatial Information Sciences – ISPRS Archives **38**, 223–228, DOI: 10.5194/isprsarchives-XXXVIII-1-C22-223-2011.

neonscience.org, 2019: National science foundation's national ecological observatory network (NEON). – https://www.neonscience.org/data-collection/flux-tower-measurements (accessed: 2019-11-04).

Pixhawk-Organisation, 2019: Pixhawk 2.1 autopilot description. – http://pixhawk.org (accessed: 2019-07-01).

Platis, A., A.F. Moene, D.M. Villagrasa, F. Beyrich, D. Tupman, J. Bange, 2017: Observations of the temperature and humidity structure parameter over heterogeneous terrain by airborne measurements during the litfass-2003 campaign. – Bound.-Layer Meteor. **165**, 447–473, DOI: 10.1007/s10546-017-0290-x.

Rao, K.R., R. Mishra, 2014: Comparative Study of P, PI and PID Controller for Speed Control of VSI-fed Induction Motor. – Int. J. Engin. Develop. Res. **2**, 16512031.

Rautenberg, A., M. Schön, zum K. Berge, M. Mauz, P. Manz, A. Platis, van B. Kesteren, I. Suomi, S.T. Kral, J. Bange, 2019: The multi-purpose airborne sensor carrier masc-3 for wind and turbulence measurements in the atmospheric boundary layer. – Sensors **19**, 2292, DOI: 10.3390/s19102292.

Rebmann, C., M. Aubinet, H. Schmid, N. Arriga, M. Aurela, G. Burba, R. Clement, A. De Ligne, G. Fratini, B. Gielen, J. Grace, A. Graf, P. Gross, S. Haapanala, M. Herbst, L. Hörtnagl, A. Ibrom, L. Joly, N. Kljun, O. Kolle, A. Kowalski, A. Lindroth, D. Loustau, I. Mammarella, M. Mauder, L. Merbold, S. Metzger, M. Mölder, L. Montagnani, D. Papale, M. Pavelka, M. Peichl, M. Roland, P. Serrano-Ortiz, L. Siebicke, R. Steinbrecher, J.P. Tuovinen, T. Vesala, G. Wohlfahrt, D. Franz, 2018: ICOS eddy covariance flux-station site setup: a review. – Int. Agrophys. **32**, 471–494, DOI: 10.1515/intag-2017-0044.

Shuttleworth, W., 2007: Putting the "vap" into evaporation. – Hydrol. Earth Sys. Sci. **11**, 210–244, DOI: 10.5194/hess-11-210-2007.

Sonntag, D., D. Heinze, 1982: Sättigungsdampfdruck- und Sättigungsdampfdichtetafeln für Wasser und Eis (1. Aufl.). – Deutscher Verlag für Grundstoffindustrie, Leipzig.

Spiess, T., J. Bange, M. Buschmann, P. Vörsmann, 2007: First application of the meteorological Mini-UAV 'M2AV'. – Meteorol. Z. **16**, 159–169, DOI: 10.1127/0941-2948/2007/0195.

Stull, R., 2000: Meteorology for Scientists and Engineers. – Brooks/Cole, Belmond CA, USA.

van den Kroonenberg, A.C., S. Martin, F. Beyrich, J. Bange, 2012: Spatially-averaged temperature structure parameter over a heterogeneous surface measured by an unmanned aerial vehicle. – Bound.-Layer Meteor. **142**, 55–77, DOI: 10.1007/s10546-011-9662-9.

Van Kesteren, B., O.K. Hartogensis, D. Van Dinther, A.F. Moene, H.A.R. De Bruin, 2013a: Measuring H2O and CO2 fluxes at field scales with scintillometry: Part i – introduction and validation of four methods. – Agricult. Forest Meteor. **178-179**, 75–87, DOI: 10.1016/j.agrformet.2012.09.013.

Van Kesteren, B., O.K. Hartogensis, D. Van Dinther, A.F. Moene, H.A.R. De Bruin, A.A.M. Holtslag, 2013b: Measuring H2O and CO2 fluxes at field scales with scintillometry: Part ii – validation and application of 1-min flux estimates. – Agricult. Forest Meteor. **178-179**, 88–105, DOI: 10.1016/j.agrformet.2013.01.010.

Vömel, H., M. Fujiwara, M. Shiotani, F. Hasebe, S. Oltmans, J. Barnes, 2003: The behavior of the snow white chilled-mirror hygrometer in extremely dry conditions. – J. Atmos.Ocean. Technol. **20**, 1560–1567, DOI: 10.1175/1520-0426(2003)020<1560:TBOTSW>2.0.CO;2.

Ward, H.C., J.G. Evans, C.S.B. Grimmond, J. Bradford, 2015a: Infrared and millimetre-wave scintillometry in the suburban environment – Part 1: Structure parameters. – Atmos. Measur. Techn. **8**, 1385–1405, DOI: 10.5194/amt-8-1385-2015.

Ward, H.C., J.G. Evans, C.S.B. Grimmond, 2015b: Infrared and millimetre-wave scintillometry in the suburban environment – Part 2: Large-area sensible and latent heat fluxes. – Atmos. Measur. Techn. **8**, 1407–1424, DOI: 10.5194/amt-8-1407-2015.

Wildmann, N., M. Mauz, J. Bange, 2013: Two fast temperature sensors for probing of the atmospheric boundary layer using small Remotely Piloted Aircraft (RPA). – Atmos. Measur. Techn. **6**, 2101–2113, DOI: 10.5194/amt-6-2101-2013.

Wildmann, N., F. Kaufmann, J. Bange, 2014a: An inverse-modelling approach for frequency response correction of capacitive humidity sensors in abl research with small Remotely Piloted Aircraft (RPA). – Atmos. Measur. Techn. **7**, 3059–3069, DOI: 10.5194/amt-7-3059-2014.

Wildmann, N., M. Hofsäss, F. Weimer, A. Joos, J. Bange, 2014b: MASC; a small Remotely Piloted Aircraft (RPA) for wind energy research. – Adv. Sci. Res. **11**, 55–61, DOI: 10.5194/asr-11-55-2014.

Wildmann, N., S. Ravi, J. Bange, 2014c: Towards higher accuracy and better frequency response with standard multi-hole probes in turbulence measurement with remotely piloted aircraft (RPA). – Atmos. Measur. Techn. **7**, 1027–1041, DOI: 10.5194/amt-7-1027-2014.

Wolf, B., C. Chwala, B. Fersch, J. Garvelmann, W. Junkermann, M.J. Zeeman, A. Angerer, B. Adler, C. Beck, C. Brosy, P. Brugger, S. Emeis, M. Dannenmann, F. De Roo, E. Diaz-Pines, E. Haas, M. Hagen, I. Hajnsek, J. Jacobeit, T. Jagdhuber, N. Kalthoff, R. Kiese, H. Kunstmann, O. Kosak, R. Krieg, C. Malchow, M. Mauder, R. Merz, C. Notarnicola, A. Philipp, W. Reif, S. Reineke, T. Rödiger, N. Ruehr, K. Schäfer, M. Schrön, A. Senatore, H. Shupe, I. Völksch, C. Wanninger, S. Zacharias, H.P. Schmid, 2017: The scalex campaign: Scale-crossing land surface and boundary layer processes in the tereno-prealpine observatory. – Bull. Amer. Meteor. Soc. **98**, 1217–1234, DOI: 10.1175/BAMS-D-15-00277.1.